



UNIVERSITY OF GENOVA
PHD PROGRAM IN BIOENGINEERING AND ROBOTICS

Development of experimental setups for the characterization of the mechanoelectrical coupling of cells *in vitro*

by

Ilaria Pulsoni

Thesis submitted for the degree of *Doctor of Philosophy* (31° cycle)

January 2019

Prof. Roberto Raiteri

Supervisor

Prof. Giorgio Cannata

Head of the PhD program

Dibris

Department of Informatics, Bioengineering, Robotics and Systems Engineering

I would like to dedicate this thesis to all the PhD students.

Do not give up.

Acknowledgments

I would first like to thank my PhD supervisor Professor Roberto Raiteri, for everything he did for me during these three years. I would also like to thank all the team from the Bioengineering Laboratory of the University of Genova: the Professors Sergio Martinoia, Laura Pastorino and Paolo Massobrio, the researchers Pasqualina Farisello, Brunella Tedesco and Elena Della Casa, the technicians Giorgio Carlini and Filippo Sante, and all the PhD students. In particular, a special thank you goes to Hossein Dabiri, who supported me since the beginning of my PhD, and still does.

I would also like to acknowledge Professor Petr Skladal of the Central European Institute of Technology of Masaryk University in Brno, for giving to me the possibility to continue my research there. In particular, I would like to thank Professor Vladimir Rotrekl, the researcher Jan Pribyl and the PhD student Sarka Jelinkova. Again, a very special thank you goes to Guido Caluori, who helped me since the first day I moved to Genova and has continued doing it in Brno.

I must express my very profound gratitude to my parents, to my sister Federica and of course to my boyfriend Shaun, for all the encouragements all along these years, and through the process of writing this thesis.

Finally, thanks to all my friends who made these three years also fun, and to my flat mates Giulia Adriana and Elena for supporting me every day and every time.

This accomplishment would not have been possible without all you guys. Thank you.

Author

Ilaria Pulsoni

Abstract

The field of mechanobiology emerged from the many evidences that mechanical forces acting on cells have a central role in their development and physiology. Cells, in fact, convert such forces into biochemical activities and gene expression in a process referred as mechanotransduction. *In vitro* models that mimic cell environment also from the mechanical point of view represent therefore a key tool for modelling cell behaviour and would find many applications, e.g. in drug development and tissue engineering.

In this work I introduce novel tools for the study of mechanotransduction. In particular, I present a system for the evaluation of the complex response of electrically active cells, such as neurons and cardiomyocytes. This system integrates atomic force microscopy, extracellular electrophysiological recording, and optical microscopy in order to investigate cell activity in response to mechanical stimuli. I also present cell scaffolds for the *in vitro* study of cancer. Obtained results, although preliminary, show the potential of the proposed systems and methods to develop accurate *in vitro* models for mechanobiology studies.

Table of Contents

List of figures	vi
List of tables	xii
Chapter 1	1
Introduction to Cell Mechanobiology	1
1.1 Mechanobiology and Mechanotransduction.....	1
1.1.1 Mechanobiology in Heart and Brain.....	4
1.2 Technologies for Mechanobiology.....	6
1.3 Mechanoelectric Coupling.....	9
1.3.1 AFM as Tool for the Mechanical Characterization of Cells.....	9
1.3.2 MEA Devices as Tool for the Electrical Characterization of Cells.....	11
1.4 Cell Patterning for Specific Investigations.....	13
1.5 The Importance of the Substrate: Stiffness and Topographical Cues can Influence Cell Response.....	14
1.6 Conclusion.....	15
Chapter 2	16
The Atomic Force Microscopy	16
2.1 Introduction.....	16
2.2 Description and Operating Principles.....	18
2.3 Imaging.....	20
2.4 Force Distance Curves.....	21
2.5 AFM Probes.....	22
Chapter 3	24
Materials and Methods	24
3.1 Cell Stretcher Device.....	24
3.1.1 Characterization of the Deformation.....	26
3.1.2 Device Holder and Vibrations Stabilizer Disk.....	26
3.1.3 Cell Culture.....	27

3.2 AFM-MEA Integrated System.....	28
3.2.1 Setup Description.....	28
3.2.2 MEA and AFM Tools.....	31
3.2.3 Software.....	33
3.2.4 Cell Patterning.....	33
3.2.5 Cell Culture.....	35
3.2.5.1 Microelectrode Array Cleaning and Coating.....	35
3.2.5.2 Neuronal Network Preparation.....	35
3.2.5.3 Neuron Plating on MEA Chip.....	35
3.2.5.4 Neuron Patterning.....	35
3.2.5.5 hPSC Culture and Cardiac Differentiation.....	36
3.2.5.6 Beating Cardiac Clusters Plating on MEA Chips.....	37
3.3 Mechanical Characterization of a 3D Alginate-Matrigel Hydrogel as Scaffold for Human Breast Cancer Cells.....	37
3.4 Characterization of the Topographical Features of Graphene-Oxide Functionalized Substrates to Study Cell Adhesion.....	38
3.5 Effects of Different Probes on Elasticity Measurements.....	39
Chapter 4	41
Results and Discussion	41
4.1 Optimization of the Cell Stretcher Device System.....	41
4.2 AFM-MEA Integrated System.....	42
4.2.1 Characterization of the System with Neurons.....	43
4.2.2 Neuronal Patterns.....	45
4.2.3 Mechanical Stimulation on hPSC-CMs.....	46
4.3 Mechanical Characterization of a 3D Alginate-Matrigel Hydrogel as Scaffold for Human Breast Cancer Cells: Results.....	52
4.4 Characterization of the Topographical Features of Graphene-Oxide Functionalized Substrates to Study Cells Adhesion: Results.....	55
4.5 Probe Size Effect on AFM Nanoindentation Measurements: Results.....	58
Chapter 5: Conclusions and Future Perspectives	59
References	60
Appendix A: Mechanical Stimulation Protocols for hPSC-CMs	67

List of figures

1.1: A cell receives mechanical stimuli from the substrate (through mature integrin adhesions) and from another cell (through cadherin receptors). These stimuli are sensed through mechanosensors (talin, vinculin, p130CAS, focal adhesion kinase, and muscle LIM proteins); signal factors (such as myocardin-related transcription factor A, Yes-associated protein, LIM proteins) are sent to the nucleus and affect gene expression and, consequently, cell behaviour and function [1].

1.2: Illustration of the principal mechanical forces that act in the heart, blood vessels and connective tissue [2].

1.3: Flow chart highlights cells mechanotransduction.

1.4: Illustration of the variety of mechanical signals that can influence cell's fate through a restructuring of the cytoskeleton and a mechanotransduction pathway.

1.5: Phases in organ engineering [24]: design, technology and discovery of new biological phenomena such as mechanotransduction, which in turn influences further study designs that requires the development of more advanced and targeted technologies.

1.6: From the left: micropipette aspiration, micro-mechanical stretching device, and shear stress in microfluidic devices.

1.7: Schematization of pillar arrays, magnetic tweezers and optical trap technologies, for which the main characteristics such as resolution and maximum force are shown. (∇B = magnetic field gradient; d =distance; F = force; k =spring constant; μ = magnetic moment) [1].

1.8: (a) Schematic of one cell stretcher and (b) its cross-sectional view (section A-A) showing a single cell adhered on top of the actuator at the off state. (c) Actuated state of the device, explaining that when a high voltage is applied to the bottom microelectrode, the membrane compresses in thickness and expands uniaxially. (d) Cross-sectional view of the actuated state of the cell stretcher, showing that a single cell attached on the actuator is stretched with the substrate [31].

1.9: Ultrasound coupled with piezoelectric nanoparticles.

1.10: Diagram of a cantilever array. Target cells in suspension are immobilized on the cantilever; these are cultured, and their mass is measured via the resonance frequency shift of the cantilever [50].

1.11: Illustration of the FluidFM setup in whole-cell configuration. The tip aperture allows connecting the electrode inside of the pipet with the cytosol. The patch-clamp electronics clamps the transmembrane potential [51].

1.12: Scheme of the biosensor setup used for biomechanical characterization of cardiomyocyte clusters. Main elements of the setup are: 1-Embryonic body, 2-AFM cantilever, 3-glass cantilever holder block, 4-AFM laser source and photodetector of laser position, 5-plastic (PP) tubing, 6-peristaltic pump, 7-syringe for drug injection [53].

1.13: On the left, an example of micro-electrodes layout; on the right, electron microscopy image of a TiN covered planar electrode.

1.14: A typical MEA device by Multichannel System.

1.15: Circuitual equivalent of the electrode-cell system, for a passive planar metal electrode [59].

1.16: A) Neonatal rat cardiomyocytes seeded on chitosan patterned glass surfaces at 8 days of culture; B) Patterned cardiomyocytes express cardiac troponin I (green) and exhibit a developed contractile apparatus (arrows) [67].

1.17: Neuronal pattern on microelectrodes array obtained using microcontact printing technique [66].

1.18: Model of the cooperative interplay between immobilized heparin and substrate topography in regulating cell behaviour [71].

2.1: Scanning probe microscopy applications [72].

2.2: The image shows the comparison between the SPM and a human deprived of his eyesight: by moving the stick, the person can figure out how the object looks; on the right side of the figure, the general configuration of an SPM, either in a tip-moving setup or in a sample-moving setup, is shown. The instrument is equipped with a sharp pointed probe, that can be a metal wire (STM) or a sharp object attached to a cantilever (AFM) moved in any direction by a piezo scanner. In addition, the instrument includes a detector to register the tip's position (x, y, z) at all times and a feedback mechanism that controls the interaction of the tip with the sample [72].

2.3: a) Schematic representation of a SPM; b) Different acquisition modes, with (constant signal) or without (constant height) Z-feedback loop; c) Probe scanning path in X (fast scan direction) and Y (slow scan direction).

2.4: Inter-atomic Force vs. distance.

2.5: Illustration of AFM photodetection system: the cantilever deflection results in a shift in laser spot position on PSPD. AFM main signal (vertical deflection) is calculated from $(A+B)-(C+D)$, while frictional torsion (lateral deflection) is $(A+C)-(B+D)$.

2.6: Illustration of the different imaging modes (on the left). On the right side of the figure, the regions of the three AFM modes are indicated: contact-mode operates in the repulsive region, the tapping and non-contact modes operate respectively in attractive/repulsive and attractive regions.

2.7: A typical force curve is shown: when approaching the surface, the cantilever is in an equilibrium position (1) and the curve is flat; as the tip approaches the surface (2), the cantilever is pushed up to the surface and deflected upwards, which is seen as a sharp increase in the measured force (3); once the tip starts retracting, the deflection starts to decrease and passes its equilibrium position at (4); as it is moved away from the surface the tip snaps in due to interaction with the surface, and the cantilever is deflected downwards (5); once the tip-sample interactions are terminated due to increased distance, the tip snaps out, and returns to its equilibrium position (6) [78]. The negative deflection preceding the linear part in the blue curve called "jump to contact" and the tip adhesion in the red one are shown: in the first case, the tip is driven towards the sample in presence of attractive interactions, in the second case, the cantilever deflects downwards because of adhesive phenomena.

2.8: The probe is generally characterized by its height, h_{probe} , its width, w_{probe} , its opening angle, and its radius of curvature (ROC). A good probe should have a high aspect ratio, a small opening angle and a small ROC to image the sample's true topography at the highest resolution [72].

2.9: A) Rectangular and triangular cantilevers [72]; pyramidal (B), spherical (C) and conical (D) tips.

2.10: Representation of cantilever's force, displacement and spring constant.

3.1: A) Illustration of the circular dielectric elastomeric actuator, and the modality of working: we can distinguish the active and the passive area, and the deformation mode when the high voltage is on; B) other types of deformation can be obtained by changing the electrodes layout.

3.2: The cell stretcher device.

3.3: The deformation of the substrate was quantified by tracking fluorescent microspheres attached in the passive area during the application of the high voltage and analysing the distance travelled.

3.4: Rectangular shaped device holder, frontal (left) and back (right) view. In the frontal view the metal plate for the coupling with the AFM is also shown.

3.5: Schematization of the temperature sensor (pt100) and the heating pads placed behind the aluminium plate.

3.6: The image shows the main elements of the multilayer device that includes a heating plate to keep cells cultured on the electrodes at 37°C, the MEA device, the recording board for the detection of cell signals, and the magnetic ring for the coupling with the AFM stage.

3.7: Schematization of the AFM-MEA integrated system.

3.8: The front (A) and the back (B) sides of the recording board, where it is possible to see all the pre-amplifiers connected to all the recording channels; C) filter-amplifier from Multichannel System; D) electronic board employed for collecting MEA signals and data from the AFM; E) the assembled multilayer device from fig. 3.6 with all the cables for the connections with the temperature controller, and the filter-amplifier; F) two version of the plate for MEAs allocation: the aluminium one to be heated and the plastic one for trials where the temperature control was not required.

3.9: Schematization of the AFM-MEA integrated system where it is shown the single cell, plated on one electrode, whose features are investigated by AFM cantilever, the recording circuitry, and the optical microscope.

3.10: A) 60HDMEA30/10iR-ITO and B) 60MEA200/30iR-Ti layouts.

3.11: Microcontact printing setup inside the biological hood.

3.12: Cortical neurons plated on a MEA chip.

3.13: A) A PDMS mask consisting of two compartments and the microchannels on the MEA surface; B) A PDMS mask consisting of one compartment on MEA surface; C) Illustration of the two compartments geometry; D) Neuronal pattern on MEA obtained using the PDMS mask with the two compartments and the microchannels: it is possible to distinguish lines of axons (indicated by the black arrows) grown inside the microchannels at 21 DIV.

3.14: A beating cardiac cluster plated on a high density MEA chip.

3.15: Schematic description of the protocol used to produce 3D cell-laden alginate-matrigel composite gels: breast cancer cells MDA-MB-231 are seeded first in liquid alginate and then matrigel is added working on ice. The cell-laden solution is transferred into Agar molds enriched with CaCl_2 ions at 37°C for to allow gelation. Then, 3D gels are removed by molds and transferred into plates with culture media.

3.16: Optical image of a cantilever with a spherical tip glued on it.

3.17: The image shows a spherical tip indenting a substrate, where R is the tip radius, a is the contact radius and h is the indentation.

4.1: AFM images that show the topography of the same fibroblast before (on the left) and after the deformation of the substrate.

4.2: Biaxial cell stretcher device schematization (frontal view): four couples of compliant electrodes allow, under the application of high voltage, the deformation of the device passive zone in two perpendicular directions in-plane.

4.3: Mean percentage strain in absolute value for three biaxial devices of 65mm (on the left) and 95mm (on the right) diameter, measured with the stabilizer support.

4.4: On the left, a MEA device, and, on the right, an optical image of the active area where it is possible to identify the electrodes, the neurons and a triangular cantilever.

4.5: Illustration of the system composed by the heating plate, the spacer, the MEA device and the recording board.

4.6: Neuronal extracellular signal recorded using the custom pre-amplifier board.

4.7: The graph on the left shows the firing activity recorded with the commercial system and the AFM-MEA integrated system: values are normalized with respect to the ones recorded using the commercial system, and data are shown with mean and standard deviation; on the right, the firing activity on the most active electrodes recorded using the two systems is shown.

4.8: Illustration of the geometry chosen to fit the electrodes layout (on the left), and a fluorescent image of the adhesion factors patterned on glass.

4.9: Images of the most significative cell pattern results on glass. In particular, image A shows lines of patterned neurons subjected to a process of immunolabeling for the MAP-2 dendritic protein (in green) and for the synapsin protein (in red), at 18 DIV (scale bar = $100\mu\text{m}$); images B, C, D, E show different neuronal culture patterned on glass at 10 DIV, scale bar = $200\mu\text{m}$.

4.10: A) An attempt to obtain lines of neurons upon the electrodes; B) and C) fluorescent images of adhesion factors on the electrodes. The distance between two electrodes (centre-centre) is $200\mu\text{m}$.

4.11: Cardiac extracellular signal recorded using the custom recording board.

4.12: A) Illustration of piezo position and force in different modes of operation; B) differences between the constant force and the constant height mode: in the first one, the cantilever deflection is kept constant and the piezo moves to maintain it; in the second mode, the piezo height is kept constant while the cantilever deflection changes with the topography of the sample.

4.13: Interaction between the cantilever and the beating cardiac cluster during the application of static force, impulsive force and transient overload.

4.14: *Overlap of the recorded cardiac and force signals during the application of impulsive forces (top) and during the application of static forces (bottom) as illustrated in fig. 4.12 A.*

4.15: *Optical images of beating cardiac cluster plated on a HD MEA (on the left), and on a standard MEA (on the right); in both images it is possible to distinguish the cantilever, the cells and the electrodes.*

4.16: *Signal amplitude (A) and beating rate (B) trends during the application of static and impulsive forces; C) overlap of the force signal and the cardiac signal peak train (every peak is a beat).*

4.17: *A) Beating rate trend during the application of static forces, transient overload and impulsive forces; B) transversal force transmitted by cells to the cantilever during the application of static forces in constant height mode*

4.18: *Using an adequate mould, well arrays could be designed on an agarose substrate; after the addition of cell suspension and centrifuge it, cells will precipitate to the bottom of the caves, assuming the same shape.*

4.19: *The detection of cell response after a mechanical stimulation could be improved by reducing the cell cluster size, to promote the propagation*

4.20: *(A) The three types of obtained compact gels; panel B shows three representative forces versus vertical displacement curves measured on three different hydrogels. The $z = 0$ corresponds to the vertical piezo displacement where the AFM tip gets into contact with the hydrogel surface; panel C shows the Young modulus average and standard deviation for the different hydrogels probed by AFM nanoindentation: bar colours correspond to different alginate concentrations, while matrigel concentration is shown along the x axis (Kruskal-Wallis test, $p < 0.05$).*

4.21: *A) MDA-MB-231 cells cultured within materials for 24 h, stained with fluorescence dyes: calceinAM (green) for live cells and propidium iodide (red) for dead cells. B) MDAMB- 231 cell proliferation after 4 and 7 days of culture for different materials. Symbol * indicates statistical significance (ANOVA test; number of samples: $N \geq 10$; $p < 0.05$).*

4.22: *(A-I) Confocal sections of cells embedded within Alginate/Matrigel gels at different time points. Cells were stained for F-actin (phalloidin) and nuclei were counterstained with Propidium Iodide. To be noted that cells show stellate morphology and invadopodia (red arrows) in 50%:50% A:M gels (G, H, I).*

4.23: *(A-C) Nuclei shapes isolated from A-to-I at fig. 4.22. In presence of Matrigel cells express nuclear fragmentation, characteristic of malignancy.*

4.24: *AFM images of an area of $5\mu\text{m} \times 5\mu\text{m}$ of Alg and GO/Alg films, respectively (panel A); quantitative analysis of average roughness of Alg and GO/Alg substrates. Values are reported as mean value and standard deviation. Symbol * indicates samples with statistically different elasticity (Kruskal-Wallis test, $p < 0.05$) (panel B).*

4.25: *Proliferation rate of MDA-MB-231, HOS and 3T3 cell lines up to one week of cell culture over Alg and GO/Alg substrates.*

4.26: *Cell adhesion patterns on Alg and GO/Alg substrates. The three cell lines were cultured over each substrate for 24 hours. Actin and vinculin were stained with phalloidin-TRITC and a monoclonal*

antivinculin antibody, respectively. The merged images show actin (red), vinculin (green), and the DAPI-stained nucleus (blue).

*4.27: Analysis of the morphological parameters of cells cultured the substrates for 24 hours. Values are reported as mean + SD * indicates $p < 0.05$ significance.*

4.28: Young modulus values of a PDMS substrate obtained using three different type of nanoindenter.

List of tables

1.1: Some examples of studies in the field of mechanobiology; in particular, the table underlines the cell type studied, its response to a specific load, and the relevance.

3.1: The table summarizes cantilever models with their main characteristic that were taken into consideration for the purpose of this work.

3.2: A summary of the processes of PDMS stamps fabrication, adhesion factors printing and cell plating.

3.3: The table shows the values of radius spring constant of the spherical tips employed, and the values of indentations reached for the purpose of this study.

4.1: Experimental protocol for hPSC-CMs.

Chapter 1

Introduction to Cell Mechanobiology

“The field of mechanobiology emerged based on the recognition of the central role that physical forces play in development and physiology [...]. At the time I entered the laboratory in the mid-1970s, virtually all research centred on the role of chemicals and genes in developmental control [...]. I suggested an alternative concept: mechanical forces may be equally important for regulation of cell and tissue formation, as well as for the development of diseases, such as cancer.”

Donald E. Ingber

1.1 Mechanobiology and Mechanotransduction

Mechanobiology is the study of cell responses to mechanical stimuli and of the mechanotransduction mechanisms which transduce such stimuli into a cascade of intra-cellular events. In other words, the term mechanobiology refers to the investigation of the role of mechanical forces in cell biology, and, in particular, it includes two aspects:

- the explanation of the mechanisms by which cells sense, transduce, and respond to mechanical forces and modulate their functions;
- the characterization of cellular mechanical properties.

Mechanotransduction converts mechanical stimuli such as substrate rigidity, stretching or shear stress into chemical signals which, in turn, regulate cell behaviour and function. Typically, the pathway involves receptors at focal adhesion points or cell-cell contact (for example, integrins and cadherins), mechanosensors, and nuclear signalling factors to change gene and protein expression profiles (fig. 1.1). Nuclear deformation can also lead to changes in gene expression patterns. The timescale of these events ranges from milli-seconds to seconds for the activation of mechanosensors, hours for altered gene expression, days for changes in cell behaviour and function, and weeks for tissue development [1].

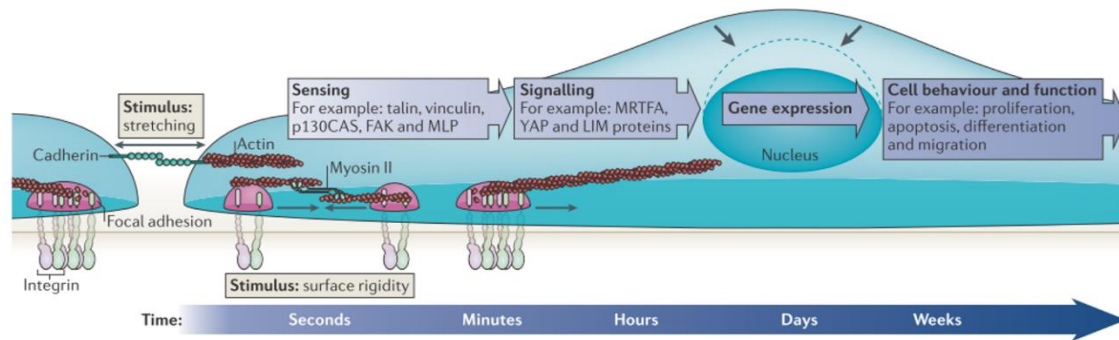


Figure 2.1: A cell receives mechanical stimuli from the substrate (through mature integrin adhesions) and from another cell (through cadherin receptors). These stimuli are sensed through mechanosensors (talin, vinculin, p130CAS, focal adhesion kinase, and muscle LIM proteins); signal factors (such as myocardin-related transcription factor A, Yes-associated protein, LIM proteins) are sent to the nucleus and affect gene expression and, consequently, cell behaviour and function [1].

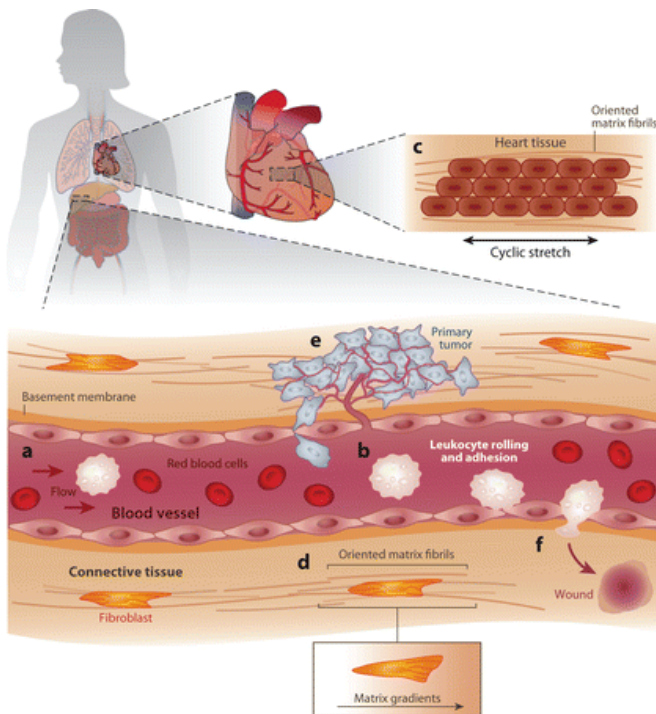


Figure 1.1: Illustration of the principal mechanical forces that act in the heart, blood vessels and connective tissue [2].

Among the mechanical forces that act on the body of a microscale there are: static loads due to gravity, tensile muscular forces that act on bones through tendons to move joints and permit human locomotion, compressive loads on cartilage and bones during walking and exercise, blood pressure and shear stresses on the vessels due to blood flow. Such forces act on many tissues and organs: the lung tissue is stretched cyclically due to the respiratory movements and is exposed to mechanical forces from blood flow and surface tension; dermal tissues are, in turn, subject to tensile, compressive, and shearing forces. The heart is also subject to mechanical forces due to changes in blood volume and pressure.

Figure 1.2 shows the main forces the heart, blood vessels, and skin are subject to: in blood vessels, for example, cells are continuously

subject to shear and hydrostatic stress from blood flow, that also modulates leukocyte rolling and adhesion (fig. 1.2, a and b). Cardiac tissue is stretched cyclically during heart contraction (fig. 1.2, c), and extracellular matrix (ECM) proteins guide the myocardial alignment during cardiovascular development as well as the directional organization of cells in connective tissue (fig. 1.2, d). Neoplastic cells originate and spread from a primary site (fig. 1.2, e) and subsequently invade other location by stimulating other tissues with soluble factors and by tracking collagenous matrix fibers [2]. Finally, in a connective tissue scar (fig. 1.2, f), the collagen matrix is characterized by a disordered architecture with dense parallel bundles, unlike the mechanically efficient basket-weave meshwork of collagen in normal dermis [3].

Living cells can adapt themselves to the dynamic changes in the physiological environment and can maintain the appropriate biological functions as they have physical and biochemical modules. For instance, cells actively sense and respond to biochemical signals, but also face different biomechanical environments, and respond to mechanical stress that could be externally applied or internally generated, such as changes in plasma membrane tension due to the topography and rigidity of the ECM, shear stress, and hydrostatic pressure.

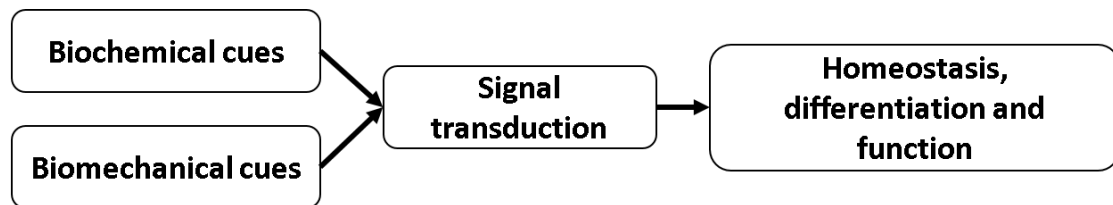


Figure 1.3: Flow chart highlights cells mechanotransduction.

Mechanical loads induce changes in the structure, composition, and function of living tissues at the cellular level. Many studies have shown that mechanical loads can influence diverse cellular functions, such as cell proliferation, protein expression, and the production of soluble factors. The components that are mainly involved in the mechanotransduction mechanisms include the cytoskeleton, integrins, G proteins, receptor tyrosine kinases, mitogen-activated protein kinases, and stretch-activated ion channels. A typical example of how a tissue grows and remodels itself in response to mechanical stimuli is the bone tissue, which changes its shape, density, and stiffness when its mechanical loading conditions are altered [4,5]. At the same way, blood vessels remodel

themselves in response to altered blood pressure and shear stress [6].

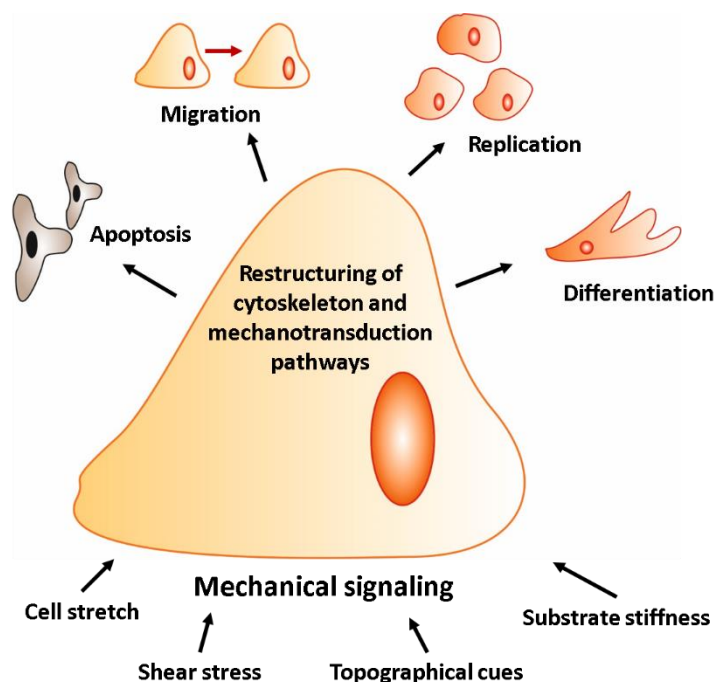


Figure 1.4: Illustration of the variety of mechanical signals that can influence cell's fate through a restructuring of the cytoskeleton and a mechanotransduction pathway.

Figure 1.4 shows a schematic representation of the variety of biomechanical cues, such as substrate stiffness, cell stretch, shear stress, and topography of the environment surrounding the cell that can regulate cell signalling and function. These mechanical forces are sensed by the cell and converted into biological responses; this in turn causes a restructuring of the cytoskeleton and intracellular signalling pathways transmitted through mechanosensitive ion channels or transmembrane adhesion receptors [7]. The mechanotransduction pathways can be activated to regulate gene expression, cell contractility, and ultimately cell apoptosis, migration, proliferation, differentiation, and growth.

As a consequence, impairments of these cellular processes contribute to cause many diseases and pathological conditions. In fact, abnormal mechanical loading conditions can alter cellular functions and change the structure and composition of the ECM, eventually leading to tissue or organ pathologies such as osteoporosis, osteoarthritis, tendinopathy, atherosclerosis, and fibrosis in the bone, cartilage, tendon, vessels, heart, lung, and skin. At the same way, overstimulation can induce maladaptive remodelling, as in the case of hypertension-associated vascular stiffening with age [8]. When cells and tissues are removed from the body [24], they begin to degenerate and malfunction, also because of the lack of proper mechanical feedback, which is a continuously ongoing process in most tissue systems *in vivo*.

The table below summarizes the results of some studies in the field of mechanobiology. The focus of these studies was the investigation of the cellular response after the application of a specific mechanical stimulus.

Cell type	Response	Type of load	Significance	Reference
Human tendon fibroblasts	Increase in cell proliferation, collagen I gene expression, and collagen I protein	Uniaxial stretch	Stretch magnitude-dependent response	Yang et al. (2004)
Pulmonary fibroblasts	Increase in procollagen production	Cyclic stretch	Synergistic action of serum growth factors with mechanical loading	Butt and Bishop (1997) and Bishop et al. (1998)
Osteoblastic cells	Increased cell proliferation	Cyclic stretch	Differential response to strain-rate	Kaspar et al. (2002)
Smooth muscle cells	Increased collagen I synthesis	Cyclic stretch	Stretch directs L-arginine transport and metabolism to collagen synthesis	Durante et al. (2000)
Adult cardiac fibroblasts	Increase in collagen III and fibronectin mRNA	Equi-biaxial static stretch	Differential regulation of collagen III and fibronectin by different types of loading	Lee et al. (1999)
Endothelial cells	Decrease in DNA synthesis	Cyclic and static strain	Inhibition of DNA synthesis by mechanical strain	Woodell et al. (2003)
Periodontal ligament fibroblasts	Increase in collagen and fibronectin synthesis	Cyclic biaxial stretch	Differential regulation of collagen type I and fibronectin by different tensile strains	Howard et al. (1998)
Bovine chondrocytes	Increase in collagen II and aggrecan mRNA	Hydrostatic pressure	Differential regulation of ECM by different types of load	Smith et al. (1996)

Table 1.1: Some examples of studies in the field of mechanobiology; the table underlines the cell type studied, its response to a specific load, and the relevance.

Innovative experimental and theoretical methodologies are needed in future research studies to correctly quantify and classify the type and magnitude of the mechanical stimuli, both at the cellular and molecular level, in order to further understand the relationship between these and the cascade of intracellular signal transduction factors.

1.1.1 Mechanobiology in Heart and Brain

Cardiac tissue is subject to dynamic mechanical stresses from very early development to the rest of a person's life. Shear stresses that cardiac cells go through can be pulsatile, oscillatory or even turbulent, and portions of the heart experience both active stretching during filling and self-generated mechanical force during ejection. In the adult human heart, cardiomyocytes can remodel in response to changing loads or conditions, often in a compensatory fashion and sometimes pathologically. The recent discovery of some adult cardiac stem cell populations show that the heart is able to repair small areas even during adulthood.

Studies have demonstrated that mechanical conditioning by direct stretching can affect cardiomyogenesis. Illi's group discovered that laminar shear flow of 10 dynes/cm² over cultures of mouse embryonic stem cells resulted in an upregulation of expression of some cardiac markers [9]. Moreover, these markers increase when cells are plated on substrates with a very narrow range in elastic modulus, centred around 10 kPa. Other studies found that direct stretch of cardiomyocytes can directly affect the activity of several ion channels and increase gap junction-mediated cell coupling [10]. In particular, experiments on neonatal rat atrial cells have shown that 13% biaxial strain results in differences in gene expression of specific potassium channels and currents, ultimately resulting in reduced action potential duration. In addition, it has been shown that cell shape also plays a role in influencing the maturation and development of an aligned sarcomeric structure in neonatal cardiomyocytes. The use of geometric boundaries that force neonatal rat ventricular myocytes to spread into an elongated shape leads to more sarcomeric alignment and a clear direction of contraction [11]. Finally, electrical stimulation of the cells can induce beating, creating a dynamic loading of cell-matrix connections as well as portions of the cytoskeleton without the need for direct stretch. Heidi's group proved that neonatal rat cardiomyocytes stimulated by an electric field in the direction of a micro-pattern-induced alignment increase elongation [12]; another group discovered that neonatal rat cardiomyocytes were more excitable and expressed more connexin-43, which is responsible for gap junctions formation, when stimulated with electrical pulses during culture [13].

An increased attention has been recently given to the role of biomechanical forces on brain tissue and neuronal functions. Both micro and nano-technological techniques have been employed in order to understand the effects these forces might have on both brain development as well as disorders [14]. A growing number of recent studies has been focusing on neuronal development and homeostasis by attempting to understand the interaction of biomechanical forces that allow neurons to respond to mechanical stimulation [15]. These forces influence neurotransmitter release [19] and neuronal gene expression [16], as well as connectivity [17] and neurite [18] outgrowth, which emphasizes the importance of a molecular study of the mechanisms involved in these changes.

Even so, due to a lack of appropriate methods to investigate the microstructural elements of the brain, the research on the precise role these forces may play has produced limited results so far.

The role of mechanical forces on the human brain is subtly evident through the sensitive property of the brain, which enables microenvironmental forces to regulate various aspects of neuronal functions. An example of such an influence is seen in the effects of haemodynamic forces of blood flow that accompanies each heartbeat with forces capable of displacing neuronal tissue by several micrometres [20]. On an even smaller scale, the changes of the plasma membrane at the nanoscale heavily influence both the intercellular and intracellular environment, affecting processes such as ion channel exchanges [21], neurotransmitter release [22] and vesicle clustering [19].

The science of neuromechanobiology represents an integration of neuroscientific discoveries with mechanobiological techniques and it should improve our understanding of the interaction of mechanical forces and signal transduction pathways that regulate the growth of neuronal tissue. Studies in neuromechanobiology should provide greater insight into the primary consequences associated with the pathophysiology of neuronal viscoelasticity in traumatic brain injuries such as concussive ones [15].

1.2 Technologies for Mechanobiology

Although it is known that cell response to mechanical stimuli is closely related to tissue physiology and pathology, how cells sense forces and convert such mechanical signals into biological responses is not fully understood. We witnessed an increase in complexity in mechanobiology studies in the past decade, due to technological advances that have allowed detailed studies on a subcellular level, in particular studies at piconewton and nanometre force and spatial resolution, respectively, in live-cell conditions [23].

Microscale technologies enabled the diffusion of bioengineered tools for the study of the roles of mechanical forces in cell biology. Microelectromechanical systems (MEMS) allow to control the type and magnitude of forces experienced at the cellular and subcellular level and can be used to generate

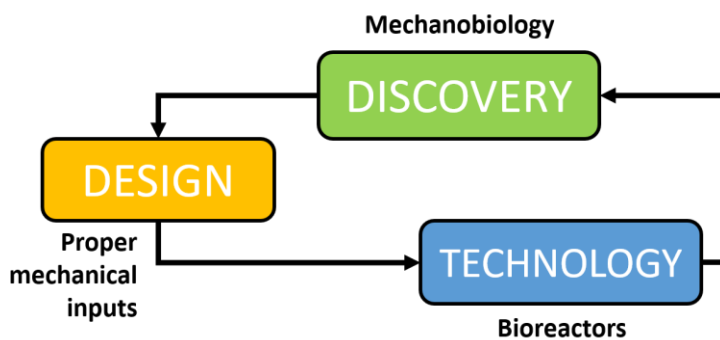


Figure 1.5: Phases in organ engineering [24]: design, technology and discovery of new biological phenomena such as mechanotransduction, which in turn influences further study designs that requires the development of more advanced and targeted technologies.

micromechanical environment *in vitro*, that resemble the *in vivo* situation, for the investigation of cellular processes in physiological and pathological conditions. Micromanipulation techniques can be based on magnetic, optical, or direct mechanical actuation. These capabilities have significant implications for cell and tissue development control and cell-based regenerative therapies.

Cell biologists and engineers developed instrumentations and novel cell substrates to apply regulated strain or shear stress on cells in 2D and 3D culture environments. Researchers tested different magnitudes of strain or shear stress, directions of fluid flow, durations of applied force, and measured a subsequent biologic response. The application of loads or shear stress to cultured cell-populated constructs for implantation in the body was one of the most significant outcomes of the basic science in mechanobiology [25, 26, 27].

Quantitative investigations of how cells sense and respond to mechanical stress depend on the techniques we use to apply a controlled mechanical force to living cells and to simultaneously measure changes in cellular deformation and alterations of molecular events. Below I list the major micromanipulation techniques that have been used to manipulate cells, nuclei, cell membrane, and cytoskeleton and that can be coupled with microscopic analysis of intracellular signalling.

1. **Micropipette aspiration.** To measure the mechanical properties of a single cell, it must be deformed in some way by a known force or stress, and its deformations must be measured. A classical technique for quantifying the mechanical properties of individual cells, such as elastic modulus and viscosity, concerns the use of a micropipette to apply a stress on the cell membrane. In particular, through this technique it is possible to apply a low-magnitude, negative pressure to deform a cell, and elongate a portion of it into the micropipette.
2. **Osmotic pressure.** Cell membrane deformations are induced by varying osmolarity of the medium and consequent changes in osmotic pressure. The data from these deformations is then correlated with changes in electrophysiological recordings.

3. **Microcantilever-based force sensors.** The atomic force microscope (AFM) involves the use of a tip, attached to the free end of a microcantilever, that is operated to deform a cell. From the cantilever deflection, the local stiffness of the cell can be calculated, and a map of its stiffness over the cell surface can be obtained. The measurements can provide valuable insights into the cytoskeletal structure and the effects of environmental parameters upon it.

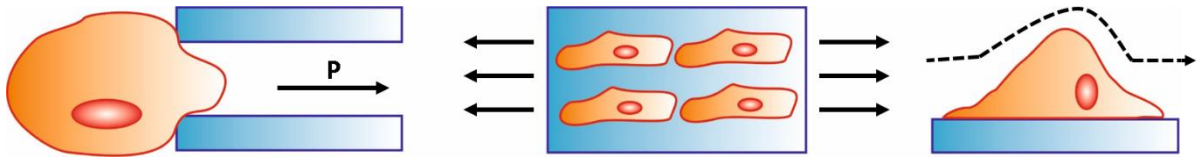


Figure 1.6: From the left: micropipette aspiration, micro-mechanical stretching device, and shear stress in microfluidic devices.

4. **Micropost arrays.** Mechanical stress exerted at cell-substrate and cell-cell interfacial boundaries can be measured using microfabricated silicone elastomeric post arrays [28]. In this method, forces are quantified by measuring micropost deflections, which deforms elastically (fig. 1.7).
5. **Magnetic tweezer and optical trap.** Magnetic microbeads are driven by the magnetic fields created by magnetic tweezers to apply mechanical forces on molecules such as integrins. In optical traps, the forces are applied axially or laterally onto microbeads by a focused laser beam, which attracts dielectric objects such as the beads (fig. 1.7).
6. **Microfluidic shear devices.** Fluid shear stress is one of the most important mechano-stimuli that occurs in a variety of physiological, pathological and embryogenic conditions. For example, stem cell development and differentiation depend on the fluid shear stress [29, 30]. In order to improve the reliability and resolution of mechanobiology systems, microfluidic systems were developed. Moreover, one of the important advantages of microchannels over conventional flow chambers is their ability to generate a wide range of shear stresses for the investigation of cellular responses to different type of mechanical stimuli.
7. **Micromechanical stretching devices.** Mechanical strains of the substrate to which cells are attached can be induced in a controlled way using different substrate technology in order to achieve uniaxial stretching, substrate bending, or in-plane substrate distension. Many typical cell stretching devices can only apply uniaxial or biaxial strain to the cells, while others can apply only radial strain. These devices are divided into three categories in relation to the different power sources, which include electric motors, dielectric elastomer actuators and regulated vacuum pressure. These cell stretching devices have more or less a similar mechanism of

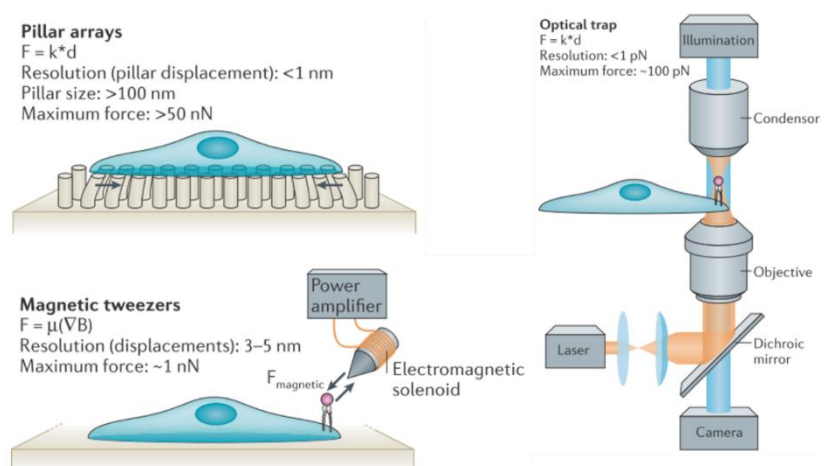


Figure 1.7: Schematization of pillar arrays, magnetic tweezers and optical trap technologies, for which the main characteristics such as resolution and maximum force are shown. (∇B = magnetic field gradient; d = distance; F = force; k = spring constant; μ = magnetic moment) [1].

applying a mechanical force on cells and tissues: applying a deformation to a stretchable membrane while cells are cultured on its surface (fig. 1.8).

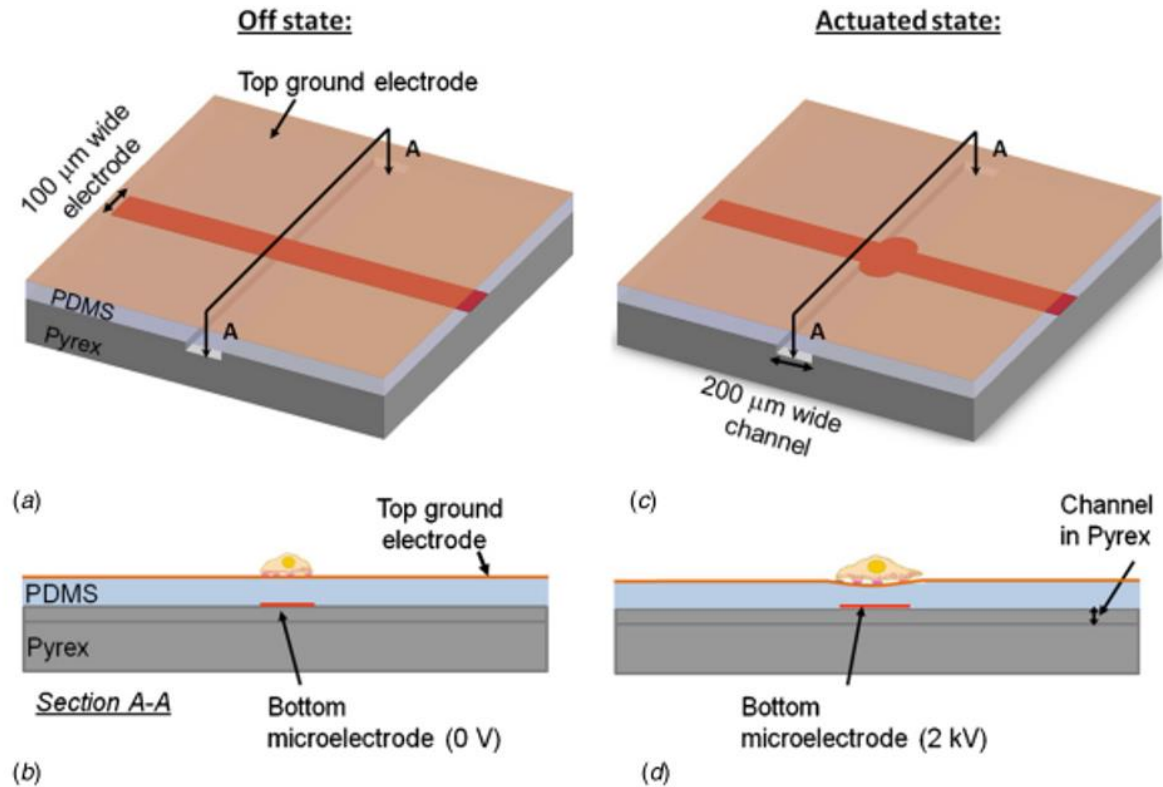


Figure 1.8: (a) Schematic of one cell stretcher and (b) its cross-sectional view (section A-A) showing a single cell adhered on top of the actuator at the off state. (c) Actuated state of the device, explaining that when a high voltage is applied to the bottom microelectrode, the membrane compresses in thickness and expands uniaxially. (d) Cross-sectional view of the actuated state of the cell stretcher, showing that a single cell attached on the actuator is stretched with the substrate [31].

8. **Ultrasound manipulation.** Ultrasonic fields can exert forces on cells and other micron-scale particles. The role of the ultrasound is usually to transfer energy from a convenient location for its generation, through transduction of electrical to mechanical energy by piezoelectric material, to a location where it is applied. For example, ultrasound may be applied to the surface of the human body for non-invasive hyperthermic surgery [32], or it may be applied at a remote location in a lab-on-chip system to control or sort particles within a microfluidic channel [33]. Ultrasound has also been coupled with piezoelectric nanoparticles (fig. 1.9) to perturb mechano-sensitive channels and generate electric fields to trigger calcium influx [34].

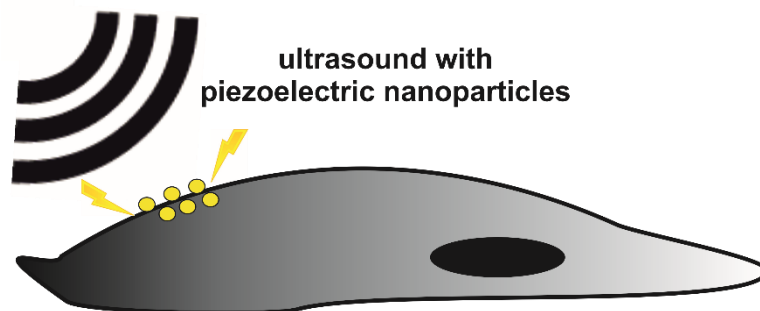


Figure 1.9: Ultrasound coupled with piezoelectric nanoparticles.

1.3 Mechanoelectric Coupling

As mentioned in the abstract, this thesis work is about the development of different experimental set-ups to perform mechanobiology studies and, in particular, for the investigation of cell mechanoelectric coupling.

The term mechanoelectric coupling (MEC), or, more specifically, mechanoelectric feedback, refers to the intra-cardiac mechanically-induced electrophysiological phenomena. In the 1915 Francis Arthur Bainbridge observed that right-atrial distension in anaesthetised dogs results in an acute increase in heart rate as a proof of the correlation between mechanical stimulations and electrical response in the heart. The past five decades have provided significant progress in MEC research, thanks to the development of new engineering-based experimental tools. A representative example is the demonstration by some recent studies that an orderly phasic stretching of cardiomyocytes contributes to the proper development of their function [35] and electrical activity [36]. The advances in computational modelling have enabled the integration of high-order data resulting from diverse spatial and temporal investigations, which, in turn, allow for the generation of new hypotheses [37].

Other technological innovations in the field of MEC studies include:

- transparent, hydrogel-based stretchable ionic conductors and large-strain actuators, in which electromechanical transduction is achieved without an electrochemical reaction [38];
- transparent, light-activated bio-compatible glues [39], that may allow novel approaches to non-contact electrical mapping during targeted mechanical interventions in native tissue;
- multiplexed electronic sensor and actuator devices that are flexible and stretchable, to overcome limitations of performing high-resolution electro-mechanical contact mapping *in vivo* on the contracting heart [40, 41].

1.3.1 AFM as Tool for the Mechanical Characterization of Cells

The use of atomic force microscopy (AFM) for probing living cells started in the early 1990s [42]. AFM is a powerful tool for cellular and molecular mechanics *in vitro* studies, in fact, it can provide information about the cytoskeletal structure and the effects of environmental parameters on it. The AFM probe can induce cell deformation and measure the force the cell applies comparable to those in many physiological conditions *in vivo* [e.g., in muscle contraction and expansion or axonal injury (>50% strain)].

The recent advances in micro- and nanofabrication techniques, have led to the development of new types of microcantilever-based MEMS devices to probe cell mechanical responses, such as cell stretch force response, cell indentation force response, and to observe *in situ* the cytoskeletal components during the mechanical stimulation, under large deformations in the range of 1 nN to 1 μ N of applied force.

Galbraith *et al.* [43] used a microfabricated device capable of determining subcellular forces generated by individual adhesive contacts to measure traction forces generated by fibroblasts. The device can continuously monitor forces exerted on adhesive contacts.

Yang and Saif [44] developed a microfabricated force sensor allowing measurements of the responses of adherent fibroblasts to stretching forces. Force responses of single cells were measured before and

after the administration of an inhibitor of actin polymerization (Cytochalasin D) and this treatment suggested that actin filaments are the most involved in the cells internal forces due to stretch.

In a recent study, in order to quantify mechanical changes of the *zona pellucida* of mouse oocytes, MEMS force sensors were developed that convert microcantilever deflections into capacitance changes. These changes were measured before and after fertilization [45], as well as before and after interactions with drug-delivery microcapsules [46, 47]. A further development of polydimethylsiloxane (PDMS) microcantilevers allows the measurement of cardiomyocytes contractile forces in real time [48, 49], though large deformations were optically measured due to the low Young modulus.

Another study developed an array of silicon cantilevers overhanging microfluidic channels in order to measure masses of cells adhering to their surface (fig. 1.10) [50]. This approach permits probing force responses of live cells in near physiological condition noninvasively, especially when combined with microfluidic cell culture techniques, as well as it provides optical observations of the same cells.

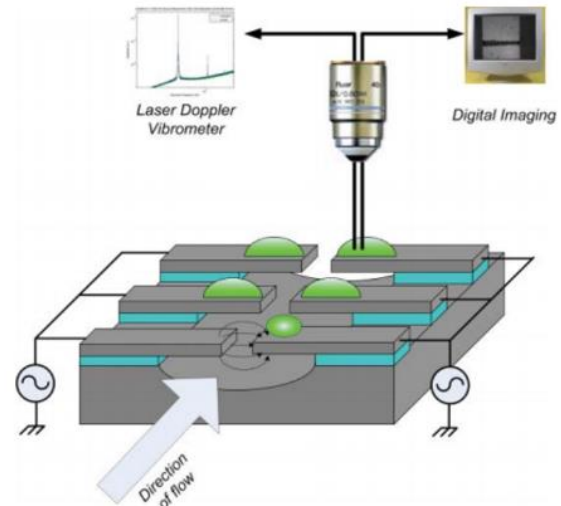


Figure 1.10: Diagram of a cantilever array. Target cells in suspension are immobilized on the cantilever; these are cultured, and their mass is measured via the resonance frequency shift of the cantilever [50].

When considering the field of mechanoelectric feedback, some systems dedicated to the study of the electrical cell response after a deformation have been proposed. Although it is of vital importance to record both the mechanical and electrical activity of an heart cell undergoing cardiovascular drug treatment to better understand heart pathophysiology and to improve existing *in vitro* models, most of the published attempts to measure simultaneously the electrophysiological and the mechanical properties of cardiomyocytes were not easy to be implemented.

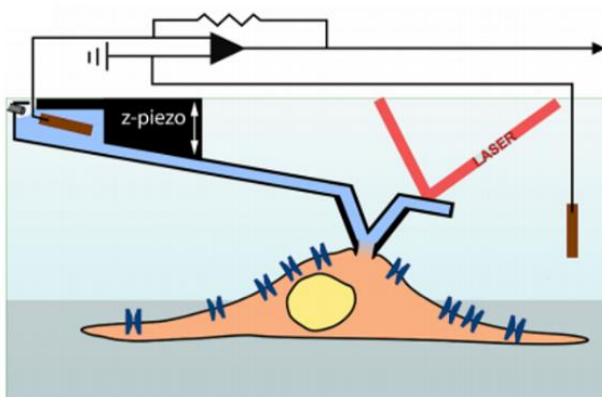


Figure 1.11: Illustration of the FluidFM setup in whole-cell configuration. The tip aperture allows connecting the electrode inside of the pipet with the cytosol. The patch-clamp electronics clamps the transmembrane potential [51].

As an example, Ossola *et al.* [51] merged the patch clamp electrophysiological recording and AFM, thus equipping the patch-clamp pipette with the sensitive AFM force control to investigate cellular topography together with electro-mechanical properties. This was possible using the so-called FluidFM technology, a force-controlled nanopipette based on microchanneled AFM cantilevers (fig. 1.11).

Liu *et al.* [52] characterized the nanomechanical properties of acutely isolated cardiomyocytes with the torsional signal of an AFM cantilever. They used an AFM combined with a confocal light microscope to detect simultaneously the change of signal molecular fluorescence.

Pesl *et al.* [53] have recently developed a system to characterize *in vitro* clusters of human induced pluripotent stem cells (hiPSC)-derived cardiomyocytes. A single cell cluster was integrated into the AFM force-sensing platform and coupled to the microcantilever probe providing a micromechanical cellular biosensor suitable for whole-day testing (fig. 1.12).

Small biosensors, such as microelectrode arrays (MEA), can be engineered to comply with AFM and optical microscopy systems for cardiac investigation [54, 55]. The attractiveness of MEA-based electrophysiology resides in its ability to multiprobe extracellular field potentials (EFP) of electroactive cells in a non-destructive fashion, which allows for prolonged and complex measurements of cells and tissues. Tian and his group [56] published a work in 2017 that shows an AFM-MEA integrated system similar to the one in this study. This group developed a platform combining the microelectrode array and AFM to detect the electromechanical activities in cardiomyocytes. The extracellular potential and beating force were recorded simultaneously by the platform with the low noise level and the feasibility of the experimental platform was verified by a drug test.

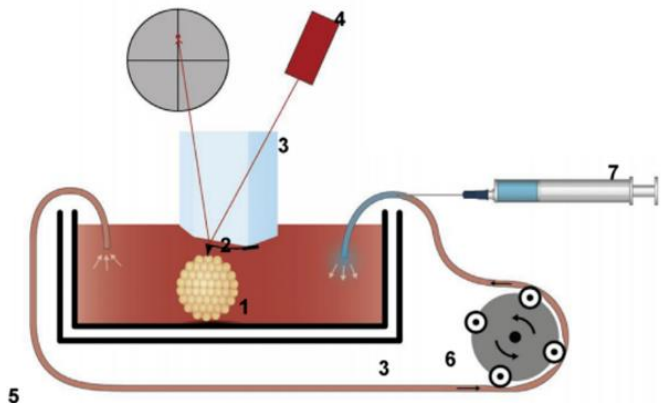


Figure 1.12: Scheme of the biosensor setup used for biomechanical characterization of cardiomyocyte clusters. Main elements of the setup are: 1-Embryonic body, 2-AFM cantilever, 3-glass cantilever holder block, 4-AFM laser source and photodetector of laser position, 5-plastic (PP) tubing, 6-peristaltic pump, 7-syringe for drug injection [53].

1.3.2 Mea Devices as Tool for the Electrical Characterization of Cells

A microelectrode array (MEA) is a two-dimensional arrangement of voltage probes designed for extracellular stimulation and monitoring of electrical activity of electrogenic cells, such as neuronal,

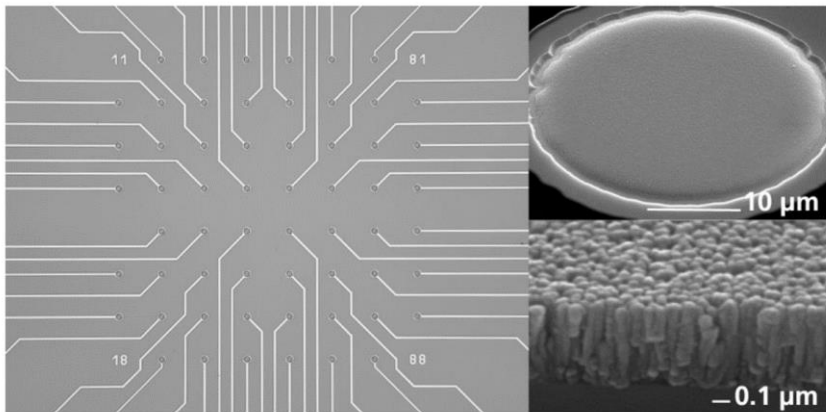


Figure 1.13: On the left, an example of micro-electrodes layout; on the right, electron microscopy image of a TiN covered planar electrode.

muscle, and cardiac tissue. A typical MEA consist of a glass slide into which an integrated array of microelectrodes has been photoetched, coated with conductive materials such as titanium nitride (TiN), indium-tin oxide (ITO), palladium or gold. A standard MEA system has a square recording area up to 5 mm length, where 60 electrodes are aligned in an 8 x 8 grid with inter-electrode

distances of 100, 200, or 500 μm . Planar TiN (titanium nitride) electrodes have diameters spanning from 10 to 30 μm , while three-dimensional TiN electrodes have a diameter of $> 12 \mu\text{m}$ at the base with a very fine tip. Most MEAs include a substrate-integrated reference electrode, and all electrodes can either be used for recording or for stimulation. Typical commercial systems have an

instrumentation noise level optimized to 5-10 μV in amplitude. This value is generally better than the voltage noise coming from a standard TiN electrode, which spans between 10-30 μV [57].

As various are the applications for MEA devices in the fields of neurobiology and cardiac electrophysiology, this technology has become accessible to any electrophysiological lab. Typical neurobiological applications are: ion channel screening, drug testing, pharmacology studies, microencephalograms (EEG). Typical applications in the cardiac field are: activation and excitation mapping, measuring of the conduction velocity, long-term characterizations of cell types (especially stem cells), culture pacing, drug testing, pharmacology studies, monitoring of QT-related prolongation and arrhythmias.



Figure 1.14: A typical MEA device by Multichannel System.

The recording and stimulation performances of these devices are not optimal for single cells measurements. Typically, the amplitudes of the local field potentials (LFPs) range between 10 μV to 1mV, for neuronal cultures, whereas for cardiomyocytes these values increase with the developmental stage [58]. These amplitude values of the detected signal can be understood when we consider the electrical environment in which these are recorded from.

As shown in figure 1.15, the model of the structural relationships between an electrogenic cell and a substrate-integrated planar electrode includes three components [59]:

- the electrogenic cell;
- a cleft formed between the cell and the substrate surface;
- the electrode.

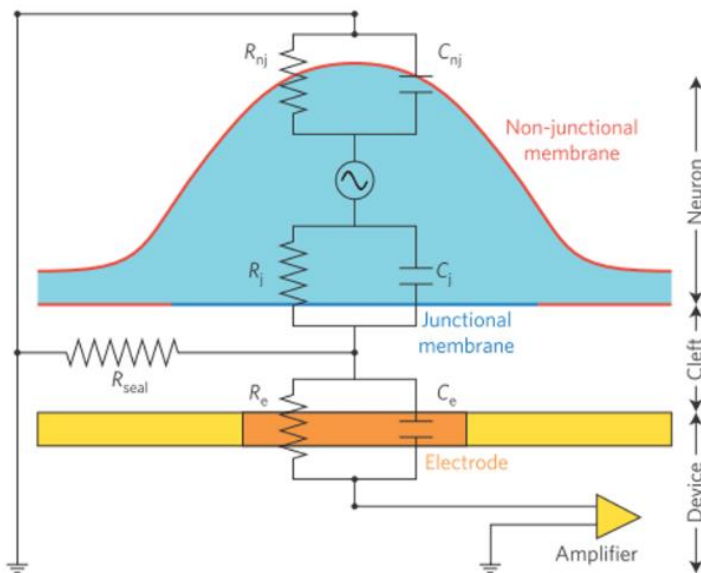


Figure 1.15: Circuitual equivalent of the electrode-cell system, for a passive planar metal electrode [59].

The plasma membrane adheres to MEA surface by electrostatic or chemical interactions between cell adhesion molecules and the ones deposited on the MEA platforms to promote cells attachment, such as ECM proteins or their synthetic equivalents. The cleft formed between the cell membrane and the MEA substrate is filled with the ionic solution of the bath. As it can be observed in the model (fig. 1.15), only a small fraction of the membrane (defined junctional membrane, R_jC_j) is in contact with the metal electrode, providing the interface between the cell and the sensing pad. The physiological solution within the cleft generates the

seal resistance (R_{seal}) to ground. When an action potential occurs, only a fraction of the ionic current flows through the bath solution in the cleft thus creating a voltage loss. This voltage formed over R_{seal} directly modulates the charge distribution across a passive metal electrode, allowing the differential detection with respect to a reference electrode in the bath [60]. The opposite terminus of each

electrode extends to the periphery of the chip, and makes contact with an external amplifier, which relays the electrical signals to a computer for analog to digital conversion, filtering, signal detection, storage, and analysis [61].

To perform the data analysis, it is necessary to consider [62]:

- the cellular signal sources and the tissue allowing spread of ionic current;
- the contact between the cell and the tissue, respectively, and the electrodes;
- the substrate and the embedded microelectrodes;
- the external hardware with stimulators and filter amplifiers connected to the electrodes.

Microelectrode array systems are a key technology for the study of *in vitro* electrophysiology, as they allow the possibility of testing different chemical reactions, testing negative and positive control on the same nominal culture, and to be further improved for the study of 3-dimensional network or patterned models [60, 62].

1.4 Cell Patterning for Specific Investigations

The ability to control the positions of cells in an organized pattern on a substrate has become increasingly important for the development of cellular biosensor technology, tissue engineering applications, high throughput drug screening systems, and, in general, for cell biology studies. The cell culture geometry has a big relevance when complex multicellular tissues such as myocardium or bone are involved.

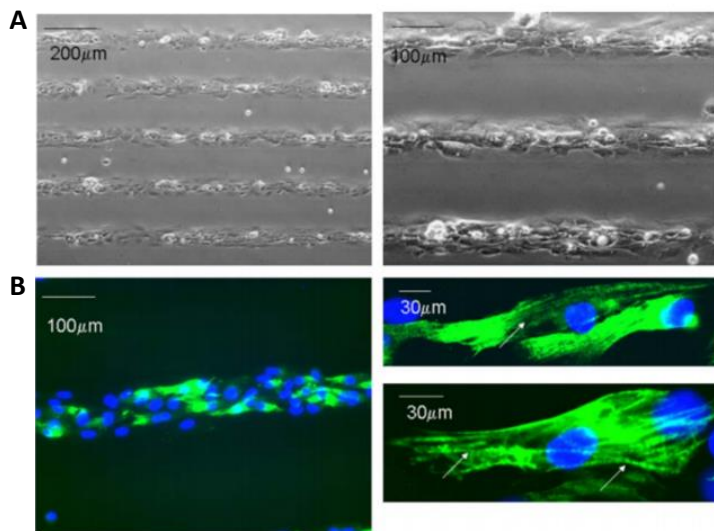


Figure 1.16: A) Neonatal rat cardiomyocytes seeded on chitosan patterned glass surfaces at 8 days of culture; B) Patterned cardiomyocytes express cardiac troponin I (green) and exhibit a developed contractile apparatus (arrows) [67].

engineering applications require that cells can be specifically placed to generate organized structures, such as a neural network (fig. 1.17).

Micropatterned ECM islands can constrain cells to a certain shape by culturing cells in the corresponding, confined areas: single cells can spread over multiple islands or can be confined to a single island, even in unnatural geometric shapes, such as

Cell patterning is also useful to precisely position cells on top of recording/stimulation planar devices. If we consider MEA devices, it could be useful to study the propagation of cells signal in specific directions, so it is fundamental having cells just upon the electrodes of interest. Similarly, automation technologies to perturb and observe cells serially requires that cells are positioned into addressable arrays that can be accessed, for example, by a motorized stage. Finally, tissue

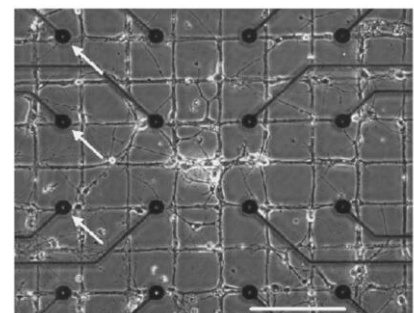


Figure 1.17: Neuronal pattern on microelectrodes array obtained using microcontact printing technique [66].

squares and triangles [63, 64]. Using this technique, it has been determined that cell death or proliferation can be controlled through constraints on the area of cell spreading, indicating that the resulting mechanical perturbations play an important role in determining cell fate [63]. Moreover, the capability of patterning ECM islands on the size scale of individual focal adhesions ($\sim 1\ \mu\text{m}$) has enabled the investigation of specific roles of focal adhesion positioning in directional control of cell spreading and movement through specific protein activation [65].

1.5 The Importance of the Substrate: Stiffness and Topographical Cues Can Influence Cell Response

The topography of cell-substrate interaction areas plays a major role in tissue engineering and cell-based regenerative therapies. Living tissues are intricate aggregates of different cell types embedded in complex and well-defined ECM structures with micro- and nanoscale topographical features. The functions of many cell types can be significantly affected *in vivo* by topographical stimulation from the surrounding ECM. For a better understanding of the cellular processes derived from the interactions between cells and their underlying ECM topography (e.g., aligned fibrillar matrices,

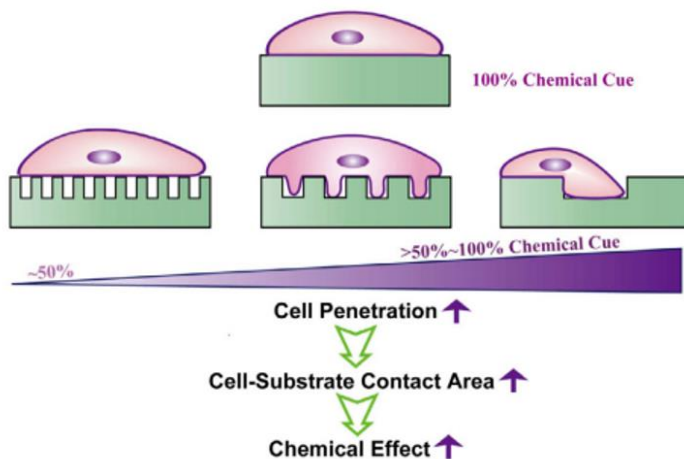


Figure 1.18: Model of the cooperative interplay between immobilized heparin and substrate topography in regulating cell behavior [71].

shape, texture), micro- and nanotopographic substrates have been developed, which, in turn, may allow researchers to ultimately tune cell function with topography-controlled biomaterials for advanced tissue engineering [68].

As mentioned, cells remodel and conform themselves to the physical environment in which they live. For example, even cell seeding density can influence cellular metabolism, migration, proliferation, and differentiation. This knowledge has

encouraged the development of biomaterials that possess the ability to change their mechanical and chemical properties, including porosity, stiffness, cell-attachment sites, and hydrophobicity/hydrophilicity.

Several micro-/nano-fabrication technologies, such as nano-imprint lithography, laser holography, and laser machining have offered powerful tools to create artificial substrates with controlled micro- and/or nano-topographical features (e.g., grooves, ripples, islands, pillars, particles, dots, etc.), but the past decade electrospinning has particularly demonstrated its significant impact on the fabrication of engineered tissue scaffolds [69].

In particular, the characteristic of the substrate can be crucial when we are using stem cells. In fact, the culture conditions must be optimized to control their differentiation. Recent studies have shown that a combination of substrate topography and cytokine cocktail may efficiently expand the hematopoietic stem/progenitor cells (HSPC), and advantageously control their lineage commitment [70]. If a topographical cue can supplant even partially the required biochemical cue to mimic a stem cell niche it would be an appealing and cost-effective strategy. Scaffold design so far has concentrated

mostly on the macroscopic 3-dimensional aspect and the inclusion of drug and gene delivery functions, but limited attention has been paid to the topographical features of a scaffold, as it is important consideration in designing a biomimetic microenvironment for tissue engineering and regenerative medicine.

A deeper consideration of the topographical phenomena will be achieved as more studies emerge, but, as of now, it is difficult to compare individual studies and establish a general trend. That is because researches study cells ranging from fibroblasts to mesenchymal stem cells, and it has been considered that different cell types may respond differently to a given topography. Studies are also conducted on substrates differing in chemical composition and mechanical properties which are known to influence cell-substrate interactions too. Eliminating these variables would be important for future studies in order to define the relationship between structure and function.

The parametric space within which lie the geometry, size, and pattern of the topographical features of the cells that are studies should be investigated. However, even without the detailed knowledge of these features, further studies could potentially improve our understanding of the mechanobiology processes, which could in turn lead to new designs.

1.6 Conclusion

The understanding of how mechano-sensing processes interplay with intra-cellular signalling pathways would permit researchers to fully comprehend the many relevant pathological and physiological processes such as cell growth in cancer and aging. It is difficult to study the effect of force signalling over time because cells respond to mechanical and biochemical signals in a timescale of seconds to minutes, whereas tissue formation occurs over weeks to months. Even if mechanical stimuli are significant in influencing cell activity, however, we poorly understand how to control or modify their effects. It is clear that cells actively test their environment both chemically and mechanically, and adopt specific cell responses depending on matrix stiffness, neighbouring cells, hormone levels, nutrients and other factors. Newly available nanotechnology and advanced microscopy tools can enable us to map when and how cells make decisions to grow, to undergo apoptosis, or to differentiate. Only when we will understand which mechanosensing and signalling pathways are activated, in what sequence and how often, in healthy and injured cells, we can possibly mitigate disease-related damages more specifically and facilitate repair processes.

Chapter 2

The Atomic Force Microscope

During my PhD I employed the Atomic Force Microscope (AFM) in different ways that will be discussed in detail in the next two chapters. First, I used this instrument to image the topography and perform mechanical characterization of different types of hydrogels which are employed as cell scaffolds. More interestingly, the idea to use the AFM probes to stimulate mechanically excitable cells plated on recording electrodes was investigated, and thus, a dedicated experimental setup was implemented for the purpose.

This short chapter explains the operating principles of the AFM and provides a brief overview on the modes to obtain images, on the available AFM probes, and an elucidation of what force-distance curves are.

2.1 Introduction

“Just as an optical microscope produces a two-dimensional image through the interaction of light and matter, the scanning probe microscopies (SPMs) produce three-dimensional images through the interaction of matter and matter, the first “matter” being the sample and the second “matter” being a small, usually sharp probe. [...]

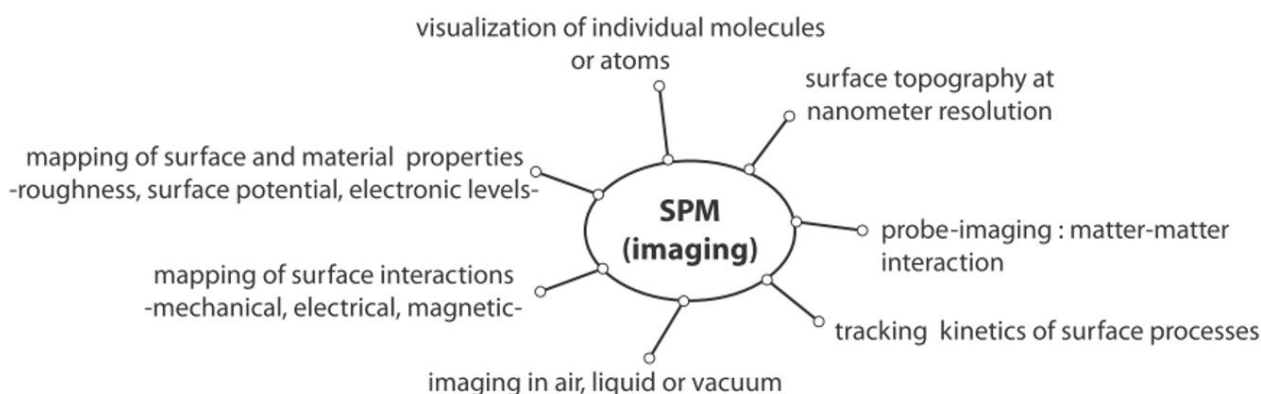


Figure 2.1: Scanning probe microscopy applications [72].

The scanning probe microscope can be considered as the technical analogy of a human deprived of eyesight. Under this condition, we humans sense nearby objects with the help of our hands or sticks. As we move forward, we intuitively probe our immediate environment by moving our hands or sticks in a systematic manner, for example, from left to right or up and down. Whenever we encounter an obstacle, we follow its contour by sliding or tapping our sticks or fingers over its surface. If the object were a hot plate, we would in this case not touch it and burn ourselves after sensing the heat, preferably at a safe distance. A scanning probe microscope shares the human intuition in sensing

objects and so behaves as a blind device that can detect micro- and nanosized objects. The instrument's stick is a probe ended in a nanometer- sized tip that is brought in contact or in close proximity to the sample surface. The probe is moved over the sample surface in a probe-moving setup (or vice versa, in a sample-moving setup) with great precision by means of a piezo-driven device. Finally, the instrument is equipped with a means to get the tip's (relative) position at any time and a feedback mechanism to control either how "hard" the tip should slide or tap or how "close" the tip should be kept from the sample surface. In both cases, the tip will follow the contour of the object by scanning it from left to right, from right to left, and up and down in a raster manner. All the SPM variants are based on one of the two most typical instrumental configurations: that of the scanning force microscope, also called atomic force microscope (AFM), and that of the scanning tunnelling microscope (STM).

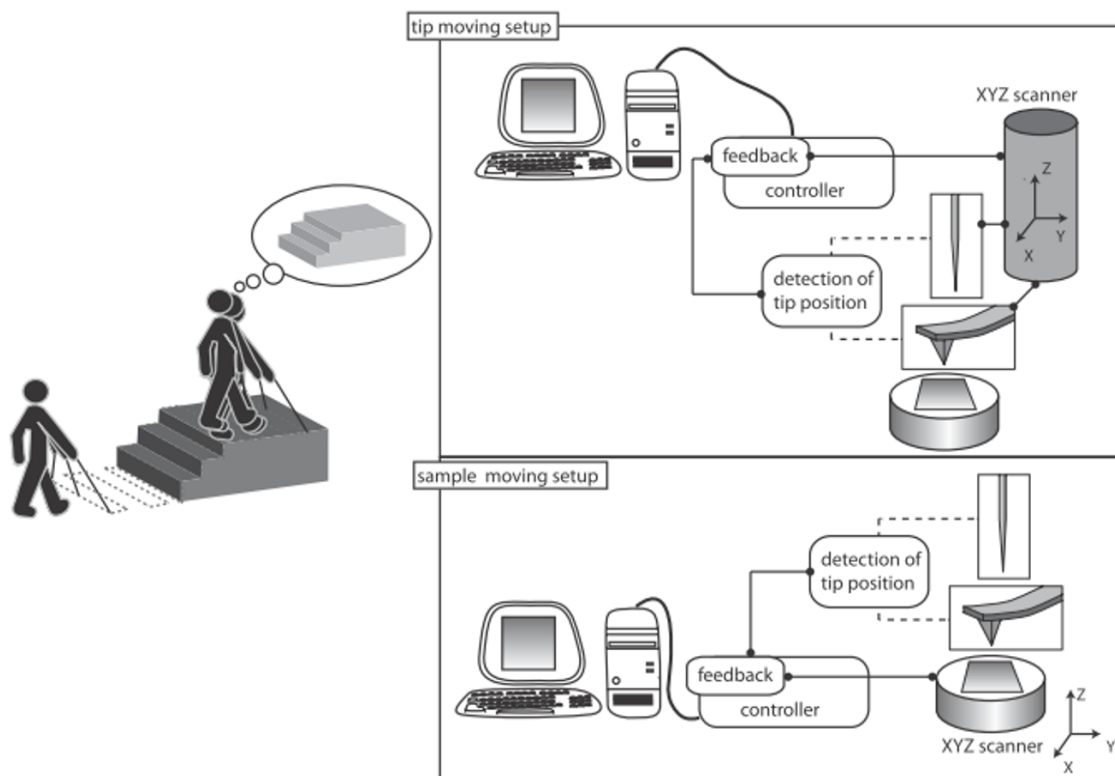


Figure 2.2: The image shows the comparison between the SPM and a human deprived of his eyesight: by moving the stick, the person can figure out how the object looks; on the right side of the figure, the general configuration of an SPM, either in a tip-moving setup or in a sample-moving setup, is shown. The instrument is equipped with a sharp pointed probe, that can be a metal wire (STM) or a sharp object attached to a cantilever (AFM) moved in any direction by a piezo scanner. In addition, the instrument includes a detector to register the tip's position (x, y, z) at all times and a feedback mechanism that controls the interaction of the tip with the sample [72].

In the AFM the probe consists of a sharp tip, with a typical radius of curvature (ROC) of 10-30nm that is attached to the free end of a micromachined cantilever. The instrument is also equipped with an optical mechanism to detect the tip's position with a four-quadrant position-sensitive photodetector (PSPD) that registers the reflection of a laser focused on the cantilever's free end."

These words, taken from the book "*HYBRIDIZING SURFACE PROBE MICROSCOPIES, Toward a Full Description of the Meso- and Nanoworlds*" by Susana Moreno-Flores and Jose L. Toca-Herrera [72], in my opinion, explain in a very effective way the principle of operation of scanning probe microscopy in general and AFM in particular. The next paragraphs provide a more specific description of the microscope characteristics.

2.2 Description and Operating Principles

Atomic Force Microscopy is a high-resolution surface microscopy technique, belonging, as explained in the previous paragraph, to the family of SPMs, whose operating principle is the interaction between the sample and a sharp probe, which is scanned over the sample surface following a raster path. SPM scanners are made of piezoelectric ceramic materials, which deform in response to an applied voltage. Scanners are properly designed to control in a precise way probe (or sample) movements.

During SPM image acquisition, the local probe-sample interaction generates, in each scanned point, a signal, which depends on the distance between the probe and the sample. Surface topography can thus be reconstructed, operating either in the so-called “constant-height mode” (probe vertical position is kept constant and the relative probe-sample distance is directly derived from signal measurement) or in “constant-signal mode” (a Z-feedback loop controls probe vertical position in order to obtain a specific signal value; topography is then reconstructed considering the vertical displacement of the piezo) (fig. 2.3).

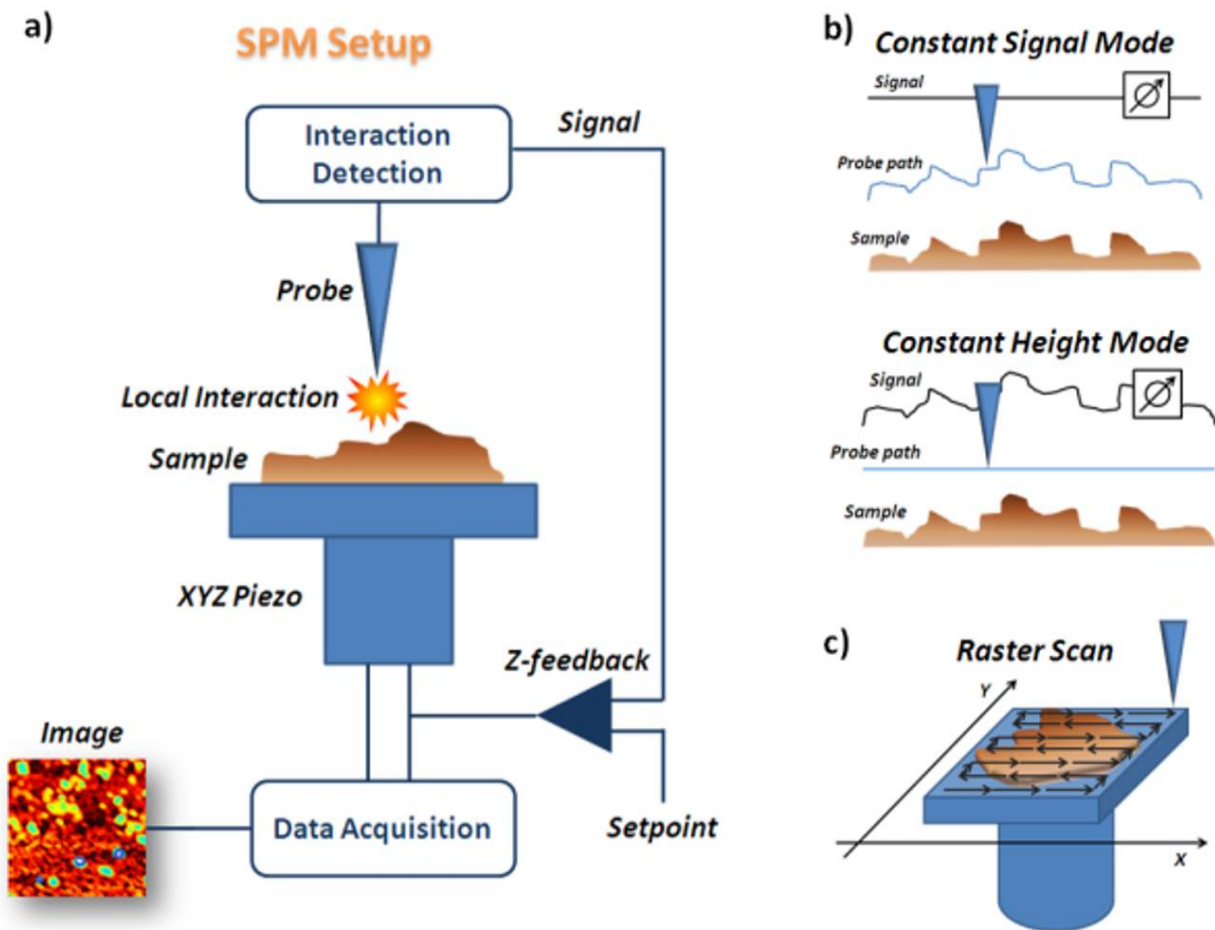


Figure 2.3: a) Schematic representation of a SPM; b) Different acquisition modes, with (constant signal) or without (constant height) Z-feedback loop; c) Probe scanning path in X (fast scan direction) and Y (slow scan direction).

The origin of SPM dates back to the early eighties with the invention, in 1981, of Scanning Tunnelling Microscope (STM) [73], for which Binnig and Rohrer won the Nobel Prize in 1986. In STM measurements, a bias voltage is applied between a conductive or semiconductive sample and STM probe, which consists in a sharp, conductive tip. When the tip gets close enough to the sample (typically 10 Å far), electrons start tunnelling through the gap. This tunnelling current depends exponentially on tip-sample distance, which can thus be determined with an extremely high precision.

STM allows imaging conductive or semiconductive flat surfaces with an atomic resolution. The first AFM was developed in 1986 by Binnig, Rohrer and Gerber [74]. Its working principal is based on the interatomic forces between the probe, generally a sharp tip attached to a suspended cantilever, and the sample. The great advantage of AFM, with respect to STM technique, is that it also works on insulating samples. Furthermore, it operates in a large number of working conditions, including air, vacuum, and liquid. Many scanning force microscopy techniques were developed in the following years, including magnetic force microscopy, electrostatic force microscopy, shear force microscopy, and Kelvin probe force microscopy.

Interatomic forces between probe and sample atoms are at the bases of AFM functioning. These forces can be of different nature (e.g. electrostatic, hydrophobic, magnetic) at higher distances. At shorter distances the prevailing interactions are anyway characterized by a longer-range attractive regime, where Van der Waals attractive forces prevail, and by a short-range repulsive regime, due to

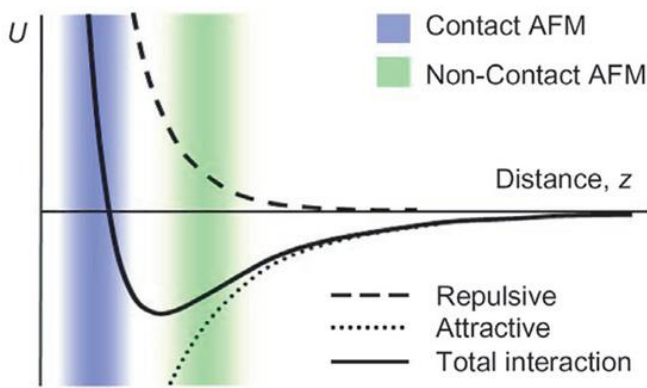


Figure 2.4: Inter-atomic force (U) vs. distance.

the overlapping of electron clouds and the repulsion between atomic nuclei (i.e. contact repulsion).

The most employed approach for quantifying cantilever deflection and this tip-sample interaction force is the one based on optical lever principle [75] where a laser beam is focused on cantilever surface, which is coated with a reflective material, typically gold (fig. 2.5). The laser spot is reflected on a position-sensitive photodetector (PSPD). In absence of interaction, laser reflection is centred on the

PSPD. Cantilever bending causes a displacement in laser spot position on PSPD, which is proportional to cantilever deflection. PSPD used in AFM are usually composed by a four segments photodetector, allowing the detection of both vertical and lateral cantilever deflections in the sub-nanometre range, since they are amplified by a quantity which depends on the optical path length.

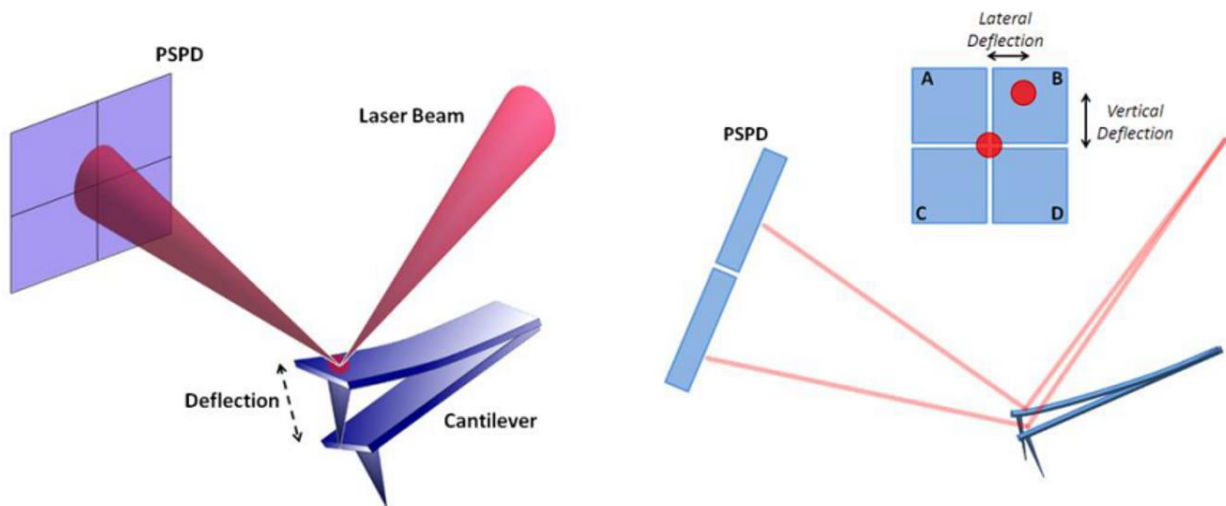


Figure 2.5: Illustration of AFM photodetection system: the cantilever deflection results in a shift in laser spot position on PSPD. AFM main signal (vertical deflection) is calculated from $(A+B)-(C+D)$, while frictional torsion (lateral deflection) is $(A+C)-(B+D)$.

An AFM cantilever behaves like a leaf-spring, following Hook's law, and its characteristics will be explained in detail in the last paragraph of this chapter.

2.3 Imaging

AFM topography imaging can be obtained using different methods, either static or dynamic, which exploit different interaction force regimes (fig. 2.6): they are indicated as contact mode, non-contact mode, and tapping mode. All AFM images related to my PhD project were obtained in contact mode, which is described in the following.

Contact imaging mode operates in repulsive regime, where the tip is pushing on the sample and positive force values are measured. Before starting, a force setpoint is chosen, generally low, in order to reduce the interaction with the sample, but high enough to overcome possible cantilever fluctuations. During scanning, the feedback system continuously compares the measured force with the setpoint, driving the piezo in order to maintain the force constant. Considering the relationship between force and deflection, the movement performed by the piezo should necessarily reflect sample profile.

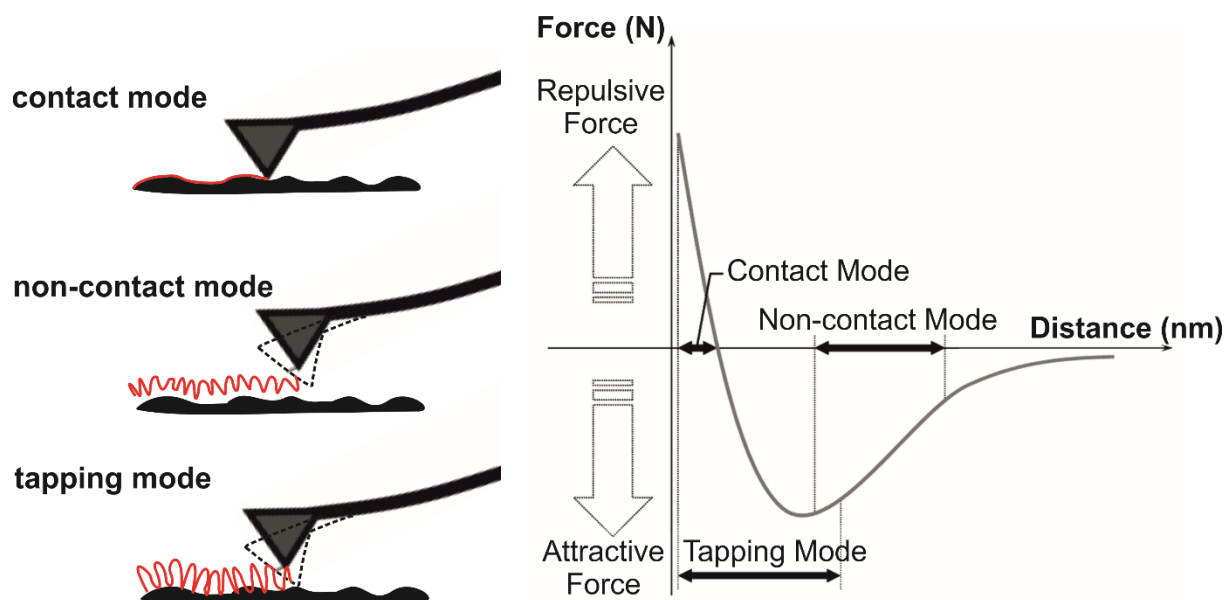


Figure 2.6: Illustration of the different imaging modes (on the left). On the right side of the figure, the regions of the three AFM modes are indicated: contact-mode operates in the repulsive region, the tapping and non-contact modes operate respectively in attractive/repulsive and attractive regions.

In tapping mode, the tip oscillates near the surface with a frequency close to the resonance of the system. The feedback parameter is the amplitude of oscillation: the more the tip gets close to the sample, the more the free oscillation amplitude is reduced. Thus, setpoint value has to be lower than free amplitude measured at the working frequency. Similarly to what happens in contact mode, piezo movement, performed to keep the amplitude constant, allows topography reconstruction. Intermittent contact involves both repulsive and attractive regime. Since repulsive contact forces are present only in the lower part of the oscillation, the interaction with the sample is extremely reduced with respect to contact mode, as well as the lateral force exerted during scanning. Thus, intermittent contact should be preferred in case of soft, delicate samples, such as the biological ones.

Even in non-contact mode cantilever oscillates near the surface, but in this case the whole oscillation stays within the attractive regime, and contact with the sample never happens. Stiff cantilever need

to be used in non-contact, in order to avoid a possible jump to the surface or jump to contact¹, which can be induced by attractive forces. Non-contact mode is not frequently employed, since it requires particular conditions, such as the absence of anomalies or other forces in the attractive regime, which are rarely verified in real cases, especially in liquid.

2.4 Force Distance Curves

The capability of the AFM probe to sense forces with high sensitivity can also be used to obtain other valuable information on sample properties apart from sample topography. Instead of scanning, in fact, cantilever can be moved along the vertical direction on a fixed X-Y position, starting from a distance far from the sample toward the contact regime, until a certain deflection (setpoint) is reached. Then the cantilever is retracted and brought back to the initial situation. During this movement, the cantilever deflection and, thus, the force acting on the tip can be measured and plotted against piezo displacement, generating a so-called force vs distance curve [76, 77] (fig. 2.7).

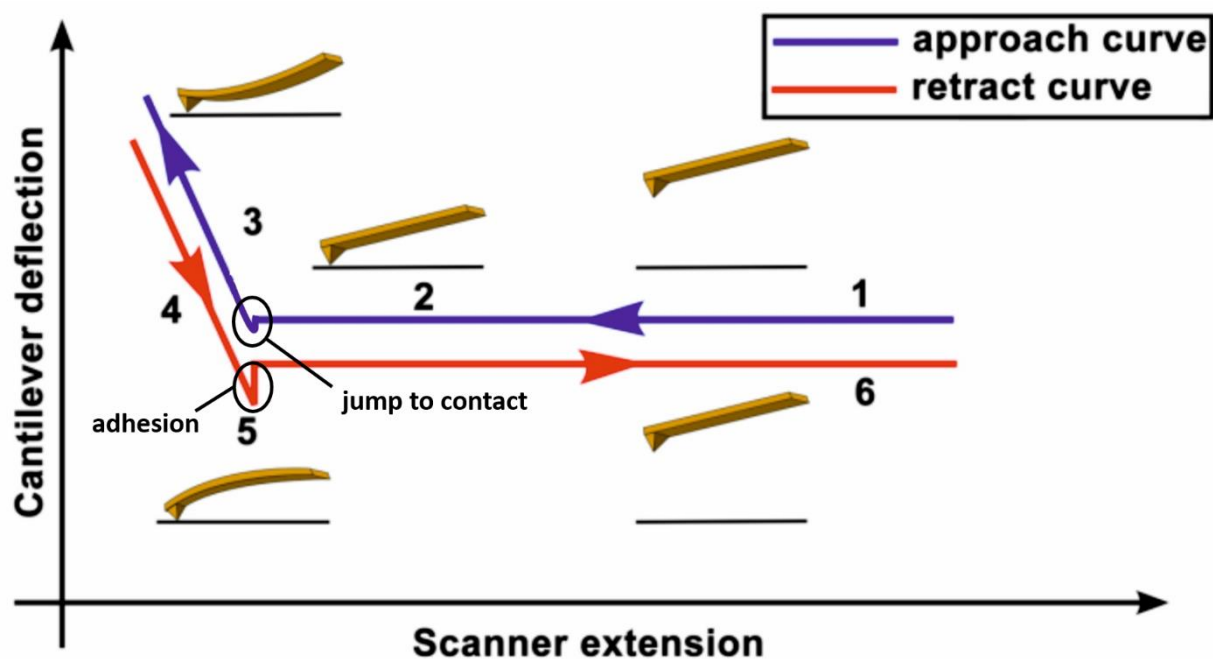


Figure 2.7: A typical force curve is shown: when approaching the surface, the cantilever is in an equilibrium position (1) and the curve is flat; as the tip approaches the surface (2), the cantilever is pushed up to the surface and deflected upwards, which is seen as a sharp increase in the measured force (3); once the tip starts retracting, the deflection starts to decrease and passes its equilibrium position at (4); as it is moved away from the surface the tip snaps in due to interaction with the surface, and the cantilever is deflected downwards (5); once the tip-sample interactions are terminated due to increased distance, the tip snaps out, and returns to its equilibrium position (6) [78]. The negative deflection preceding the linear part in the blue curve called “jump to contact” and the tip adhesion in the red one are shown: in the first case, the tip is driven towards the sample in presence of attractive interactions, in the second case, the cantilever deflects downwards because of adhesive phenomena.

The simplest situation we can consider is the one in which the measurement is done on a hard sample and in absence of long-range interactions. Before contact, cantilever is not deflected, and the measured force is zero. After having reached the contact point, force increases linearly with a slope equal to cantilever elastic constant. In presence of attractive interactions, such as Van der Waals or capillary forces, the tip is driven towards the sample before the contact regime: this “jump” is represented by a negative deflection preceding the linear part (fig. 2.7). Other kinds of long-range

¹ See paragraph 2.4 and figure 2.7.

interactions, such as electrostatic repulsion, can also be observed, especially when we are working in liquid environment.

When performing a force-distance curve on soft samples the AFM tip, once in contact, may induce sample deformation, which is represented by a non-linear behaviour of the curve in the contact regime. Once the applied force reaches the chosen setpoint, the probe is retracted from the sample (fig. 2.7). During retraction, the curve goes back to zero, sometimes displaying a hysteresis caused by viscous losses or plastic deformations. After having crossed the zero line, the tip may remain attached to the sample, due to adhesive phenomena: cantilever deflects downwards until the force is enough to overcome adhesion; then, the tip breaks free and the curve stabilizes at zero again (fig. 2.7).

In the last years, force-distance curves have been largely used to characterize biological samples. Single molecule force spectroscopy is used to determine the mechanical stability of single bonds or single protein molecules. Functionalized tips can be employed in molecular recognition, since the rupture of bounds between tip functional groups and specific molecules on sample surface can be identified through the analysis of characteristic features on the retrace curve.

2.5 AFM Probes

“In an ideal world where the probes were infinitely sharp and the surfaces infinitely flat, the SPM images would show the true profile of the samples, unaffected by any probe’s influence whatsoever. However, in the real world, the probes have a finite geometry, and though they are sharp, they always have a certain width and bluntness at the very end, which is defined by their radius of curvature. Likewise, the real world samples are far from being atomically flat; rather, they are more or less

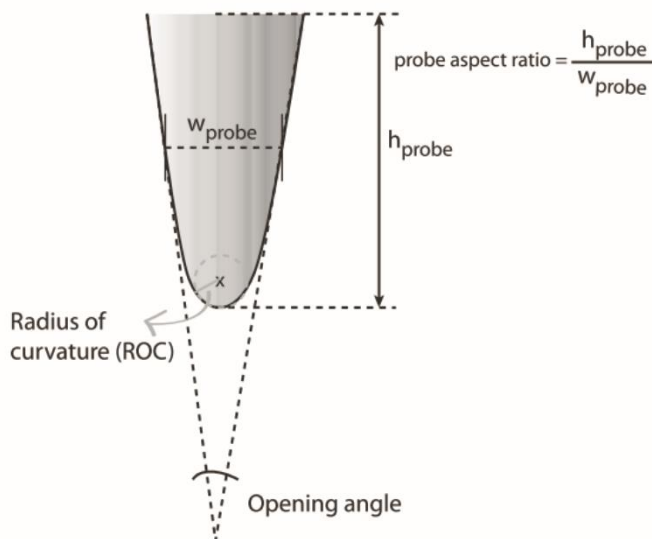


Figure 2.8: The probe is generally characterized by its height, h_{probe} , its width, w_{probe} , its opening angle, and its radius of curvature (ROC). A good probe should have a high aspect ratio, a small opening angle and a small ROC to image the sample’s true topography at the highest resolution [72].

corrugated. Consequently, the tip may interact with different parts of the sample, and the sample may in turn interact with different parts of the tip. All in all, this often results in a not negligible - and probably complex - convolution of the sample features with the tip shape that affects every SPM image [72].”

In general, the probe’s tip influence on the resulting sample topography image must be minimized. To do so, the shape of the tip has to be accurately controlled, and its geometry known, in order to determine the true profile of the sample.

To reach the purpose, the probe should fulfil the following requirements:

- a) **smallness**: the smaller the probe, and, in particular, the probe’s apex, the better. In any case it should be negligibly small compared to the sample features of interest;
- b) **sharpness**: the edges around the apex of the probe should be as perpendicular to the sample surface as possible;
- c) **length**: to avoid the interaction between sample features and the cantilever, the tip should protrude from the cantilever far enough;

d) **durability**: a tip should resist possible wear and damage after continuous scanning.

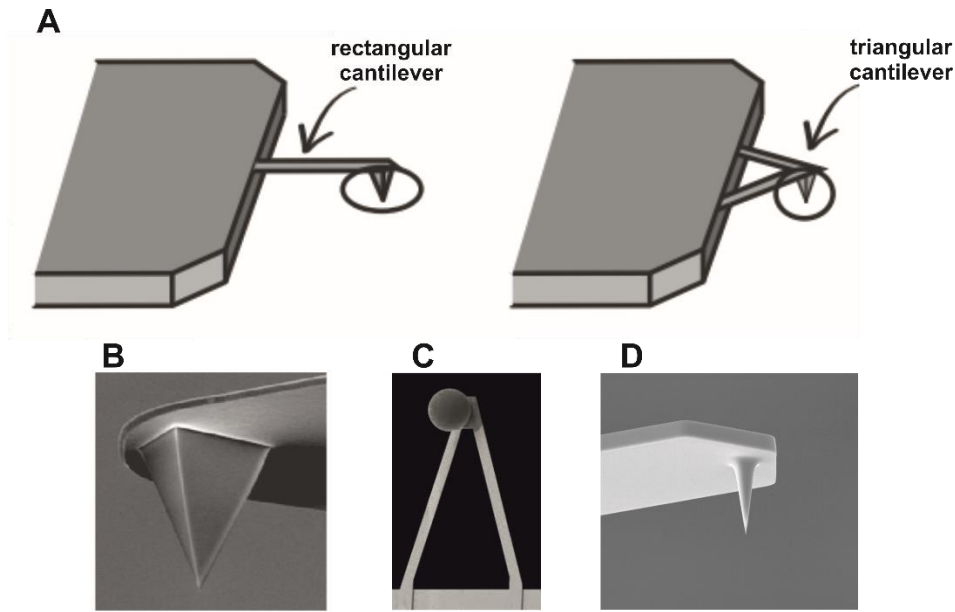


Figure 2.9: A) Rectangular and triangular cantilevers [72]; pyramidal (B), spherical (C) and conical (D) tips.

The AFM probe is integrated to a cantilever at its free end, while the opposite cantilever end is attached to a relatively thick, millimeter-sized slab, the chip. The chip and the cantilever are generally made of the same material, usually doped or undoped silicon or silicon nitride, but other materials such as gallium arsenide or diamond are also employed. The cantilevers are micrometer-sized beam springs that are able to bend vertically and twist laterally, and their shape may be either rectangular or triangular (fig. 2.9, A). Commercial cantilevers are usually 100-200 μm long, 10-50 μm wide, and 500-700 μm thick. Tips may adopt different aspects and geometries, but the most typical are the pyramids (fig. 2.9, B).

The cantilever probe acts as a force transducer (fig. 2.10): it transforms the total interaction force F acting on the tip into a measurable deformation Δx . For small deformations, the cantilever behaves like an ideal spring governed by Hooke's law:

$$F = k \cdot \Delta x$$

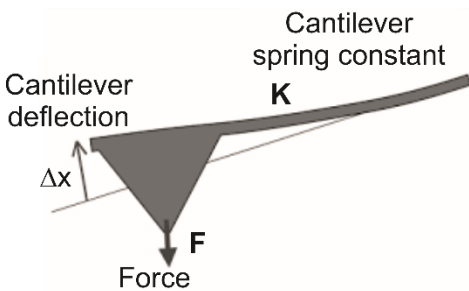


Figure 2.10: Representation of cantilever's force, displacement and spring constant.

where k is the spring constant of the cantilever that depends on cantilever material and geometry: short, thick cantilevers present high k values, while long, thin cantilevers are softer. Nominal k values are generally reported for commercial cantilevers, but, if we are interested in knowing exactly the applied force, it is necessary to calibrate each cantilever before using it. This can be done, for instance, using the so-called thermal noise method [79].

Chapter 3

Materials and Methods

The goal of my PhD project was to study the response of excitable cells after the application of mechanical stress. To do so, I dedicated the last three years to the development and tuning of systems that could permit to perform the application of mechanical stress to cells as well as to quantify their response, for example, in terms of recording their electrical signals. Moreover, I performed elasticity measurements and topographical analysis of different types of cell scaffolds in the context of projects aimed to study *in vitro* models of cancer.

3.1 Cell Stretcher Device

I started my PhD work with the optimization of a stretcher device developed by the research group of the Department of Biophysical and Electronic Engineering of University of Genova. A circular actuator based on a dielectric and transparent elastomer film was used to study cellular mechanotransduction since it allows to apply controlled deformations on adherent cells, and *in situ* simultaneous inspection through fluorescence microscopy and AFM. The device has an external ring where compliant graphite electrodes are deposited on both sides of the film, while cells are seeded and cultured in the central area (fig. 3.1).

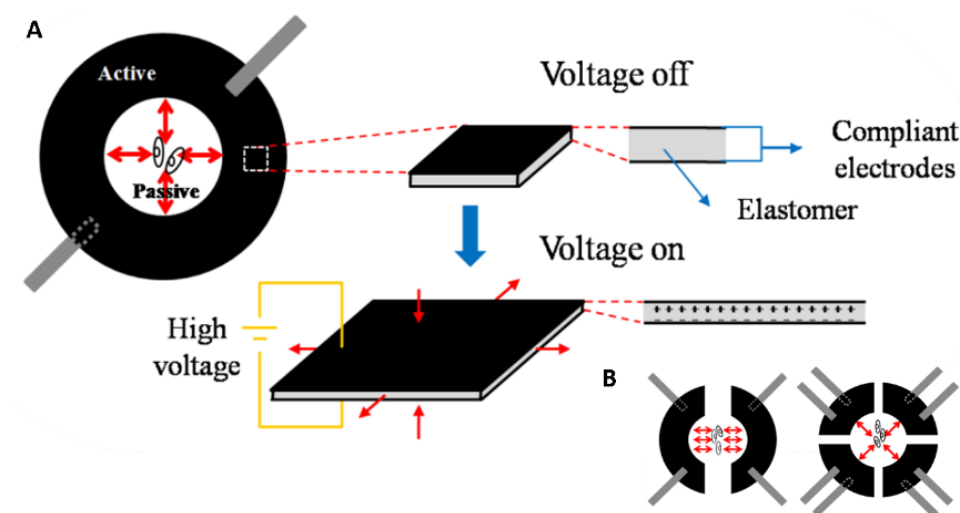


Figure 3.8: A) Illustration of the circular dielectric elastomeric actuator, and the modality of working: we can distinguish the active and the passive area, and the deformation mode when the high voltage is on; B) other types of deformation can be obtained by changing the electrodes layout.

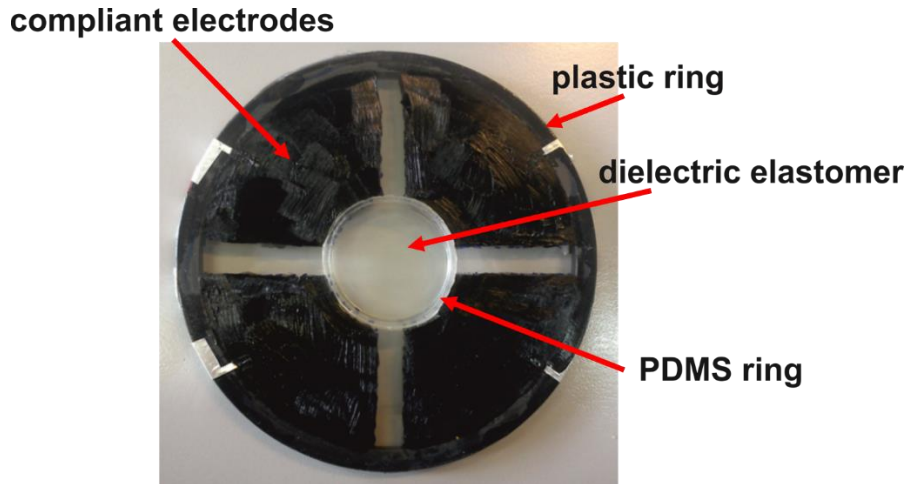


Figure 3.2: The cell stretcher device.

High voltage (up to 4 kV) between the upper and lower electrodes is applied, therefore the elastomer film is compressed in the transverse direction due to electrostatic force and expands in the in-plane direction (fig. 3.1). As a consequence, cells adhering onto the central area of the disk will undergo a symmetric compression. When switching the applied voltage back to zero, the elastomer film will tend to return to the original geometry, thus making the deformation reversible.

More specifically, the cell stretcher device (fig. 3.2) consists of an acrylic-polymer-based (VHB 4910®) from 3M, available as films with predefined thicknesses. The membrane has to be pre-stretched in order to enhancing the electromechanical response of dielectric elastomer actuators as it allows higher actuation strain: reducing the thickness of the film leads to an increase of the electric field. In these devices a circular central zone of the film of 25 mm diameter reaches a pre-stretch deformation of about 300%. The elastomeric membrane is fixed on a circular rigid support made with an acetal resin (polyoxymethylene) of 95 mm for the external diameter, 90 mm for the internal. VHB films are very sticky, so it is not necessary to use glue or similar adhesives to fix it. The excess parts of the film are not cut away but fixed in order to cover all the rigid support. Strips of aluminium paper were used to create the contact points to connect the device to the high voltage source. Aluminium paper of small dimensions was used in order not to stiff the membrane. For every electrodes couple there are two contacts: one for the upper electrode and one for the bottom electrode. It is necessary that the upper and the lower electrodes do not come into contact in order not to create electrical bridges and electrical sparks that can lead the membrane to break.

After positioning of the contacts, the electrodes were painted on both faces of the membrane using the Carbon Conductive Grease 846, M.G (Chemicals-Canada). The circular zone in the centre of the device was left free from carbon: in here the polydimethylsiloxane (PDMS) ring for the cellular culture was fixed (fig. 3.2). The ring was fixed to the device using the same mixture of Sylgard 184 and 527 used to produce the rings. PDMS was left to polymerize in oven for 30 minutes at a temperature of 37° C. Just a minimal amount of PDMS for the ring sticking is needed: exceed may cause a stiffening of the membrane. The temperature is as low as possible because the VHB does not withstand higher temperatures.

3.1.1 Characterization of the Deformation

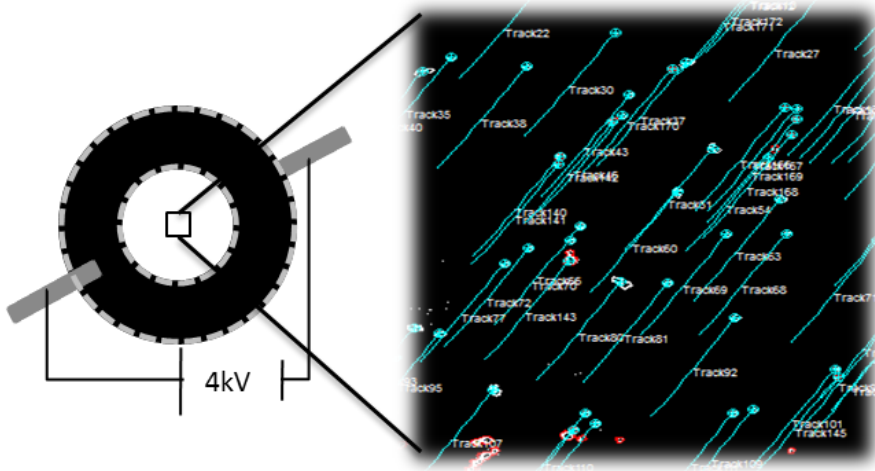


Figure 3.3: The deformation of the substrate was quantified by tracking fluorescent microspheres attached in the passive area during the application of the high voltage and analyzing the distance traveled.

With the purpose of knowing the strain level on the passive zone of the cell stretcher devices during the application of high voltage (4 kV), fluorescent microspheres (Polysciences, inc Warrington, pa cat 17155, ϕ 3 μ m) deposited on the passive zone of the devices were used as markers. A custom-made hollow stage hosting the cell stretcher device was mounted on an inverted

optical microscope (IX70, Olympus, Tokyo, Japan) and connected to the voltage supply set up. Images of the markers in rectangular areas of (1200x1200) μ m² at each voltage were taken with a Hamamatsu CCD camera by using HCLImage Live software. The measurement of deformations of the devices was achieved by tracking the displacement of markers on the membrane's surface using ImageJ – Pro software (fig. 3.3): X and Y marker coordinates were acquired during the application of the different voltages from 0 to 4 kV increasing by steps of 0.2 kV. In order to obtain valid results a minimum of 100 homogeneous tracks had to be calculated using the appropriate filters provided by the tracking software. Using a numerical tool to determine the strain fields, the deformation components were found.

3.1.2 Device Holder and Vibrations Stabilizer Disk

A square Teflon holder was used in order to couple the device with the inverted microscope. The metal plate on the top of the holder allows the system holder-device to be coupled with the AFM (Keysight Technologies, model 5500ILM). The lateral parts of the holder present eight metal strips, four per part, needed to connect the device with the cables that provide the device the high voltage

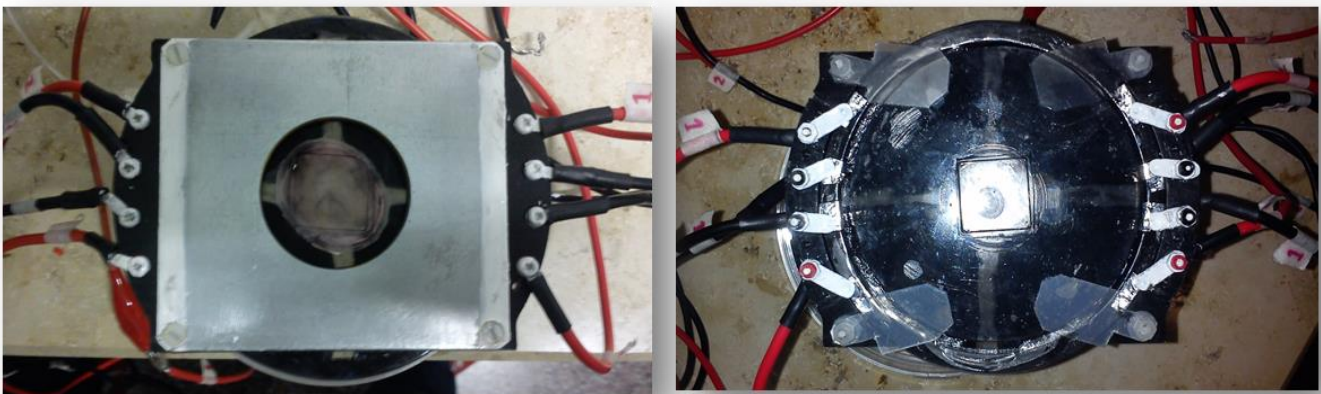


Figure 3.4: Rectangular shaped device holder, frontal (left) and back (right) view. In the frontal view, the metal plate for the coupling with the AFM is also shown.

(fig. 3.4). The metal strips, touching the aluminium ones on the device, create the electrical contacts for the electrodes deformation.

The membrane vibrates when the device is actuated, and these vibrations get worse when the AFM cantilever's tip touch it during the investigation of cells mechanical properties. It's necessary to attenuate this unintentional noise; the stabilizer disk has been designed for this purpose. The vibrations stabilizer consists of a polycarbonate disk that is hold by four plastic transparent tabs fixed in the device holder (fig. 3.4). The hole in the centre of the polycarbonate disk presents a little step needed to house a very thin glass in it, in order to create a well. The well has to be in contact with the passive zone of the device, in which cells are cultured, that is very sticky as it's free of carbon black. To avoid friction between stabilizer and membrane the well has to be filled with a low friction liquid, specifically oil. The contact between the stabilizer and the membrane has to be the minimum possible, or the stabilizer disk will push the membrane on the holder preventing the deformation of the device.

3.1.3 Cell Culture

In order to use the devices for cell stretching applications is necessary to create a cell-friendly environment. First, the membrane and the culture ring are sterilized under hood by filling the culture well (the area inside the PDMS ring, as fig. 3.2 shows) with an ethanol solution (70% v/v), emptying it after 20 minutes and then drying it for 30 minutes under laminar flow to ensure ethanol evaporation. Then, the membrane is washed with water in order to completely remove it. The ethanol should not remain on the membrane for a long time as the VHB membrane takes up the alcohol and swells: the resulting internal stress could break the pre-stretched membrane.

To permit the deposition of the cell on the VHB membrane is necessary to make the membranes biocompatible: the sterilized passive zones are incubated overnight with the adhesion molecules in PBS solution (0.02% gelatin and 100 μ g/ml fibronectin for fibroblast cells), to enhance the adherence of the cells to the membrane. The devices are kept closed with Parafilm to avoid the solution evaporation. Supernatant is removed after 12 hours of incubation and devices are dried under laminar flow during 15 min.

Since I could not get a high enough throughput to achieve statistically significant results, after the first year I dedicated myself to another project, described in the next paragraph.

3.2 AFM-MEA Integrated System

The AFM-MEA integrated system has been developed for the investigation of the behaviour of excitable cells and their mechano-electrical response. The system is composed of an AFM, an optical microscope, a microelectrode array, and custom circuitry. This setup allows optical microscopy, electrical recording and *in situ* mechanical stimulation of single cells. The integration of the different techniques represents a new tool for the investigation of the mechano-electrical coupling of cell networks, such as the well know phenomena of the excitation-contraction-coupling (ECC) and the mechano-electric feedback (MEF), for *in vitro* cardiac muscle models, but also for less established phenomena involving neuronal cells.

The technical starting point of this work was an existing experimental setup that integrates AFM, optical microscopy and MEA electrophysiology measurement on either embryonic or postnatal rat ventricular cardiomyocytes [54]. This setup was designed, fabricated and tested by the group of my PhD supervisor, Prof. Raiteri. In particular, this system was optimized at the hardware composition level, and it was characterized in terms of ability to record consistent electrophysiological signals from neurons in culture. To achieve this purpose, a new custom electronic board was designed and fabricated, to allow the recording of neuronal signals, which has a lower intensity compared to the cardiomyocyte model, hence the previous system could not detect them.

3.2.1 Setup Description

The physical interface between the AFM, the inverted light microscope, and the MEA has been developed in order to fit the commercial AFM used in Genova (model 5500, Keysight Technologies) and includes four different layers (fig. 3.6 and fig. 3.8, E):

- an aluminium plate (fig. 3.8, F) to house the cells cultured onto the microelectrode array. This layer is equipped with two 1.25 W adhesive heating silicon pads and a Pt100 temperature sensor (both from RS Components) as shown in fig. 3.5. These components allow to keep the cells at physiological temperature (37.4°C) during the time of the experiment;

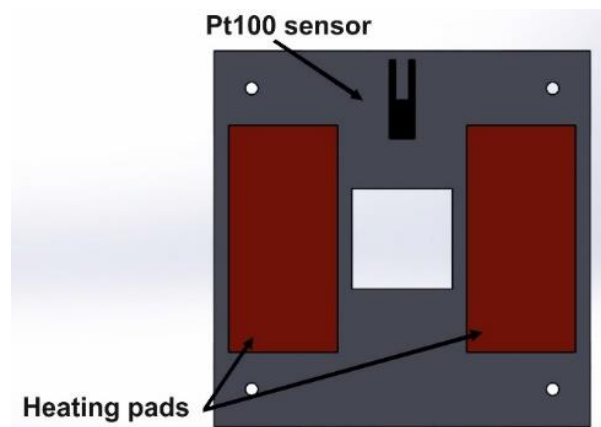


Figure 3.5: Schematization of the temperature sensor (pt100) and the heating pads placed behind the aluminium plate.

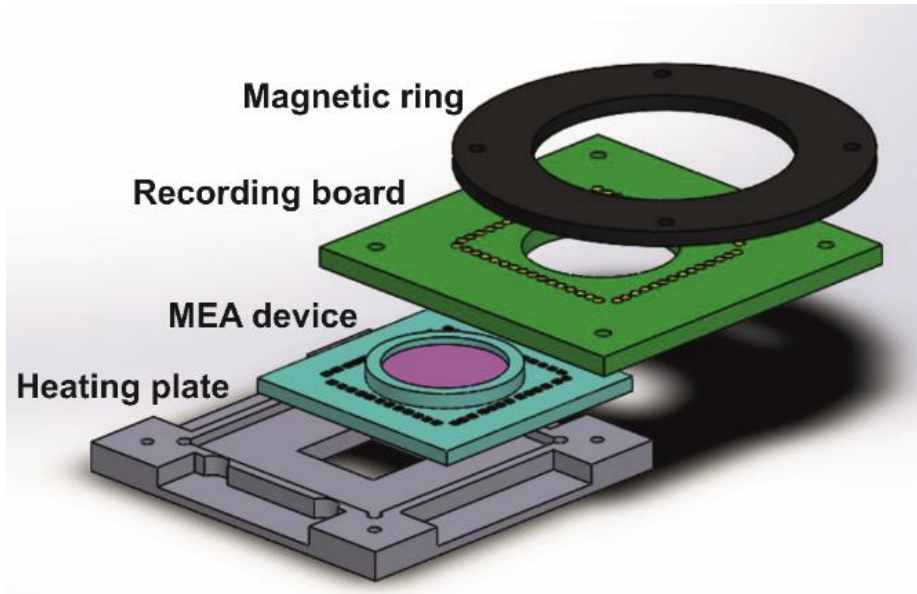


Figure 3.6: The image shows the main elements of the multilayer device that includes a heating plate to keep cells cultured on the electrodes at 37°C, the MEA device, the recording board for the detection of cell signals, and the magnetic ring for the coupling with the AFM stage.

- a pre-amplification board composed by precision JFET amplifiers AD8643 (fig. 3.8, A and B), amplify with a 10x gain the electrical signals recorded by the microelectrodes of the array before the high gain amplification stage. The board is designed to minimize the length of the physical connections. Its main purpose is to decouple the signals from the electronic noise coming from the source;
- a commercial MEA device with 60 electrodes (see the next paragraph);
- a magnetic ring to place firmly all components under the AFM head and still allow lateral movement of the MEA with respect to the AFM tip.

Although, this interface has been developed for a specific AFM model and optical microscope (Olympus IX70), it can be adapted to be used with other combinations of AFM and optical microscope systems, as I did to perform measurements on human cardiomyocytes, as it is explained in more details in paragraph 4.1.3, chapter 4.

Figure 3.7 shows a schematic representation of the acquisition and stimulation system, starting from the pre-amplifier board. The electrodes in the MEA device are connected by spring contacts that match the MEA pads structure. Three flat cables with zif connectors are employed to carry the pre-amplified signals: they were chosen to minimize the cable weight burden, in order to avoid potential instability in the sample stage that is magnetically attached to the AFM head. The signals probed by the interface board require added amplification and filtering in

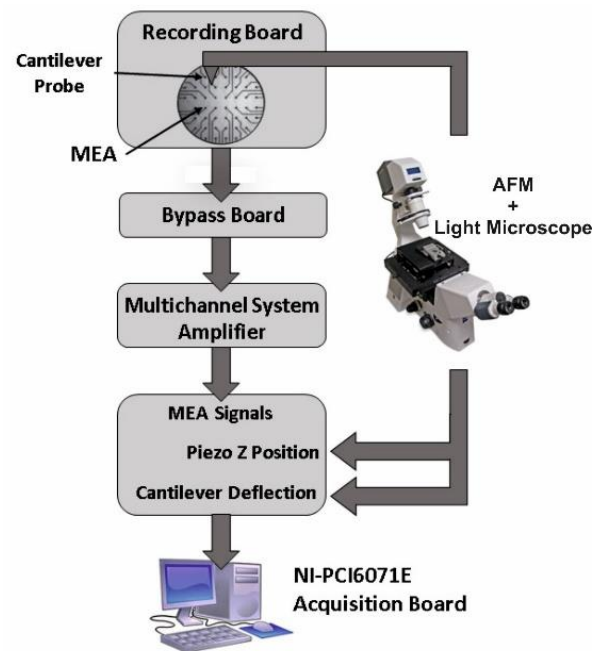


Figure 3.7: Schematization of the AFM-MEA integrated system.

order to be digitalized with significant signal-to-noise ratio. In order to achieve this goal, a differential high gain 64-channel amplifier made by Multichannel System was employed, with a bandpass of 10-3000 Hz and a gain of 1000 V/V (fig. 3.8, C). A bypass board between the pre-amplifier board and the Multichannel amplifier is responsible for adjusting the channels' disposition so that it can fit the pinout of the SCSI connector needed to feed the signals into the high gain amplifier.

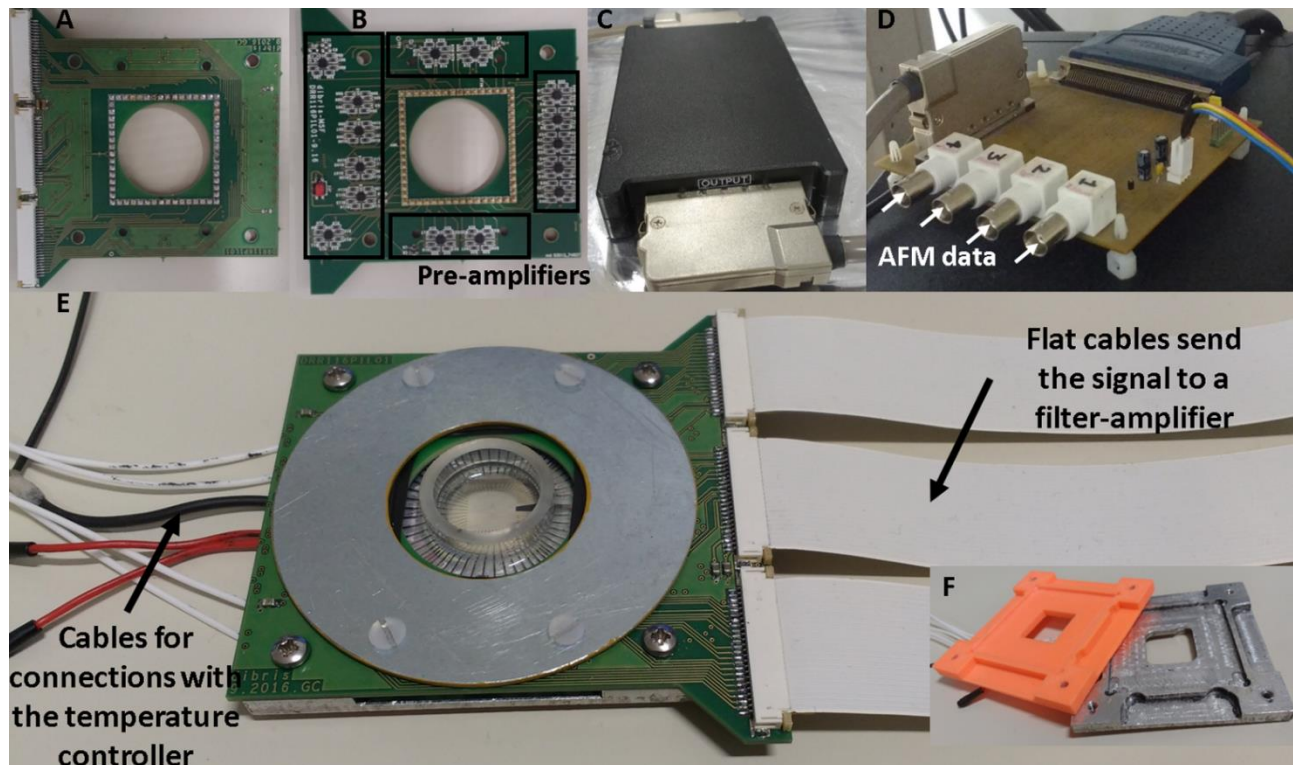


Figure 3.8: The front (A) and the back (B) sides of the recording board, where it is possible to see all the pre-amplifiers connected to all the recording channels; C) filter-amplifier by Multichannel System; D) electronic board employed for collecting MEA signals and data from the AFM; E) the assembled multilayer device represented in fig. 3.6 with all the cables for the connections with the temperature controller, and the filter-amplifier; F) two version of the plate for MEAs allocation: the aluminium one to be heated, and the plastic one for trials where the temperature control was not required.

The AFM data, consisting of the vertical piezo position and the cantilever deflection, are acquired in two ways. The former, called the Z position, is intercepted by the AFM scanner's closed-loop cable with an external bypass PCB. From there, the signal is passed to another board that notch filters it to eliminate 50 Hz noise while amplifying with a 50 V/V gain. The cantilever deflection signal is directly acquired from the AFM breakout box. These signals are then carried by a BNC coaxial cable to the second bypass board, assigned to collect MEA and AFM signals, matching the pinout of the NI-PCI6071E acquisition board (fig. 3.8, D).

3.2.2 MEA and AFM Tools

MEA devices used in this work are commercially available from Multichannel Systems. They are made of a glass slide, measuring 49x49x1mm, onto which electrodes and tracks are fabricated by surface micromachining techniques. Titanium (Ti), or indium tin oxide (ITO), are selectively deposited via plasma enhanced chemical vapor deposition (PECVD) to obtain tracks, electrodes, and

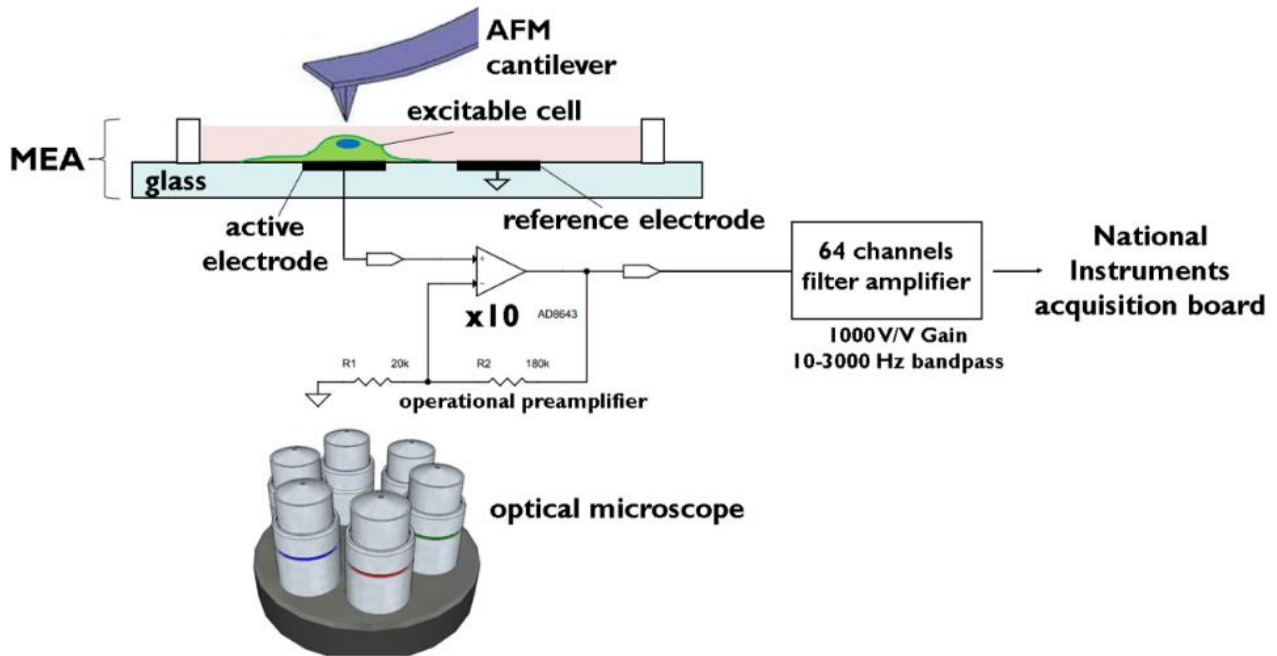


Figure 3.9: Schematization of the AFM-MEA integrated system where it is shown the single cell, plated on one electrode, whose features are investigated by AFM cantilever, the recording circuitry, and the optical microscope

contact pads. A subsequent layer of titanium nitrate (TiN) is deposited in the same fashion only on the electrode area to increase the area in contact with the electrolyte. Such coating increases electrode stability against possible redox reactions, while lowering impedance. To provide insulation on all the device, except for the electrodes area, a layer of transparent silicon nitrate (Si_3N_4) is deposited on top of all the other layers. A large electrode is fabricated outside the array of microelectrode to provide a reference for extracellular field potential stable recording [62]. All the materials are biocompatible, chemically stable in culture medium, and can be easily coated with ECM proteins to promote cell adhesion.

Two types of microelectrode arrays were selected for this study:

- 60HDMEA30/10iR-ITO presents an electrode diameter of $10\mu\text{m}$, and an inter-electrode distance (centre-to-centre) of $30\mu\text{m}$ (fig. 3.10, A) [80];
- 60MEA200/30iR-Ti presents an electrode diameter of $30\mu\text{m}$, and an inter-electrode distance (centre-to-centre) of $200\mu\text{m}$ (fig. 3.10, B) [80];

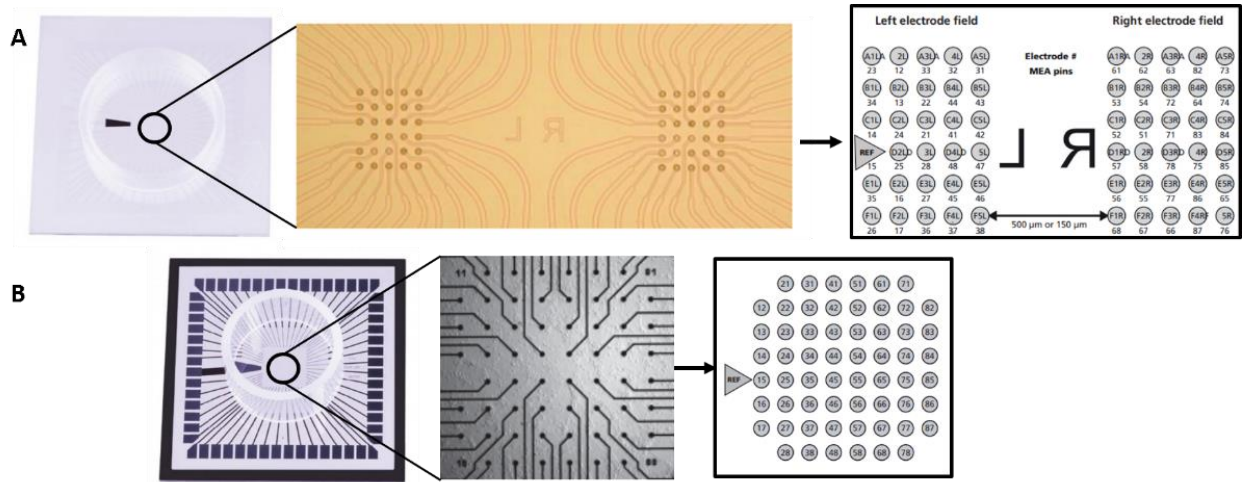


Figure 3.10: A) 60HDEMEA30/10iR-ITO and B) 60MEA200/30iR-Ti layouts.

AFM probes must be accurately selected for each type of experiment. In order to mechanically stimulate cells, a group of tipless cantilevers with different stiffness was selected, in order to apply forces with different intensities depending on the cell type. For example, while using cardiomyocytes that self-assemble as a spheroid, a stiff cantilever was employed, as the size of this spheroid ranges between 100 and 300 μm in diameter, and it is bigger than the cantilever size (table 3.1). In this case, it is necessary to apply a large force to deform the spheroid significantly, using a stiff cantilever. For neuronal networks, on the contrary, a softer cantilever could be used for the stimulation, since neurons are smaller than cardiomyocytes. At the time of this thesis, mechanical stimulation experiments on neurons were not performed. Below, a table is shown that details the probes taken into consideration and their properties.

		Resonance Frequency, kHz			Force Constant, N/m			Length μm	Width μm	Thickness μm
		min	typ	max	min	typ	max			
NCS35, Tipless, AI, MikroMash	Cantilever A	130	205	290	2.7	8.9	24	110 \pm 5	35 \pm 3	2.0 \pm 0.5
	Cantilever B	185	300	430	4.8	16	44	90 \pm 5	35 \pm 3	2.0 \pm 0.5
	Cantilever C	95	150	205	1.7	5.4	14	130 \pm 5	35 \pm 3	2.0 \pm 0.5
All-in-One, Tipless, AI, Budget Sensors	Cantilever A	10	15	20	0.04	0.2	0.7	500 \pm 10	30 \pm 5	2.7 \pm 1
	Cantilever B	50	80	110	0.4	2.7	10	210 \pm 10	30 \pm 5	2.7 \pm 1
	Cantilever C	70	150	230	1	7.4	29	150 \pm 10	30 \pm 5	2.7 \pm 1
	Cantilever D	200	350	500	7	40	160	100 \pm 10	50 \pm 5	2.7 \pm 1

Table 3.1: The table summarizes cantilever models with their main characteristic that were taken into consideration for the purpose of this work.

To characterize the AFM-MEA integrated system, the AFM scanner head with a 9 μm vertical range (5500ILM, Keysight Technologies, USA) from the Bioengineering Laboratory in the Department of Biophysical and Electronic Engineering of University of Genova was employed. While, in order to induce mechanical stimulation on cardiomyocytes, an AFM scanner head with 15 μm vertical range

(NanoWizard 3, JPK, Berlin, Germany) from the Central European Institute of Technology (CEITEC) facility in Brno was used.

3.2.3 Software

PicoView and ExperimentControl commercial software tools were employed to communicate with the AFM systems, the 5500ILM and the NanoWizard3 respectively, and control the experimental parameters. These software tools are always fundamental for preliminary calibration of cantilever sensitivity and spring constant.

A customized MEA signal probing C# software called Hybrainware2 (in collaboration with Jacopo Tessadori from IIT in Genova) was used to acquire neuronal culture electrical activity and to perform electrical noise tests on the AFM-MEA integrated system, while the MC_Rack (Multi Channel Systems, Reutlingen, Germany) software was used to record cell activity with the system provided by Multichannel System. Neuronal activity was recorded using the two systems in order to make a comparison between them, as discussed in the next chapter. The acquisition of signals from cardiomyocytes plated on MEA and from the AFM was performed using a custom LabVIEW (National Instruments, Austin, TX, USA) program (developed by Guido Caluori from CEITEC in Brno). All data were then processed using MATLAB².

3.2.4 Cell Patterning

Cell patterning is the process of positioning cells on a substrate, with defined spatial selection, which in turn keeps the cell growth on the substrate stable. Cellular modifications are dependent on the direction of the mechanical stimulation. As such, it is important to define the pattern of cells placed in the culture.

The patterning technique that I have used in this work is the microcontact printing technique, where a molecular ink is placed upon an elastomeric stamp that resembles the desired geometry that is then transferred to the substrate of interest. The microcontact printing setup is constituted of:

- a vertical square bar screwed in a 2 cm thick steel plate which provides mechanical stability. The bar is equipped with a manual 3-axis micromanipulator onto which different modules can be mounted;
- a second vertical bar, which houses a sliding, adjustable optical system (magnification range 4-20x) and a small CMOS camera for image acquisition (uEye UI1540C);
- a precision scale to monitor applied forces during protein printing;
- a LED light panel, fixed to the scale, which provides intense illumination (adjustable through a dimmer) from the bottom of transparent samples.

The following table shows the patterning procedure employed after some optimization. Protocols for the three main steps: PDMS stamp fabrication, adhesion factor printing, and cell plating, are briefly described.

² For neuron spikes detection SPYCODE 4.0 [81] was employed.

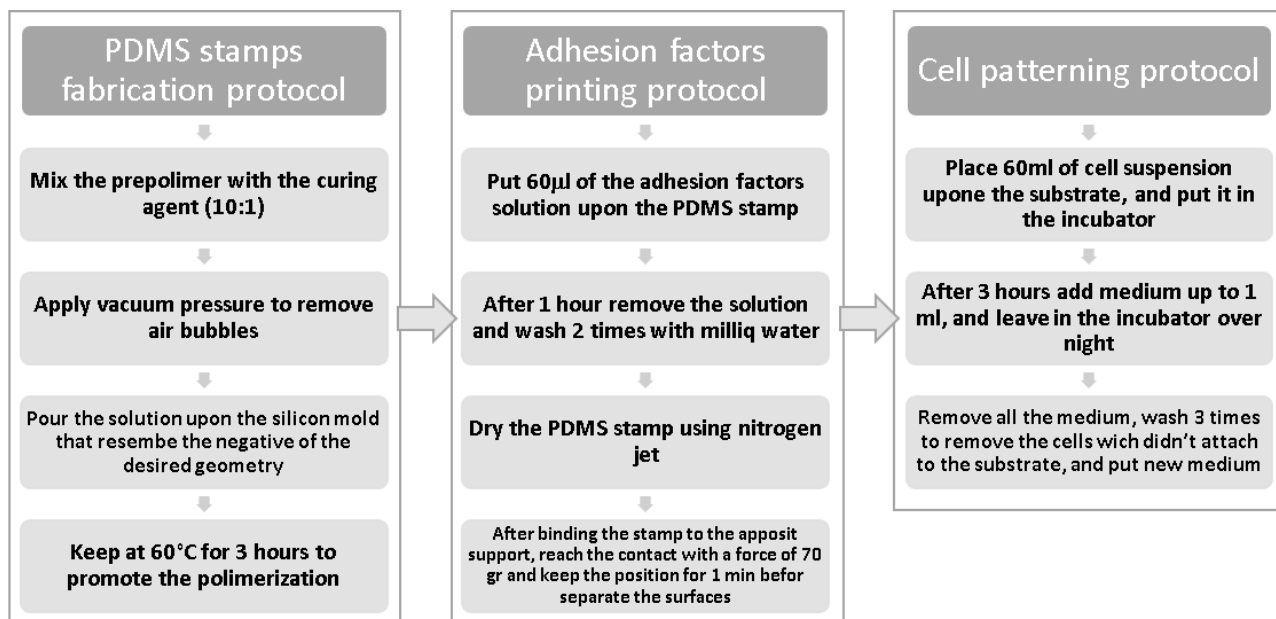


Table 3.2: A summary of the processes of PDMS stamps fabrication, adhesion factors printing and cell plating.

The major improvement I made during my work over protocols already in use in the lab concerns the sterility conditions during the deposition of the adhesion factors: we used to pattern the proteins on the substrate outside the biological hood, and then sterilize with ethanol before placing the cells on this substrate. While performing fluorescence trials I found that ethanol may have a negative effect on the protein structure, and I have hypothesized the possibility that ethanol could compromise cells attachment. Thus, the microcontact printing setup was modified so that the pattern may be performed under in a sterile environment (laminar flow hood, fig. 3.11) to avoid the use of substances like ethanol to sterilize the substrate afterward.



Figure 3.11: Microcontact printing setup inside the biological hood.

3.2.5 Cell Culture

3.2.5.1 Microelectrode Array Cleaning and Coating

Before cell plating, MEAs are cleaned using a 0.1% w/v solution of Tergazyme detergent (Alconox, White Plains, NY, US) in MilliQ water for at least 4 hours. The culture well (the area bounded by the plastic ring) is then washed with MilliQ water to remove the excess agent. The preparation of the device is then moved to a UV-sterilized clean box. Each MEA is placed in 100 mm sterile Petri dish (TPP, Trasadingen, Switzerland), and the MEA culture well is sterilized by filling it with 70% ethanol solution. After 30 min, the sterilizing solution is removed, the culture well on MEA is rinsed twice with sterile water and let dry. The sensing area (the electrode array area) is then coated with adhesion molecules to promote cell adhesion. In particular, for neurons, a mixture of 50 μ l of poly-D-lysine and laminin, 1:1 ratio, is used, while, for cardiomyocytes, a mixture of 50 μ l of laminin and fibronectin, 1:1 ratio, is employed. The MEAs are put in a cell incubator at 37°C, 5% CO₂, overnight. They are then rinsed twice with sterile water to remove any excess of adhesion factor from the surface.

3.2.5.2 Neuronal Network Preparation

Murine tissue was obtained through the removal of 18-day embryos (E18) by caesarean section. The experimental protocol was approved by the European Animal Care Legislation (2010/63/EU), by the Italian Ministry of Health in accordance with the D.L. 116/1992 and by the guidelines of the University of Genova (Prot. N. 24982, October 2013). Cortices were removed from murine embryos and their tissue were at first enzymatically dissociated in 0.125% of Trypsin/Hank's solution containing 0.05% DNase (Sigma Aldrich) for 18-20 min at 37°C and then mechanically dissociated with a fire-polished Pasteur pipette.

3.2.5.3 Neuron Plating on MEA Chip

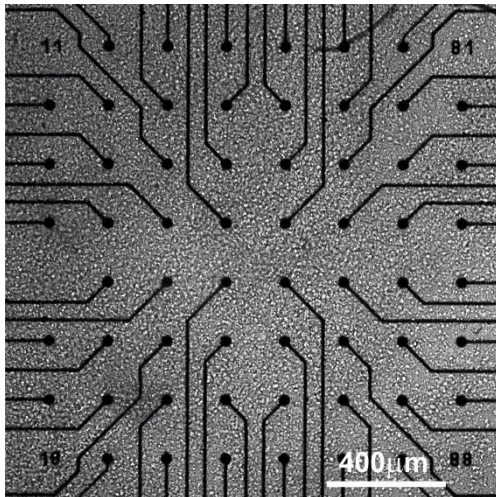


Figure 3.12: Cortical neurons plated on a MEA chip.

Cells are plated on the MEA chips (fig. 3.12) at a density of about 1000 cells/mm² in a solution containing Neurobasal™ Medium with 1% Glutamax, 2% B-27 supplemented, 1% penicillin–streptomycin (all from Invitrogen Life Technologies). MEAs are then incubated in a humidified 5% CO₂ atmosphere at 37 °C and half-volume medium is replaced every week. Measurements of electrical activity were performed after 21 Days In Vitro (DIV).

3.2.5.4 Neuron Patterning

As shown by a recent study [82], the network activity of an organized cellular culture and its overall development are not significantly altered when compared to random control cultures. It has been shown that an imposed grid topology that matches the position of the electrodes can reinforce the connectivity in the directions of interest. For these reasons, an ulterior aim of this project is to realize a strong and reproducible cell patterning protocol on MEAs to spatially control neuronal network growth and microelectrode arrays in order to realize a long-term, non-invasive neuro-electronic interface. To achieve such a goal, two strategies were employed: the first one is based on microcontact printing technique (described in paragraph 3.2.4), which consists in transferring a pattern of adhesion molecules onto the MEA substrate through PDMS stamps, made with the Replica Molding technique obtained through the use of an SU-8 master on a silicon wafer as a mold. In particular, the adhesion

molecules pattern consists of stripes that are 40 μm wide 1,2 mm long and spaced 200 μm , and it matches with the 60MEA200/30iR-Ti electrodes layout.

The second approach is based on the use of PDMS masks to confine cell seeding and growth.

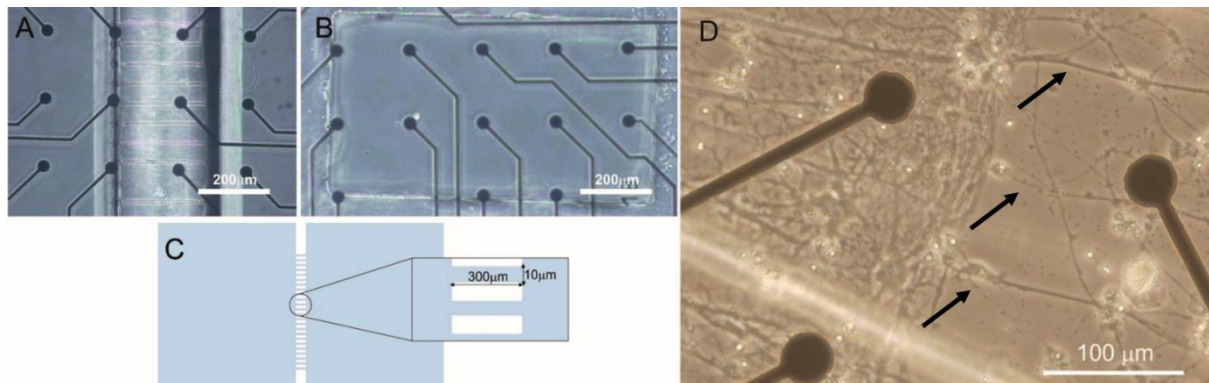


Figure 3.13: A) A PDMS mask consisting of two compartments and the microchannels on the MEA surface; B) A PDMS mask consisting of one compartment on MEA surface; C) Illustration of the two compartments geometry; D) Neuronal pattern on MEA obtained using the PDMS mask with the two compartments and the microchannels: it is possible to distinguish lines of axons (indicated by the black arrows) grown inside the microchannels at 21 DIV.

Two different geometries for the masks were considered, the first one (fig. 3.13, A and C) consisting of two compartments (600 μm x 1,5 mm) interconnected by microchannels (400 μm x 30 μm), and the second one (fig. 3.13, B) consisting of four compartments (500 μm x 800 μm) that are not interconnected. No significant differences were evidenced in terms of cell morphology or viability between the two geometries.

Both methods need to be optimized, and in particular the microcontact printing procedure, in order to obtain a stable patterned culture on MEAs. Fig. 3.13, D shows a neuronal pattern on MEA obtained using the PDMS mask with the two compartments and the microchannels where it is possible to distinguish lines of axons grown inside the microchannels, while results of neuronal patterns obtained with microcontact printing are shown and discussed in the next chapter.

3.2.5.5 hPSC Culture and Cardiac Differentiation

Pluripotent cells were firstly thawed and seeded on mitotically-inactivated mouse embryonic fibroblasts (feeder cells). The hPSC colonies are cultivated in DMEM-F12 (Thermofisher, Waltham, MA, USA) supplemented with 15% KnockOut fetal bovine serum (FBS, Life Technologies, Carlsbad, CA, USA), 1% L-glutamine (Thermofisher), 0.5% penicillin/streptomycin (Thermofisher), 1% 2-mercaptoethanol (Thermofisher), 1% non-essential amino acids (Life Technologies), and 10 ng ml⁻¹ human fibroblast growth factor 2 (hFGF2, Peptrotech, London, UK). The medium is changed daily, and colonies are propagated for at least 5 passages, by manual fractioning. Cardiac differentiation is started by embryonic body (EB) formation: briefly, compact, round colonies are manually cut and scratched from the culture surface. The cell leaflets are then transferred in hypoxic incubation atmospheres (5% O₂) and underwent a sequential cytokine modulation in KnockOut DMEM (Life Technologies), supplemented with 10% FBS, 1% L-glutamine, 1% PS, 1% 2-mercaptoethanol, 1% non-essential amino acids (further referred simply as MEF medium), with 10 μg ml⁻¹ BMP4 (R&D Systems, Minnesota, MN, USA) and 10 μg ml⁻¹ ascorbic acid (Sigma Aldrich). Beating cardiac clusters are visible from day 14 and are transferred into normoxic atmospheres. After day 22, they are kept in the MEF medium with ascorbic acid.

3.2.5.6 Beating Cardiac Clusters Plating on MEA Chips

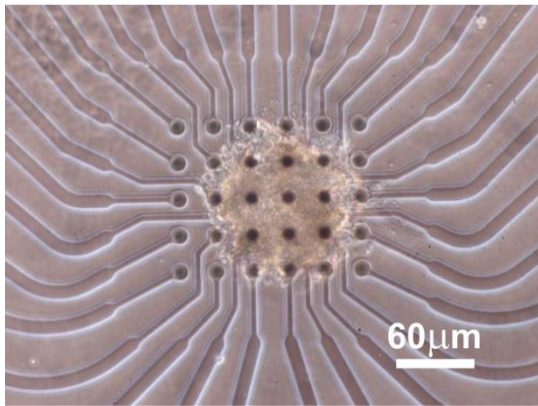


Figure 3.14: A beating cardiac cluster plated on a high density MEA chip.

Suspended beating cardiac clusters (BCCs) are collected and plated on MEA sensing area that was previously filled with 500 μ l of the MEF medium. Samples are manually placed on top of electrode array, then 200 μ l of the medium is removed to encourage cells attachment on the electrodes surface. After that, samples are put in standard cell incubator and kept in this 1 hour (each Petri dish containing a MEA was enclosed using parafilm to avoid the medium evaporation). Then medium is gently added up to 1 ml. After 2 days *in vitro* to ensure appropriate adhesion, spreading and formation of cell-electrode contacts, the BCC can be measured. Fig. 3.14 shows a typical BCC properly placed on MEA, before beginning the experiments.

3.3 Mechanical Characterization of a 3D Alginate-Matrigel Hydrogel as Scaffold for Human Breast Cancer Cells

I performed AFM measurements for the mechanical characterization of three types of scaffold for the study of the breast cancer *in vitro*. The purpose of this study was the development of a 3D material to be used as substrate for breast cancer cell culture. A composite gel constituted by different concentrations of alginate (A) and matrigel (M) was developed to obtain a structurally stable-in-time and biologically active substrate.

Human aggressive breast cancer cells MDA-MB-231 were cultured within the gels, and cells were morphologically characterized while considering the relation between cell morphology and malignancy. Moreover, their invasiveness was studied through a bioreactor-based invasion assay. The type of gel composed by 50% alginate and 50% matrigel emerged as superior compared to the others thanks to a series of significant results. In fact, cells cultured in this gel exhibited peculiar cytoskeleton shapes and nuclear fragmentation (characteristic of their malignancy), expressed the formation of the so-called invadopodia, actin-based protrusion of the plasma membrane associated with degradation of the extracellular matrix in cancer invasiveness and metastasis, and finally they were able to migrate through the gels and attach to an engineered membrane, mimicking the vascular walls hosted within bioreactor. The results are promising and make this 3D scaffold a new *in vitro* model of the very precursor steps of metastasis.

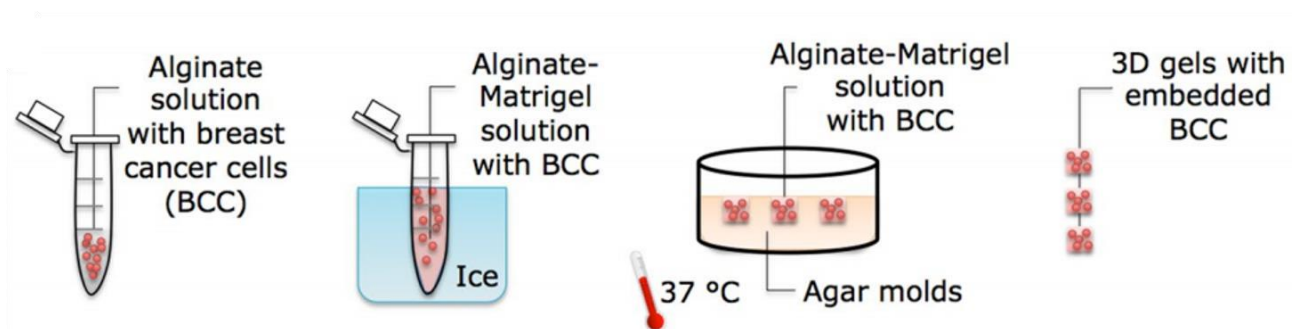


Figure 3.15: Schematic description of the protocol used to produce 3D cell-laden alginate-matrigel composite gels: breast cancer cells MDA-MB-231 are seeded first in liquid alginate and then matrigel is added working on ice. The cell-laden solution is transferred into Agar molds enriched with CaCl_2 ions at 37 °C for to allow gelation. Then, 3D gels are removed by molds and transferred into plates with culture media.

Stiffness measurements of hydrogels with a different alginate-to-matrigel concentration (100% A, 75%:25% A:M, 50%:50% A:M) were performed using a commercial AFM, equipped with a scanner that has a vertical range of 9 μm (Keysight Technologies, model 5500ILM). To compensate for piezo nonlinearity, creep and hysteresis, the scanner continued to operate in a closed loop during all the experimental session. A rectangular micro-cantilever (CSG 11 type, NT-MDT, Russia) with a conical tip was employed, and its spring constant was calculated by monitoring the cantilever oscillation in air due to thermal noise, following the procedure described by Hutter and Bechhoefer [79]. Standard force curves were recorded to evaluate hydrogel stiffness. The section of the curve produced after the contact between the cantilever and the sample was then considered for further analysis. The applied load for cantilever deflections was calculated by first converting the output voltage from the AFM four-segment photodetector into nanometres of deflection, and then by multiplying the deflection by the cantilever spring constant. The conversion factor was calculated by taking several force curves on a hard glass substrate each time the laser spot on the cantilever had to be adjusted, as well as by considering the reciprocal of the average slope of the constant compliance region of the curves. When using sharp conical tips, the load versus indentation curve was evaluated to extract the elastic modulus of the sample using the model proposed by Oliver and Pharr [83]. All measurements were performed at a constant approaching/retracting speed of 4 $\mu\text{m/s}$.

Hydrogels were glued onto a Petri dish using a minimum amount of fast cyanoacrylate glue, and, during measurement, samples were kept in a buffer containing 5 mM CaCl_2 . Force curves were recorded over a square grid (5 x 5 μm), in order to consider intra-sample heterogeneity. For all the samples, three maps of 16 x 16 curves were collected onto three regions randomly selected over the samples surface. A custom-built software was used for processing the single force curves in order to detect the vertical displacement corresponding to the AFM probe-gel surface contact. Data were expressed as mean values \pm standard deviation. Statistical analysis was performed with Origin 8.0 (OriginLab Corporation, Northampton, MA) using Kruskal-Wallis test. Figures were edited with Corel Draw 2017 (Corel Corporation, Ottawa, Canada). All AFM measurements reported in this paper were taken with the same cantilever and the same experimental conditions. For this reason, the observed relative changes in stiffness among the three samples are not significantly affected by uncertainties due to, for example, the tip geometry or the hydrogel Poisson's ratio (regarding the Poisson's ratio of all tested hydrogels, we assumed a constant value of $\nu=0.5$, corresponding to an incompressible, rubber-like material). On the contrary, the calculated absolute values could be affected by the abovementioned uncertainties.

3.4 Characterization of the Topographical Features of Graphene-Oxide Functionalized Substrates to Study Cell Adhesion

I was involved in another project that has as its main focus the study of the topographical features of graphene-oxide functionalized substrates, where I performed elasticity measurements and topographical images of such substrates, using the same AFM described in the previous paragraph.

Graphene-derived materials, such as graphene oxide (GO), have been widely explored for biomedical and biological applications, including cancer research. Most of the *in vitro* studies are carried out by employing GO sheets dispersed in solution or organized in a planar film as cell substrates for the evaluation of the effects of GO on cancer cell activity. So far, the incorporation of GO within biomimetic substrates that mimic the tumour environment has not yet been fully investigated. The work presented in this paragraph evaluated the interactions of three different cell lines, the human breast cancer cells (MDA-MB-231), a cancer cell line from human osteosarcoma (HOS) and healthy

murine fibroblasts (3T3), with alginate (Alg)/GO hydrogel-based substrates. It was observed that GO addition selectively inhibits malignant breast cancer cells adhesion, efficiency, and spreading area, while promotes HOS and 3T3 adhesive processes. The same results were not obtained when cells were cultured on Alg films with GO nanosheets dispersed only in the medium, without embedment into the Alg. This outcome suggests that the cancer (MDA-MB-231 and HOS) and healthy (3T3) cell adhesion efficacy is induced by the topographical cues provided by the GO-based substrate: these, in turn, support cell activities mimicking the physical features of the tissue of origin.

All AFM elasticity measurements were performed in triplicate, using the same rectangular micro-cantilever (CSG 11 type, NT-MDT, Russia). Its spring constant (k) was calculated following the procedure described in the previous paragraph. AFM imaging was performed in contact mode at the speed of 0.5 line/sec. Samples were kept in a buffer containing 5 mM CaCl₂ during all measurements. Hydrogel stiffness was evaluated by nano-indentation measurements, following the procedure described in the previous paragraph, while image processing and roughness analysis were performed using Gwyddion software (Department of Nanometrology, Czech Metrology Institute). All data are expressed as mean value \pm standard deviation.

3.5 Effects of Different Probes on Elasticity Measurements

Atomic force microscope has found applications in biology to measure features of cells, such as cellular elasticity. AFM indentation can be used to mechanically stimulate cells and quantitatively characterize their elastic properties, providing critical information for understanding their mechanobiological behaviour. Nano-mechanics has become a popular research area, with tools such as AFM often employed to measure bulk cellular rheological properties, typically Young (elastic), or shear modulus. By altering tip geometry or chemistry, a multitude of both local and whole-cell studies can be performed on living cells in their native environments [84]. Nanoindentation can be applied using different sizes for the indenter, opening the possibility to investigate the structure from the whole tissue to the single components. During this third year of PhD, I started performing nanoindentation measurements on soft substrates using the AFM, and, in particular, testing the effect of the tip size on the measured parameters. Measurements were performed employing three spherical tips with different radii on PDMS (3% wt) substrate, which I considered homogeneous (at the probed length scale) and isotropic.

The ratio between the maximum contact radius (a) and the tip radius (R) (fig. 3.17) was kept constant, to create similar deformation conditions among the different measurements.

In particular, this ratio, that we can call ε :

$$\varepsilon = \frac{a}{R}$$

has to be the same for all the spherical tips.

We can obtain the indentation value h starting from the contact radius equation, calculated considering the triangle constituted by R , $R - h$ and a as edges, and applying the Pitagora theorem:

$$a = \sqrt{R^2 - (R - h)^2}.$$

Considering $a = \varepsilon R$ we will obtain:

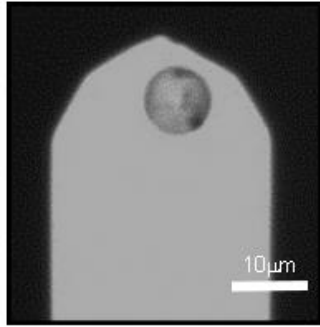


Figure 3.16: Optical image of a cantilever with a spherical tip glued on it.

$$\varepsilon R = \sqrt{R^2 - (R - h)^2};$$

and, solving the equation, we will obtain:

$$h = R - R\sqrt{1 - \varepsilon^2}.$$

Keeping ε value constant for all the measurements with spherical tip, we will obtain the h value, which will be different for each tip, so, a different indentation has to be taken in account while performing force maps.

The aim of this work is to verify that it was possible to extract the same value for the Young modulus of the homogeneous material when probed at different scale lengths. This result could be applied to cells, which are neither homogeneous nor isotropic, in order to probe the mechanical properties of their internal structures and components. To do so, it is important to choose the appropriate tip size and indentation depth.

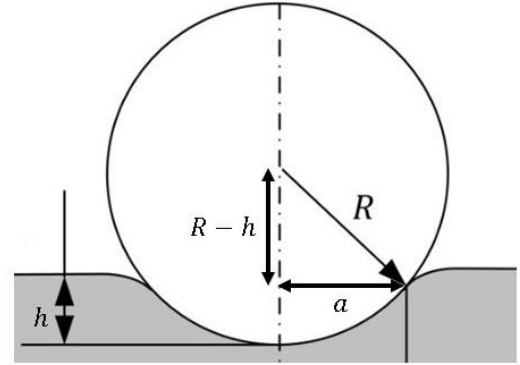


Figure 3.17: The image shows a spherical tip indenting a substrate, where R is the tip radius, a is the contact radius and h is the indentation.

TIP	RADIUS R [nm]	SPRING CONSTANT [N/m]	INDENTATION h [nm]
Spherical 1	1200	0.45	240
Spherical 2	5000	4.7	1000
Spherical 3	10000	8.45	2000

Table 3.3: The table shows the values of radius spring constant of the spherical tips employed, and the values of indentations reached for the purpose of this study.

Cantilevers with different spherical tips were obtained gluing microspheres to tipless cantilevers (fig 3.16), and nanoindentation measurements were performed in the same way as explained in paragraph 3.3 but taking into account different indentation depths. Table 3.3 shows then characteristics of the three spherical tip employed in this study.

Chapter 4

Results and Discussion

In this chapter I present and discuss the results I obtained by working on the cell stretcher device, the implementation of the AFM-MEA integrated system, the cell patterning, and the topographical and mechanical characterization of 3D and 2D hydrogel-based cell scaffolds. In addition, preliminary results regarding the effect of indenter size on AFM based nanoindentation measurements are also described.

4.1 Optimization of the Cell Stretcher Device System

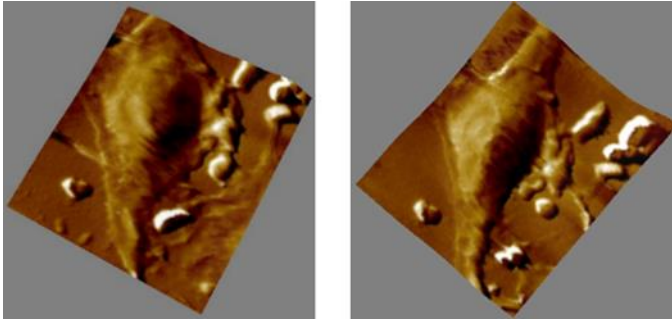


Figure 4.1: AFM images that show the topography of the same fibroblast before (on the left) and after the deformation of the substrate.

The cell stretcher device was optimized in terms of reducing membrane's vibration during the measurement with the AFM. This was achieved by applying glycerol between the device and the rigid stabilizer support. This allowed to take topography images of living cells before and after a deformation cycle (fig. 4.1). As we can observe in figure 4.1, the cell remodels its morphology after the application of unidirectional stress.

Other optimizations include the employing of a bigger support ring (see paragraph 3.1, chapter 3) for the polymeric membrane to reach a higher deformation of the substrate. Figure 4.3 shows the results of the deformation field of two different types of devices with different sizes of support rings. The rings had a diameter of 65 mm and 95 mm respectively, while the same electrode configuration allowed a biaxial deformation (fig. 4.2). The deformation field is composed by the gradient of the components of the Green Lagrange strain tensor, E_{11} and E_{22} .

The biaxial device actuated until 4 kV in two opposite electrodes couple acts as a uniaxial device: only one of the two strain components is significant. Considering the direction of the higher deformation, the maximum strain reached ranged from 8.2-12.86% for the bigger device, compared to one reached with the smaller stretcher which ranged between 1.46-2.08%.

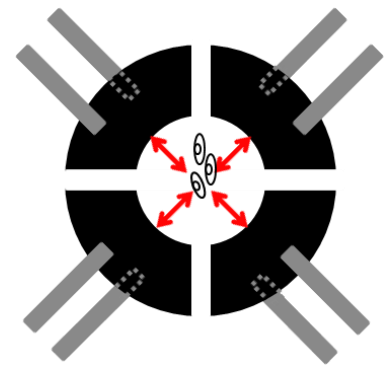


Figure 4.2: Biaxial cell stretcher device (frontal view): four couples of compliant electrodes (located in both the faces of the membrane) allow, under the application of high voltage, the deformation of the device passive zone in two perpendicular directions in-plane.

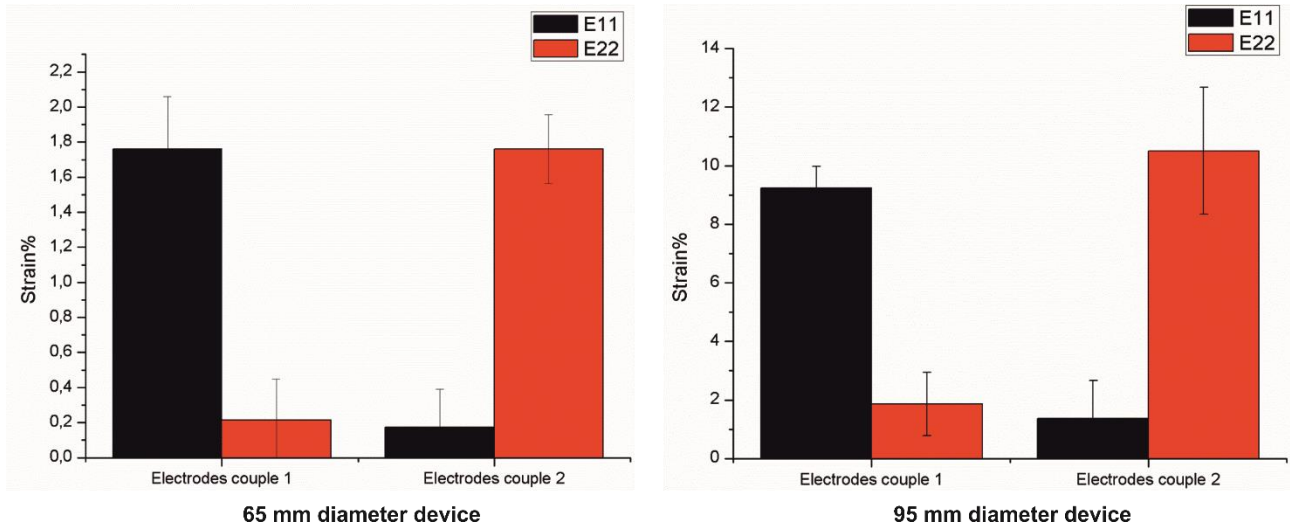


Figure 4.3: Mean percentage strain in absolute value for three biaxial devices of 65 mm (on the left) and 95 mm (on the right) diameter, measured with the stabilizer support.

The major limitations of this device are:

- the difficulty and the time needed to assemble each device manually and to mount it on the AFM sample stage;
- the vibrations of the elastomeric membrane which limits the resolution achievable by AFM measurement;
- the membrane fragility and its sensitivity to the humidity of the incubator environment: this resulted in many devices already loaded with cells which broke while being in the incubator.

4.2 AFM-MEA Integrated System

Results presented in this paragraph refer to the characterization of the AFM-MEA integrated system and to the experiments performed on cardiomyocytes from human pluripotent stem cells (hPSC-CMs). In particular, the new custom pre-amplifier board was tested with cortical neurons, to prove the capability of this system to record also low-amplitude electrical signals, lower than those from cardiac myocytes. Unfortunately, I could focus my work on the system characterization, and significant data related to mechanical stimulation on neurons were not recorded so far because of different problems, related to the neuronal primary cultures preparation, we had in the lab in the last year. On the other hand, some preliminary results were obtained from measurements performed on hPSC-CMs with the aim of validating the use of these cells as models of mechanically-induced arrhythmia, as explained in the following paragraphs.

4.2.1 Characterization of the System with Neurons

In order to record the spontaneous electrical activity of cortical neurons, different sources of electrical noise in the hardware had to be identified and fixed. In particular, the metallic parts of the system were properly grounded, including the cantilever retaining spring in contact with the scanner nose holder.

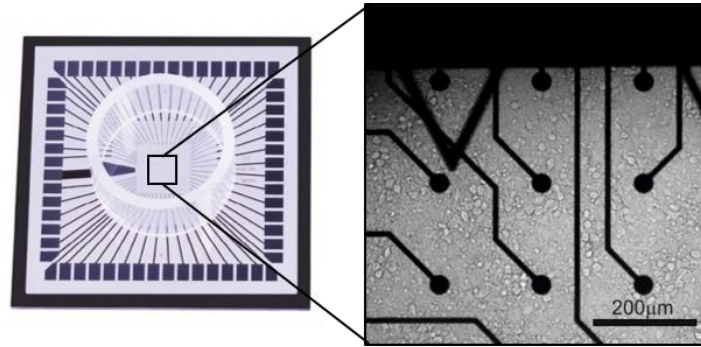


Figure 4.4: On the left, a MEA device, and, on the right, an optical image of the active area where it is possible to identify the electrodes, the neurons and a triangular cantilever.

In order to get reproducible recordings, I had to improve:

- 1) the electrical coupling between the contact pads in the MEA device and the spring contacts of the pre-amplifier board. This was achieved by inserting a plastic spacer between the heating plate and the MEA device, to elevate it and push it harder against the spring contacts (fig. 4.5).
- 2) the mechanical coupling between the AFM tip and the MEA surface. This was achieved using a thinner magnetic ring so as to reduce the total burden.

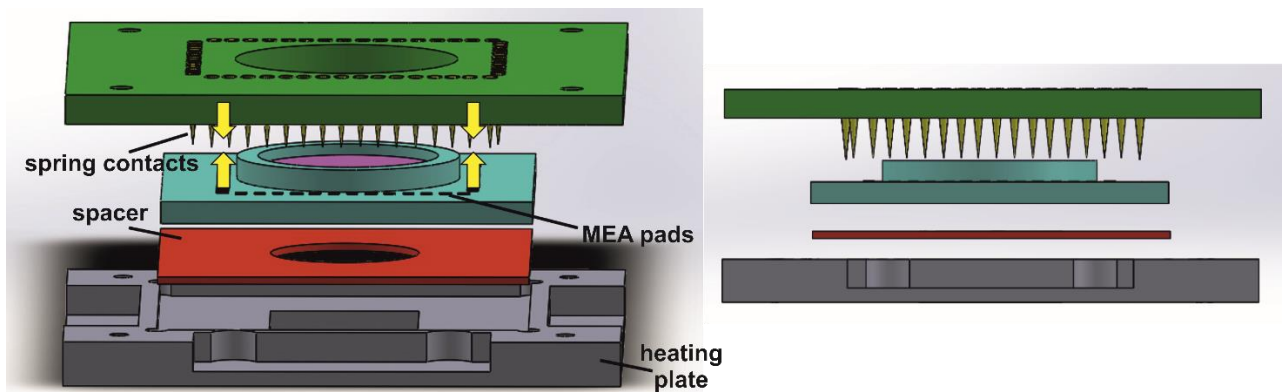


Figure 4.5: Illustration of the system composed by the heating plate, the spacer, the MEA device and the recording board.

After some hardware debugging and improvements, I succeeded in recording the electrical activity of neuronal cultures. Cortical neurons from the same preparation plated on three different MEA devices were tested at 21 DIV. In order to simulate the experimental condition during the mechanical stimulations, measurements were done with the AFM tip in contact with the neurons. The electrophysiological recording obtained with the AFM-MEA integrated setup was compared to the one obtained with a commercial MEA recording system (MEA2100-60, Multichannel System, Germany) as a reference, in order to compare the signal-to-noise ratios and the resulting neuronal network activities with the two systems.

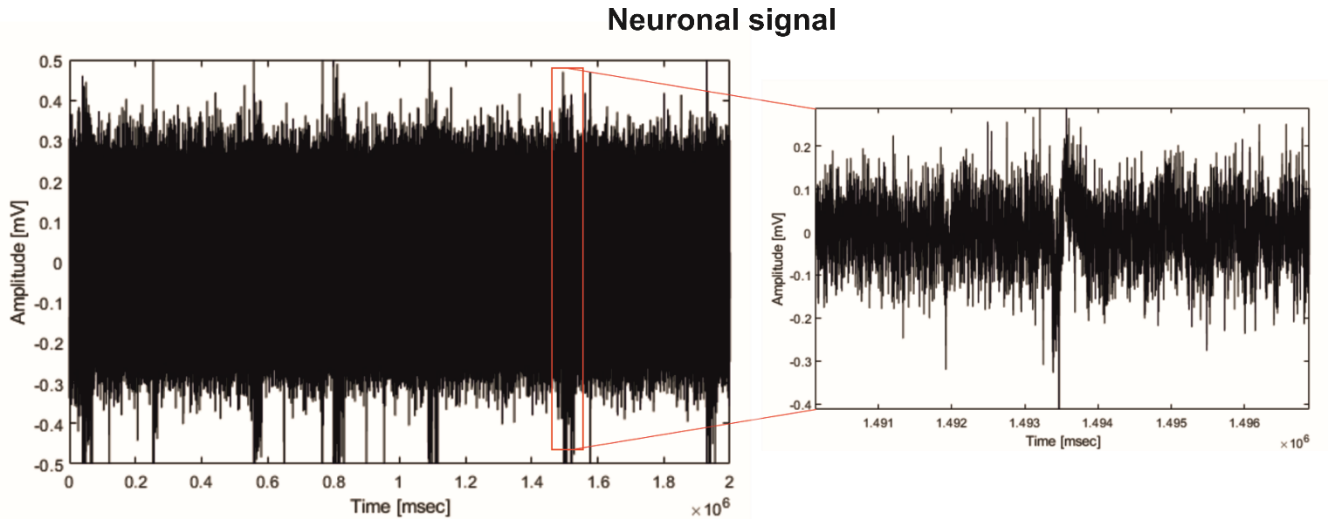


Figure 4.6: Neuronal extracellular signal recorded using the custom pre-amplifier board.

Data analysis was performed using SPYCODE software [81]. By comparing the mean signal-to-noise ratio (SNR) values obtained for each recording channel of the integrated system with those obtained with the commercial reference MEA system, it can be observed that, on average, the SNR is 32% lower in the integrated system using the custom-built pre-amplifier.

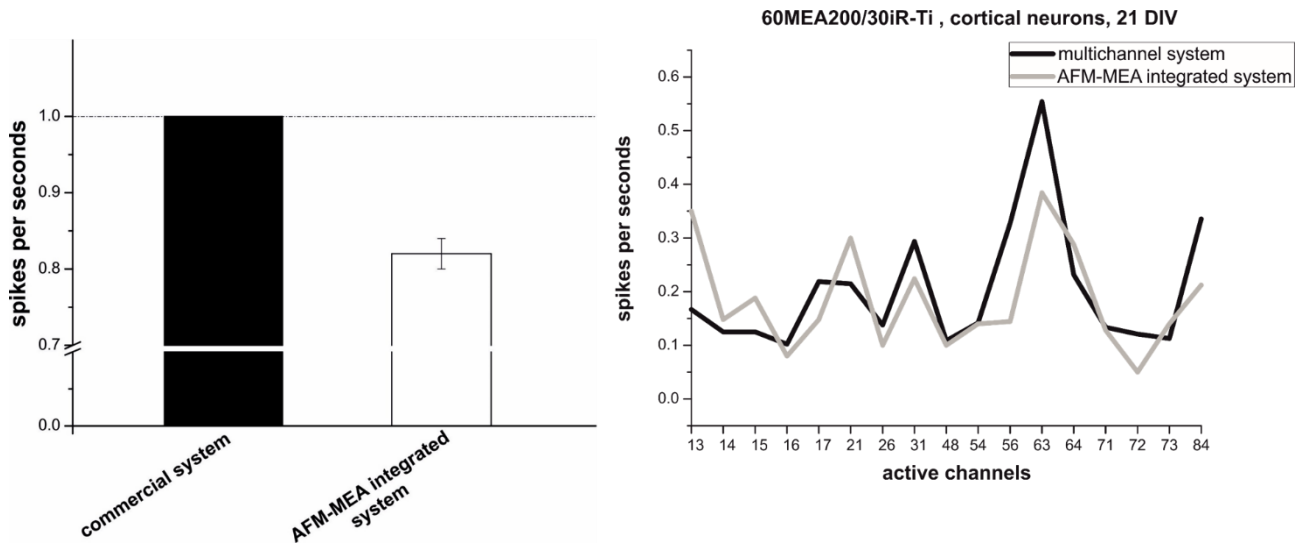


Figure 9.7: The graph on the left shows the firing activity recorded with the commercial system and the AFM-MEA integrated system: values are normalized with respect to the ones recorded using the commercial system, and data are shown with mean and standard deviation; on the right, the firing activity on the most active electrodes recorded using the two systems is shown.

Consequently, an appropriate noise thresholding procedure must be used to achieve a suitable accuracy of the spike detection algorithm. As shown in fig. 4.7, the mean firing rate values calculated from recordings taken with the two systems on the same neuronal culture are very similar, this showing that the AFM-MEA integrated system provides reliable results on the activity of cortical neuronal networks.

4.2.2 Neuronal Patterns

The importance of patterning cells was explained in the first chapter. Mechanotransduction studies using the AFM-MEA integrated system would benefit from having the possibility to get a controlled cell distribution over the MEA surface to better discriminate the effects of the mechanical stimulation.

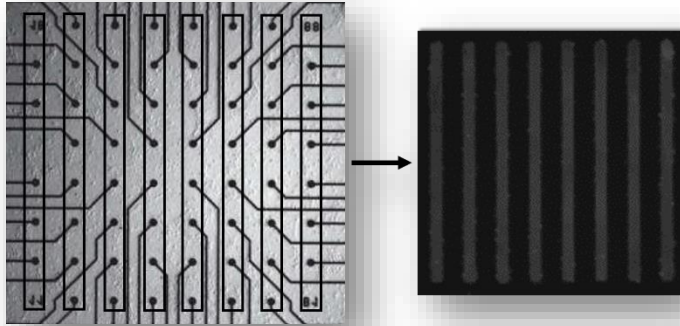


Figure 4.8: Illustration of the geometry chosen to fit the electrodes layout (on the left), and a fluorescent image of the adhesion factors patterned on glass.

As an example, one can think of having small clusters of cells to adhere and grow onto the electrodes area and being connected with each other. For this purpose, a geometry consisting of parallel lines with the same width and pitch distance of the microelectrodes in the array was chosen, as shown in fig. 4.8.

The patterning technique that I used is the microcontact printing technique, described in the previous chapter.

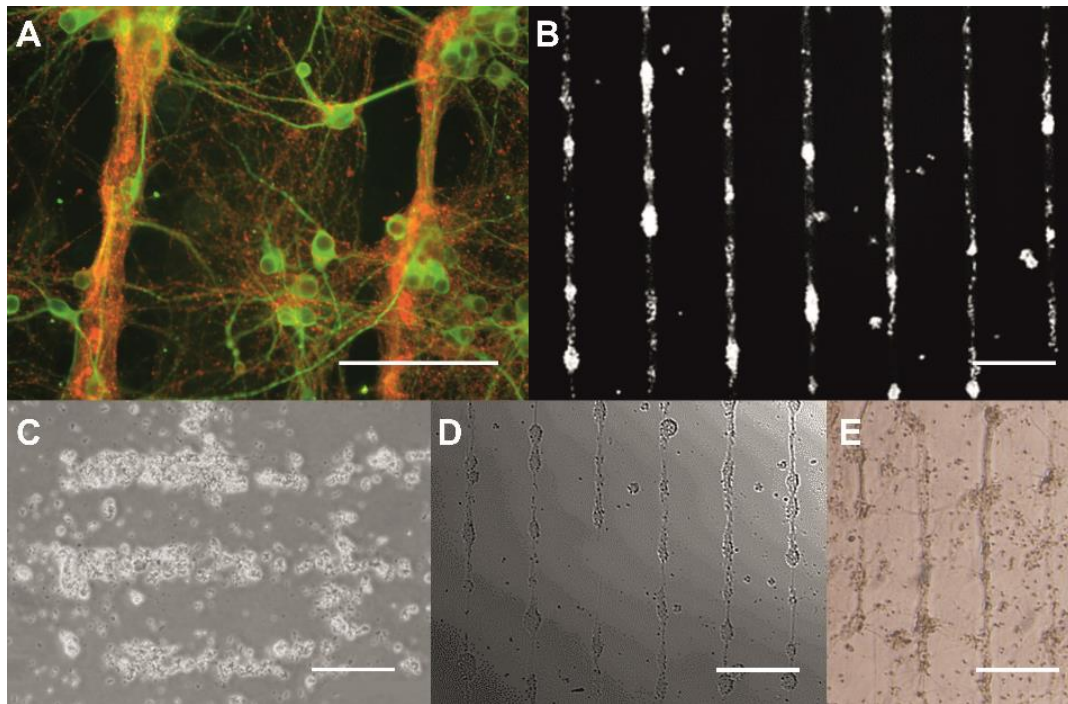


Figure 4.9: Images of the most significant cell pattern results on glass. In particular, image A shows lines of patterned neurons subjected to a process of immunolabeling for the MAP-2 dendritic protein (in green) and for the synapsin protein (in red), at 18 DIV (scale bar = 100 μ m); images B, C, D, E show different neuronal culture patterned on glass at 10 DIV, scale bar = 200 μ m.

After many trials, I could identify the appropriate pressure and time parameters for stamping a pattern of the selected adhesion factor on a glass substrate. Despite being successful on glass (as an example figure 4.9 show results obtained with an 18-days old neuronal culture), I could not get reliable results when printing onto the MEA substrate.

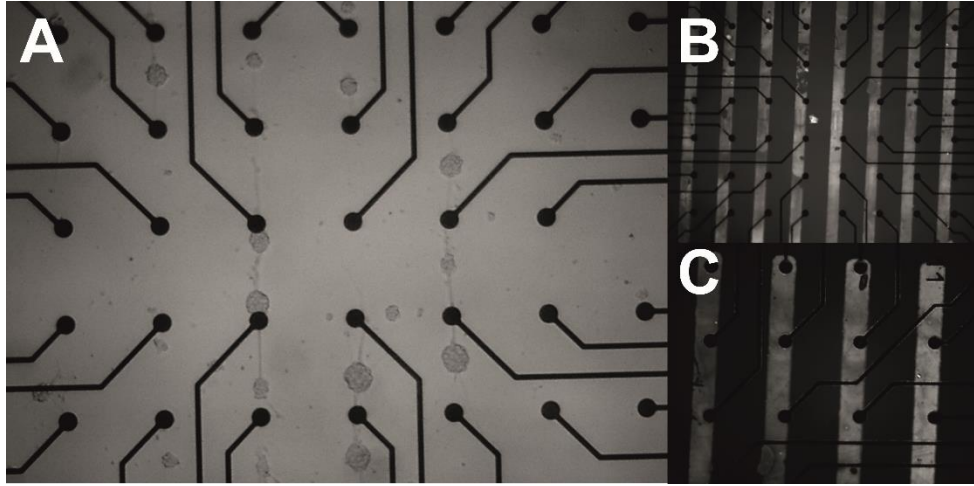


Figure 4.10: A) An attempt to obtain lines of neurons upon the electrodes; B) and C) fluorescent images of adhesion factors on the electrodes. The distance between two electrodes (centre-centre) is $200\mu\text{m}$.

As far as hPSC-CMs is concerned, the same method was not applied to obtain lines of cells plated upon the electrodes. This type of cells was cultured to form spheroidal clusters large enough to be manipulated with the micropipette. The challenge thus consisted in plating one single cluster precisely on one or a group of electrodes (in the case of high density MEAs) in order to have the conditions to stimulate one cluster and record the electrical response from a reduced number of electrodes.

4.2.3 Mechanical Stimulation of hPSC-CMs

The implemented setup allowed the simultaneous visualization, synchronous recording and coupled analysis of the electromechanical features of the beating cardiac clusters (BCCs). The lowest observable noise level in the MEA extracellular field potential (EFP) traces was 1mV peak to peak.

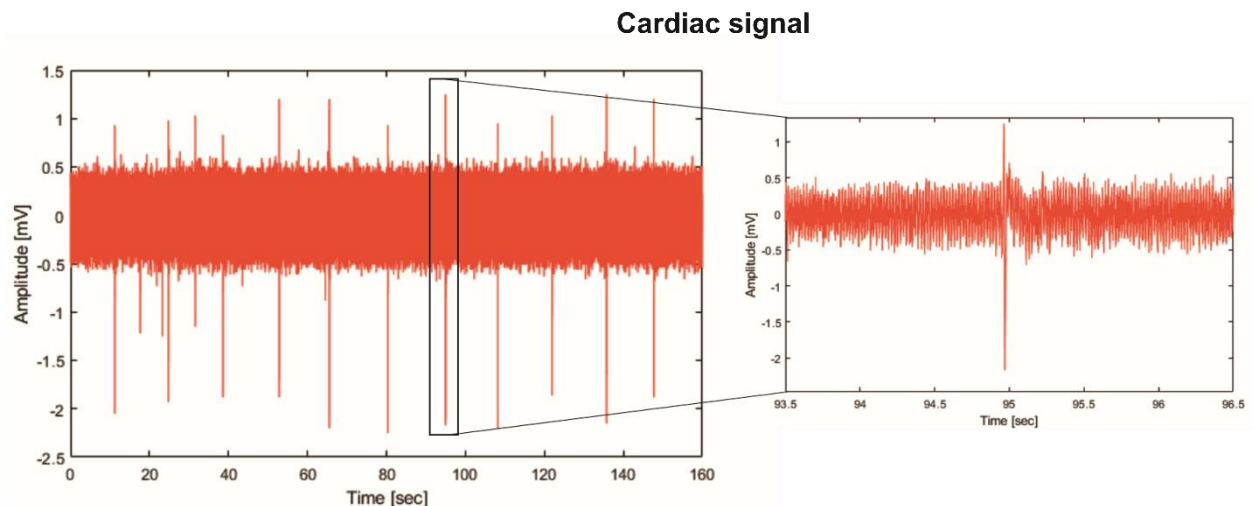


Figure 4.11: Cardiac extracellular signal recorded using the custom recording board.

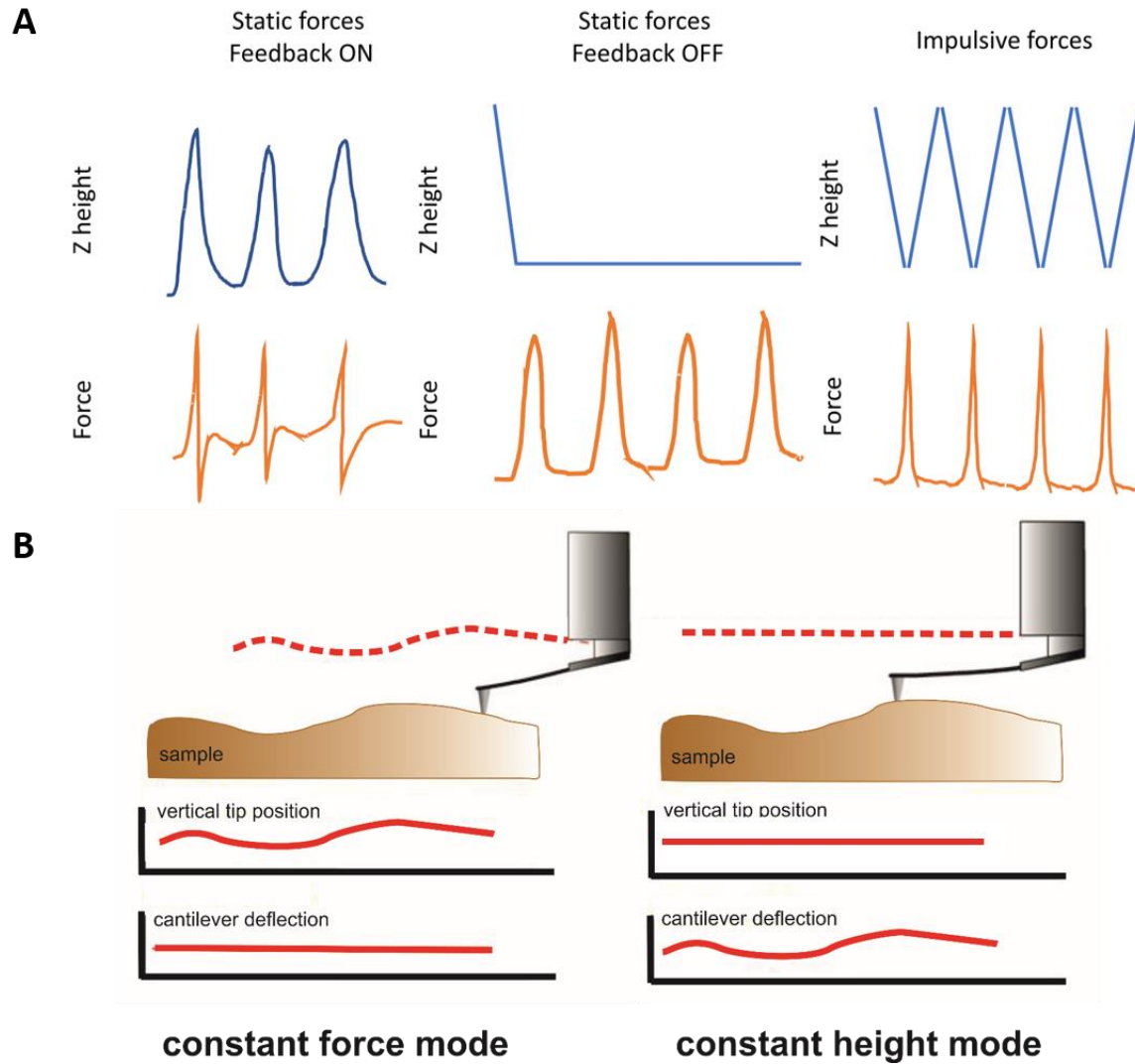


Figure 4.12: A) Illustration of piezo position and force in different modes of operation; B) differences between the constant force and the constant height mode: in the first one, the cantilever deflection is kept constant and the piezo moves to maintain it; in the second mode, the piezo height is kept constant while the cantilever deflection changes with the topography of the sample.

A protocol for the mechanical stimulation of hPSC-CMs was developed to validate the use of this beating cardiac clusters as model of mechanically-induced arrhythmia. The table below summarize the experimental protocol:

Work using	Application of	Detection of
Tipless cantilevers with high spring constant	Static forces to simulate hypertension, and in particular: <ul style="list-style-type: none"> • <u>constant force</u> to measure the variations of topography due to cell deformation (feedback loop on) • <u>constant height</u> to measure the transversal force transmitted on the cantilever (feedback loop off) 	Extracellular Field Potentials (EFP)
High density MEA devices with internal reference electrode	Impulsive forces to simulate a localized conduction block (e.g. commotio cordis) in the cardiac cycle: <ul style="list-style-type: none"> • force-distance curves at <u>different forces and frequencies</u> (1, 2, 5 Hz), imposed as approach speed 	Contractility disturbances, and, in particular, changes in: <ul style="list-style-type: none"> • heart beating rate • signal amplitude • signal morphology
Healthy hPSC-CMs	Transient overload (mixed impulsive and static forces)	

Table 4.3: Experimental protocol for hPSC-CMs.

So far, cell behaviour in response to mechanical stimuli was tested, using three type of tipless cantilevers, with different spring constants, high density MEA devices (HD MEAs), and the following stimulations:

1. Static forces
 - 10-100nN
 - 100-500nN
2. Impulsive forces
 - 100-500nN, 1-5 Hz
 - 200-1000nN, 1-5 Hz
3. Constant height, 100-200 nN
4. Transient overload, 50-100 nN, 2 Hz

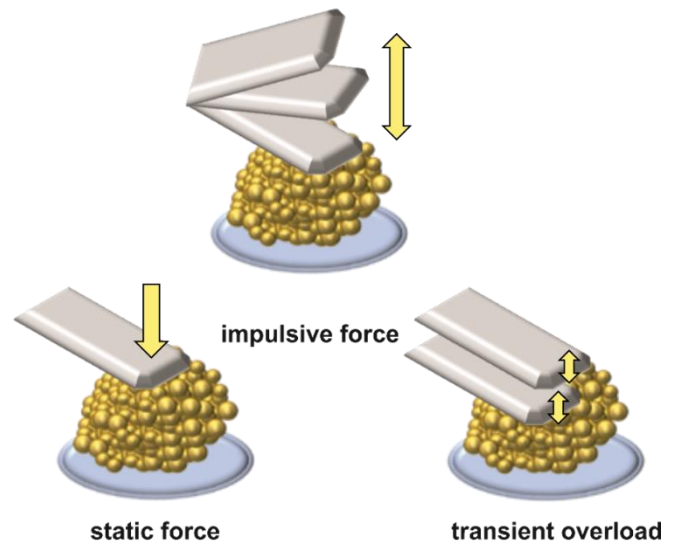


Figure 4.13: Interaction between the cantilever and the beating cardiac cluster during the application of static force, impulsive force and transient overload.

Each measurement lasted between 2 and 3 hours, without any visible alteration of the BCC morphology, and, at the end of the experiments, samples was refilled with antibiotics-containing medium, as the measurements took place in a condition that were not completely sterile. In this way, cells stay cultured without visible contamination for up to 4 days, proving that the BCC model presents an outstanding resilience.

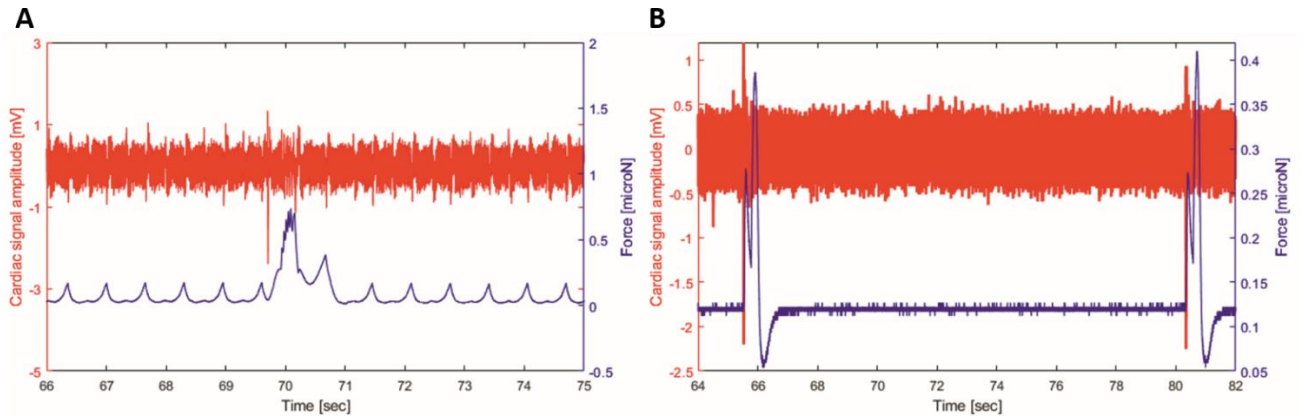


Figure 4.14: Overlap of the recorded cardiac and force signals during the application of impulsive forces (top) and during the application of static forces (bottom) as illustrated in fig. 4.12 A.

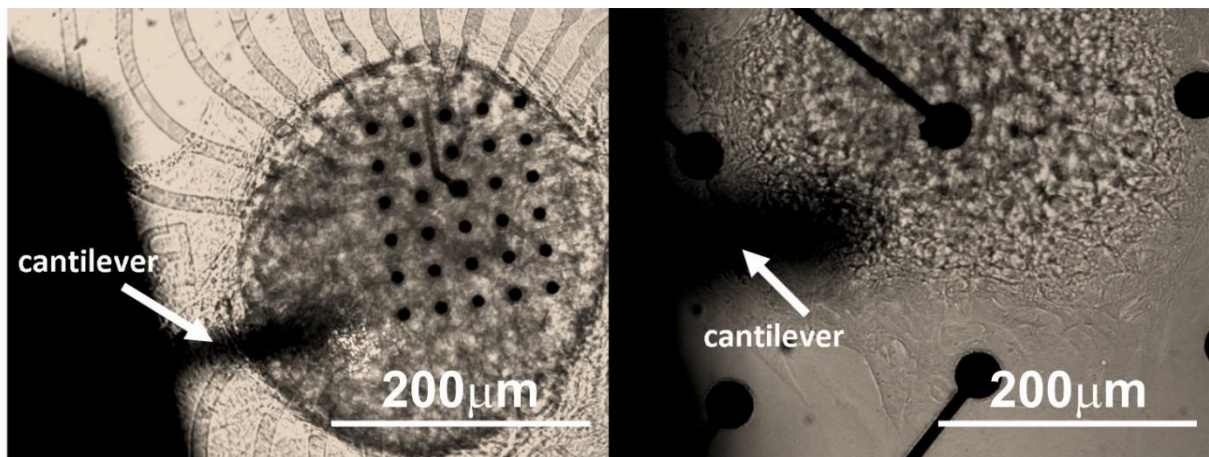


Figure 4.15: Optical images of beating cardiac cluster plated on a HD MEA (on the left), and on a standard MEA (on the right); in both images it is possible to distinguish the cantilever, the cells and the electrodes.

Preliminary results are not showing significant changes in terms of cardiac electrical signal amplitude and beating rate. The application of static and impulsive forces below 500 nN did not induce any alteration of the above-mentioned parameters, while static force stimulations in constant height and transient overload seems to reduce the beating rate (fig. 4.17, A). Moreover, the application of impulsive forces up to 1000 nN at 4 Hz resulted in a 44% increase in signal amplitude compared to the baseline (fig. 4.16, A). This very preliminary experimental stage had the purpose of trying a range of force intensities and types of tapping to evoke a mechano-electric feedback and deepen the knowledge concerning this particular response.

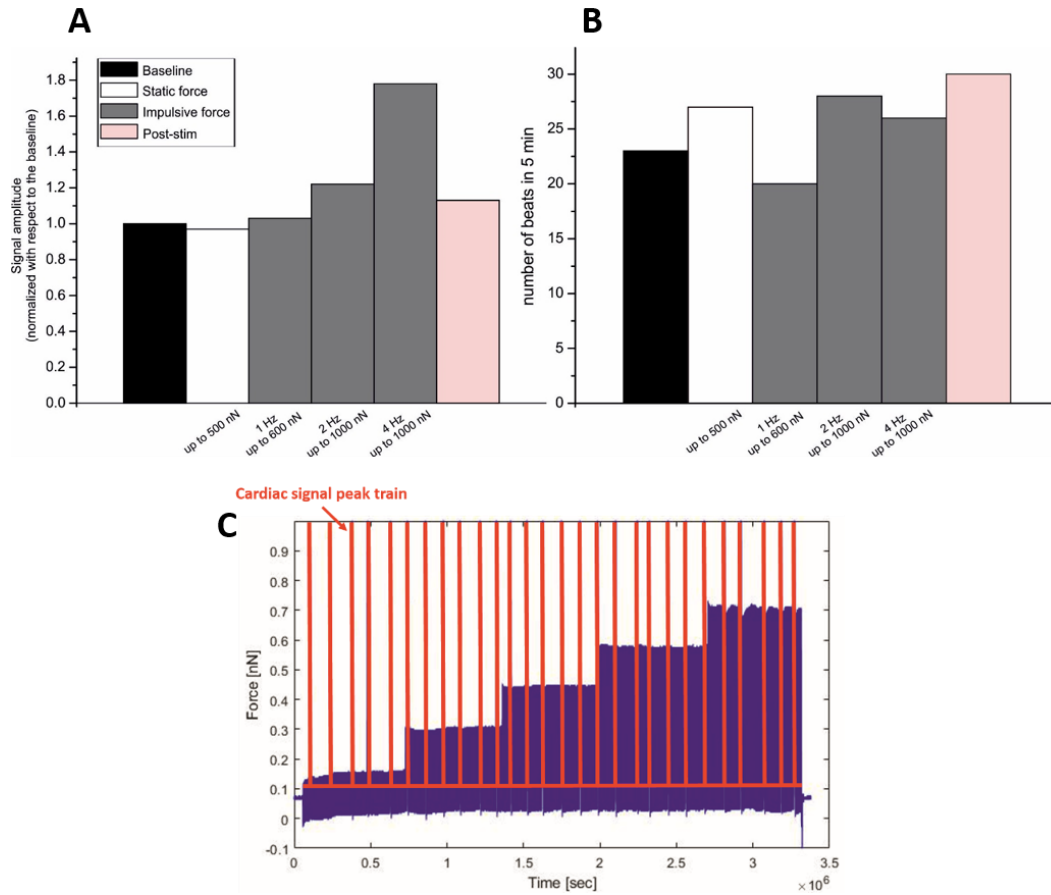


Figure 4.16: Signal amplitude (A) and beating rate (B) trends during the application of static and impulsive forces; C) overlap of the force signal and the cardiac signal peak train (every peak is a beat).

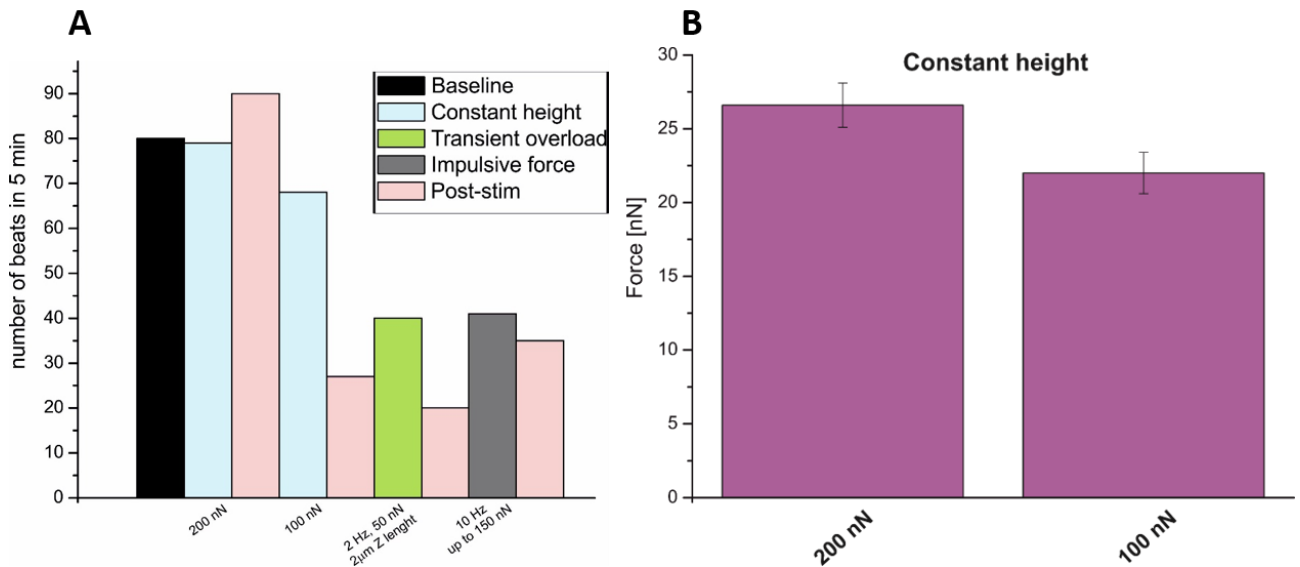


Figure 4.17: A) Beating rate trend during the application of static forces, transient overload and impulsive forces; B) transversal force transmitted by cells to the cantilever during the application of static forces in constant height mode.

The scarcely-conductive coupling between the MEA planar electrodes and the cells was the reason why at least half of the plated samples were not able to produce a visible extracellular field potential trace while mechanically beating. In fact, the morphology of the cell signal is dependent on the

conductive sample/electrode proximity and high resistance cleft, as explained in the introduction of this thesis work [59]. As BCCs present a mixed cell population of cardiomyocytes and fibroblast-like cells, it is likely that a non-conductive patch might adhere to the electrode area. This issue can be solved by removing gently and re-plating BCCs in sterile conditions.

The low significance of the results could be due to the fact that the dimensions of the beating cluster were higher than the volume of the cantilever used as probe; they also could be influenced by their inhomogeneity (BCC contain cardiomyocytes and fibroblasts-like cells) and conduction pattern variability. To overcome these issues, it is necessary to obtain cell clusters which have the same reduced dimensions (e.g. max 100 μm in diameter), which should be comparable to the probe size. This purpose could be reached by stamping well arrays on agarose substrates, adding the cell suspension and centrifuging it to let cells precipitate inside the well and shape themselves in the same way.

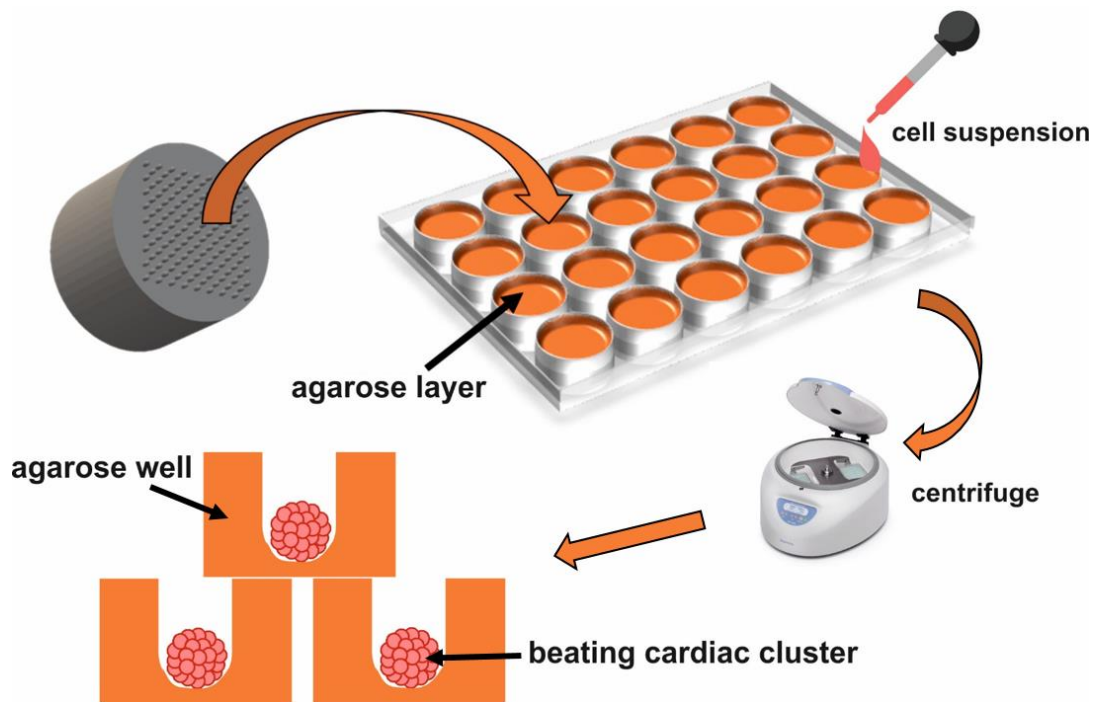


Figure 4.18: Using an adequate mould, well arrays could be designed on an agarose substrate; after the addition of cell suspension and centrifuge it, cells will precipitate to the bottom of the caves, assuming the same shape.

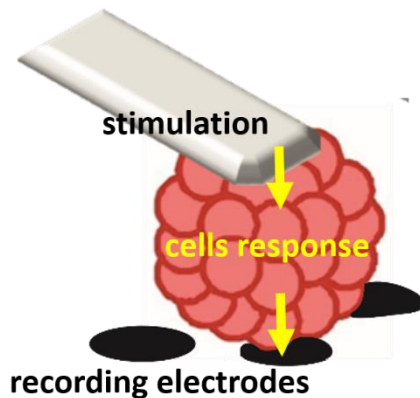


Figure 4.19: The detection of cell response after a mechanical stimulation could be improved by reducing the cell.

In the same optics, in order to further investigate the effects of mechanical stimulation, size reduction will decrease the distance between cells in the top cluster (that are in direct contact with the stimulation probe) and the ones on the bottom coupled with the recording electrodes.

Furthermore, it is necessary to replicate protocols in beta-adrenergic stimulation (e.g. isoprenaline), calcium channel blockers (e.g. verapamil or gentamycin for stretch-activated ones) and use the constant-current pacing to study the MEF in a more controlled setting. Future improvements in this direction could provide more significant results.

4.3 Mechanical Characterization of a 3D Alginate-Matrigel Hydrogel as Scaffold for Human Breast Cancer Cells: Results

Using AFM nanoindentation technique, the Young modulus of each hydrogel was measured at the sub-micrometre scale, the same length scale of the actual cell sensing [85]. The slope of the force curve after contact showed a negligible hysteresis between loading and unloading, which indicates a mainly elastic deformation of the hydrogels. Stiffness values were obtained using the same cantilever and the same approach-retract speed (4 $\mu\text{m}/\text{sec}$). The average force-distance curves for each hydrogel are displayed in fig. 4.20, panel B. The curves show a qualitative, yet evident, difference in the compliance of the different hydrogels while deformed by the AFM tip. Panel C in fig. 4.20 reports mean values and standard deviation of the Young modulus measured over the hydrogel surface by AFM nanoindentation, following the procedure described in the previous chapter. The Young modulus varies significantly when changing alginate-to-matrigel concentrations (100% alginate, 75%:25% alginate:matrigel, 50%:50% alginate:matrigel), and, in particular, it decreases with the reduction of the alginate concentration. The Young modulus value of the sample with the higher concentration of alginate was in the range 66-76 KPa, while the sample with the lower concentration of alginate resulted softer (24-26 KPa). The results demonstrate that hydrogel stiffness is dependent on alginate concentration. As reported by Samani *et al.* [86], the Young modulus of an intermediate-grade IDC (Invasive Ductal Cancer) calculated on 21 samples is about 19.99 ± 4.2 kPa. This appears to be in agreement with the stiffness of 50%:50% A:M gels.

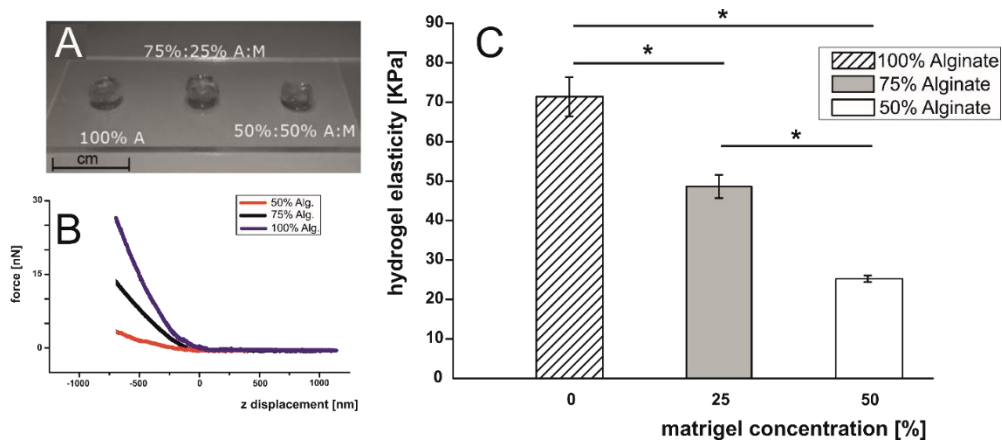


Figure 4.20: (A) The three types of obtained compact gels; panel B shows three representative forces versus vertical displacement curves measured on three different hydrogels. The $z = 0$ corresponds to the vertical piezo displacement where the AFM tip gets into contact with the hydrogel surface; panel C shows the Young modulus average and standard deviation for the different hydrogels probed by AFM nanoindentation: bar colours correspond to different alginate concentrations, while matrigel concentration is shown along the x axis (Kruskal-Wallis test, $p < 0.05$).

Tumour cells in the hydrogels demonstrated high viability and density, as shown in the fig 4.21: Although initial cellular proliferation in gels on day 4 was marginally low, it recovered on day 7 (number of samples: $N \geq 10$).

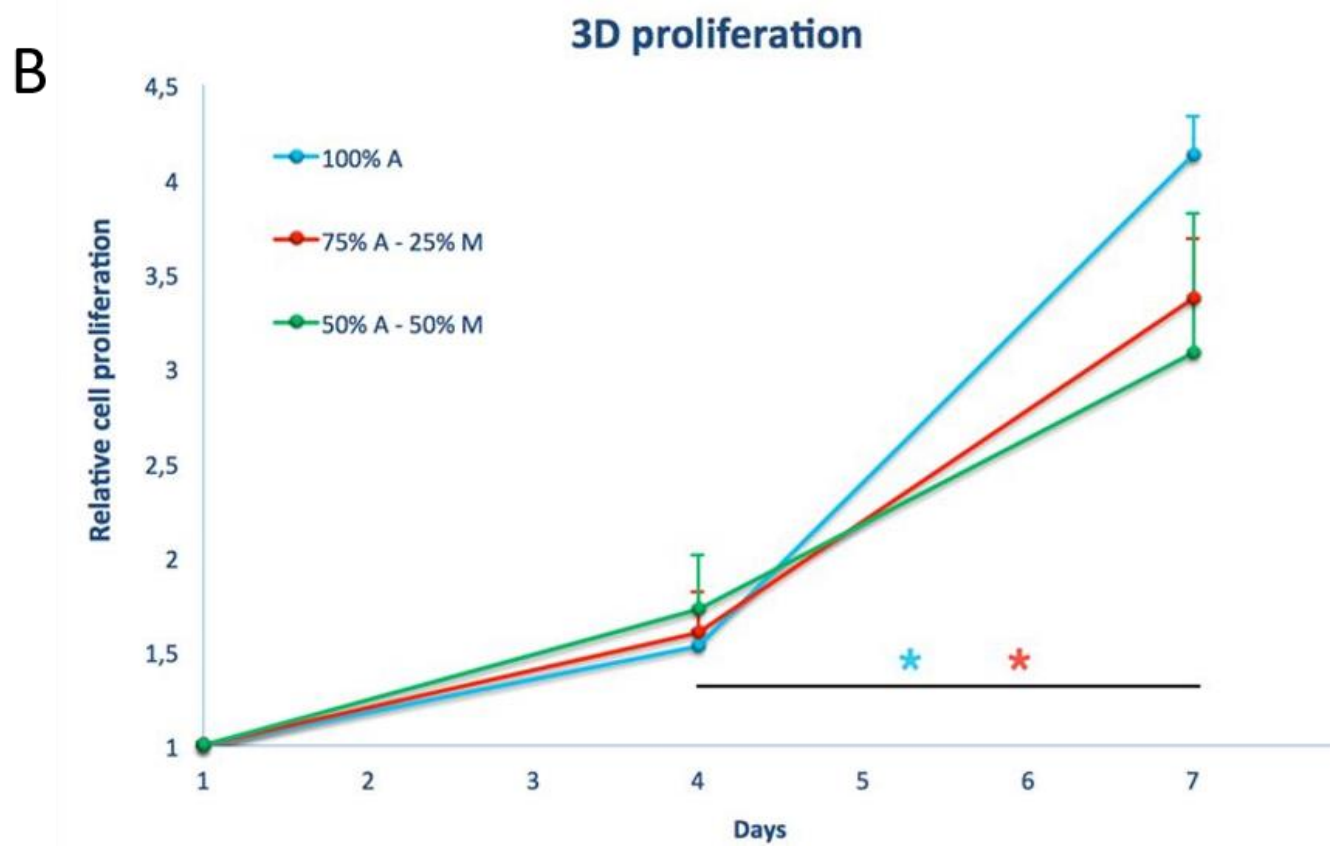
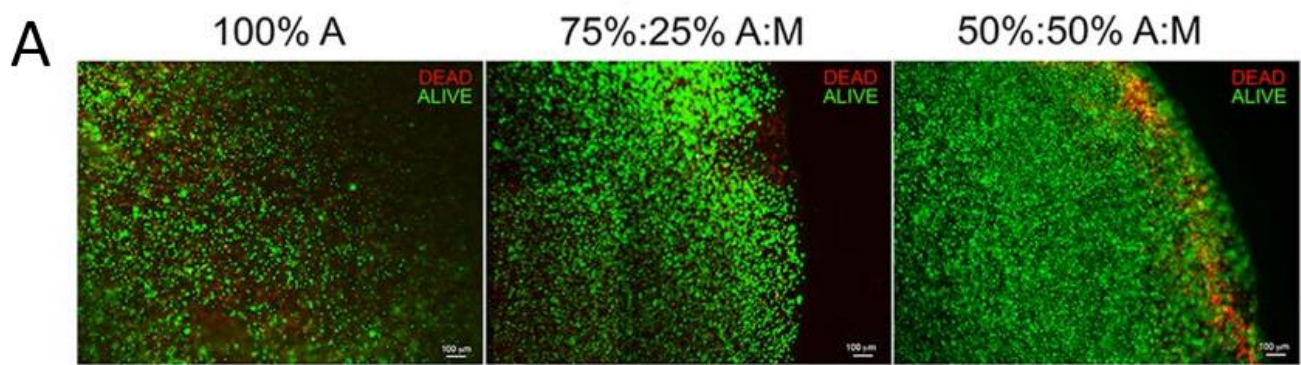


Figure 4.21: A) MDA-MB-231 cells cultured within materials for 24 h, stained with fluorescence dyes: calceinAM (green) for live cells and propidium iodide (red) for dead cells. B) MDAMB- 231 cell proliferation after 4 and 7 days of culture for different materials. Symbol *indicates statistical significance (ANOVA test; number of samples: $N \geq 10$; $p < 0.05$).

MDA-MB-231 cells expressed their typical elongated and stellate morphology in 2D and *in vivo* (xenograft) conditions. To obtain a similar conformation in a 3D environment, cell morphology was analysed within the three different types of gels at three different time points (1, 4 and 7 days).

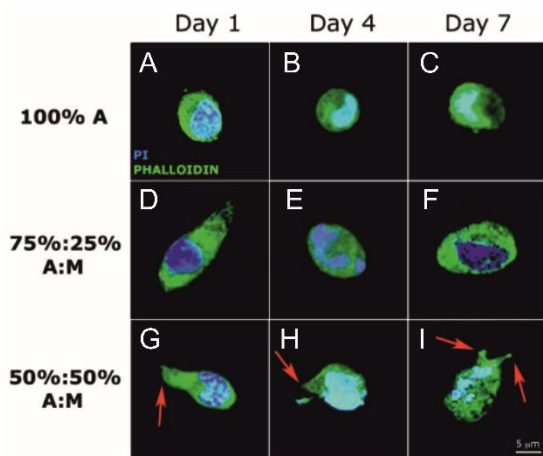


Figure 4.22: (A-I) Confocal sections of cells embedded within Alginate/Matrigel gels at different time points. Cells were stained for F-actin (phalloidin) and nuclei were counterstained with Propidium Iodide. To be noted that cells show stellate morphology and invadopodia (red arrows) in 50%:50% A:M gels (G, H, I).

In alginate gels, cells maintained a round morphology, typical of suspension phase and expressive of a non-malignancy condition (fig. 4.22, A-C), while, in presence of matrigel, cells tended to elongate, accordingly to their aggressiveness (fig. 4.22, D-I). More interestingly, and in contrast to 2D controls, in the same gels, a nuclear fragmentation, known to be linked to malignancy, was observed. In fact, while nuclei assumed a round and regular shape in 100% A gels (fig. 4.23, A), they showed a multiple and irregular conformation in presence of matrigel (fig. 4.23, B and C). Finally, only in 50%:50% A:M gels, cells have manifested invadopodia (fig. 4.22, G-I), actin-based protrusions of the

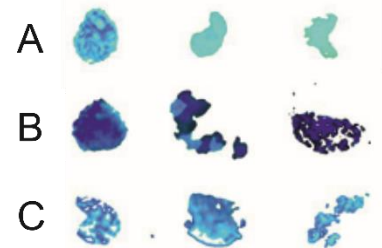


Figure 4.23: (A-C) Nuclei shapes isolated from A-to-I at fig. 4.22. In presence of Matrigel cells express nuclear fragmentation, characteristic of malignancy.

plasma membrane through which cancer cells anchor to the Extracellular Matrix and degrade it.

It is a proven fact that 3D cultures are essential for a better comprehension of cell behaviour, as they mimic an environment more similar to the *in vivo* one [87], and this is extremely important in pathological conditions, such as in cancer studies. The microenvironment plays a role as a regulator of tumour progression [88], and recent studies have demonstrated that instead of 2D culture, the 3D matrix of animal-derived biomaterials such as Matrigel can significantly mediate the breast-cancer phenotype.

It is very interesting to observe that these morphological features were expressed by cells only in those gels having the same mechanical properties of *in vivo* tumours, highlighting the importance of mechanical and not only chemical properties of the 3D environment. The ability of the cell to migrate was also studied using a bioreactor-based set-up, and results show that cells displayed a greater tendency to migration in 50%:50% alginate:matrigel gels. This new 3D model of aggressive breast cancer allows human carcinomas to grow *in vitro* and to maintain many typical *in vivo* properties, such as 3D architecture, nuclear fragmentation and invadopodia manifestation, and migration capability. It can be used for a prolonged cell culture time thanks to the mechanical robustness provided by the alginate component and, at the same time, it is permissive to cell migration and motility thanks to the Matrigel part. This 3D cell-laden hydrogel due to its characteristic to simulate the *in vivo* condition can provide a completely new approach for studies on invasive breast cancer and drug testing.

4.4 Characterization of the Topographical Features of Graphene-Oxide Functionalized Substrates to Study Cells Adhesion: Results

Graphene-oxide/alginate (GO/Alg) nano-composite films were fabricated by using a CaCl_2 crosslinking solution, and they were characterised and compared with the alginate (Alg) substrates. Topography images of the Alg and GO/Alg hydrogel films were obtained by AFM operated in contact mode. The AFM images (fig. 4.24, A) revealed distinct surface morphologies for the different substrates: Alg films displayed a regular granular surface profile, while GO/Alg films exhibited a less regular porous surface morphology, characterized by numerous peaks and valleys. The average surface roughness at the nanoscale was significantly higher ($p < 0.05$) in the polymeric films functionalized with GO: 2.68 ± 0.56 nm for Alg substrates, and 6.25 ± 1.17 nm for the GO/Alg ones.

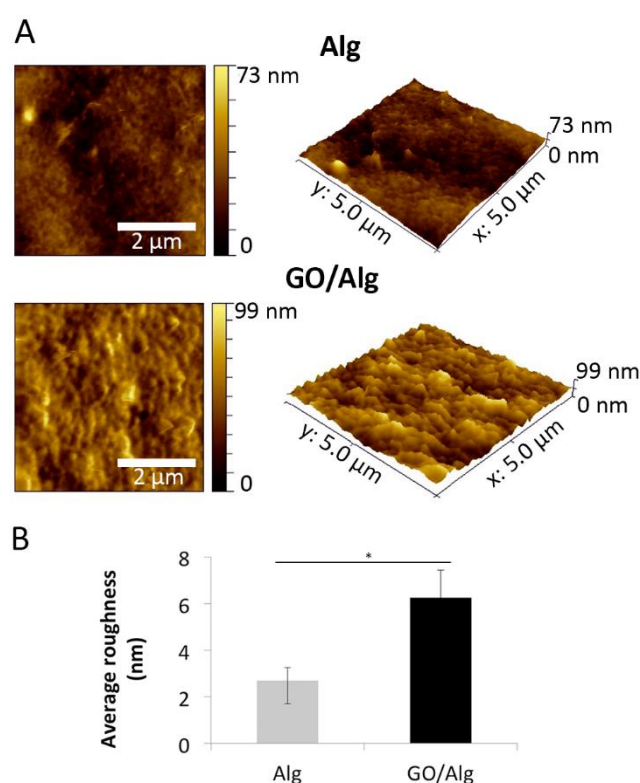


Figure 4.24: AFM images of an area of $5 \mu\text{m} \times 5 \mu\text{m}$ of Alg and GO/Alg films, respectively (panel A); quantitative analysis of average roughness of Alg and GO/Alg substrates. Values are reported as mean value and standard deviation. Symbol * indicates samples with statistically different elasticity (Kruskal-Wallis test, $p < 0.05$) (panel B).

Cell proliferation was quantified after 1 and 7 days of culture, by normalizing the proliferation rate to the number of cells detected after one day of culture (fig. 4.25). Interestingly, no significant differences were observed between Alg and GO/Alg substrates for the three cells lines. Therefore, GO addition to the substrates seems not to induce any significant effect on the

Nano-indentation measurements were also performed using the AFM in order to evaluate the Young modulus of each hydrogel film at the sub-micrometre scale. The calculated elastic modulus varies significantly between Alg and GO/Alg hydrogel film ($p < 0.05$), increasing with the GO addition. The elasticity value of the Alg substrate was of 518.88 ± 46.26 KPa, while the GO/Alg ones resulted stiffer (732.74 ± 160.97 KPa).

The biological interactions between cancer cells and graphene-based films was evaluated by testing cytotoxicity, spreading areas, proliferation, and expression of adhesion proteins of the three different cell lines, the human breast cancer cells (MDA-MB-231), a cancer cell line from human osteosarcoma (HOS) and healthy murine fibroblasts (3T3). It was observed that, for all the samples, cells were mostly alive ($>95\%$), suggesting the non-toxic nature of graphene oxide nano-sheets. In particular, breast cancer cells preferred to adhere and attach over the graphene-free based substrates, while both HOS and 3T3 exhibited an opposite trend, showing an improved adhesion efficacy when cultured on the GO/Alg substrates.

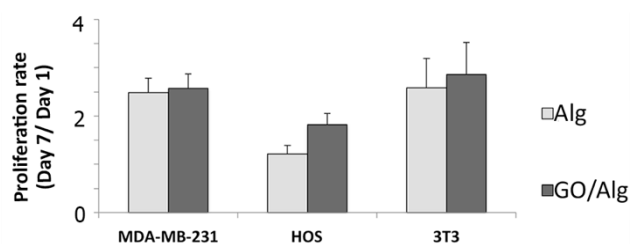


Figure 4.25: Proliferation rate of MDA-MB-231, HOS and 3T3 cell lines up to one week of cell culture over Alg and GO/Alg substrates.

proliferation efficacy, while it plays a key role in determining cell adhesion to a specific preferential substrate.

To analyse the effect of GO addition on the cellular cytoskeletal organization and expression and on the cell spreading patterns, cell types were cultured over the Alg and GO/Alg films, and, after 24 hours they were immune-challenged. This procedure permits the detection of vinculin and actin filaments (fig. 4.26), which are intracellular proteins involved in protein anchoring or in cytoskeletal attachment, respectively.

The normalized ratio between the vinculin- and actin-positive cell surface areas over the total cell area in 3T3 and HOS was significantly enhanced by the addition of GO if cultured onto GO-embedded substrates.

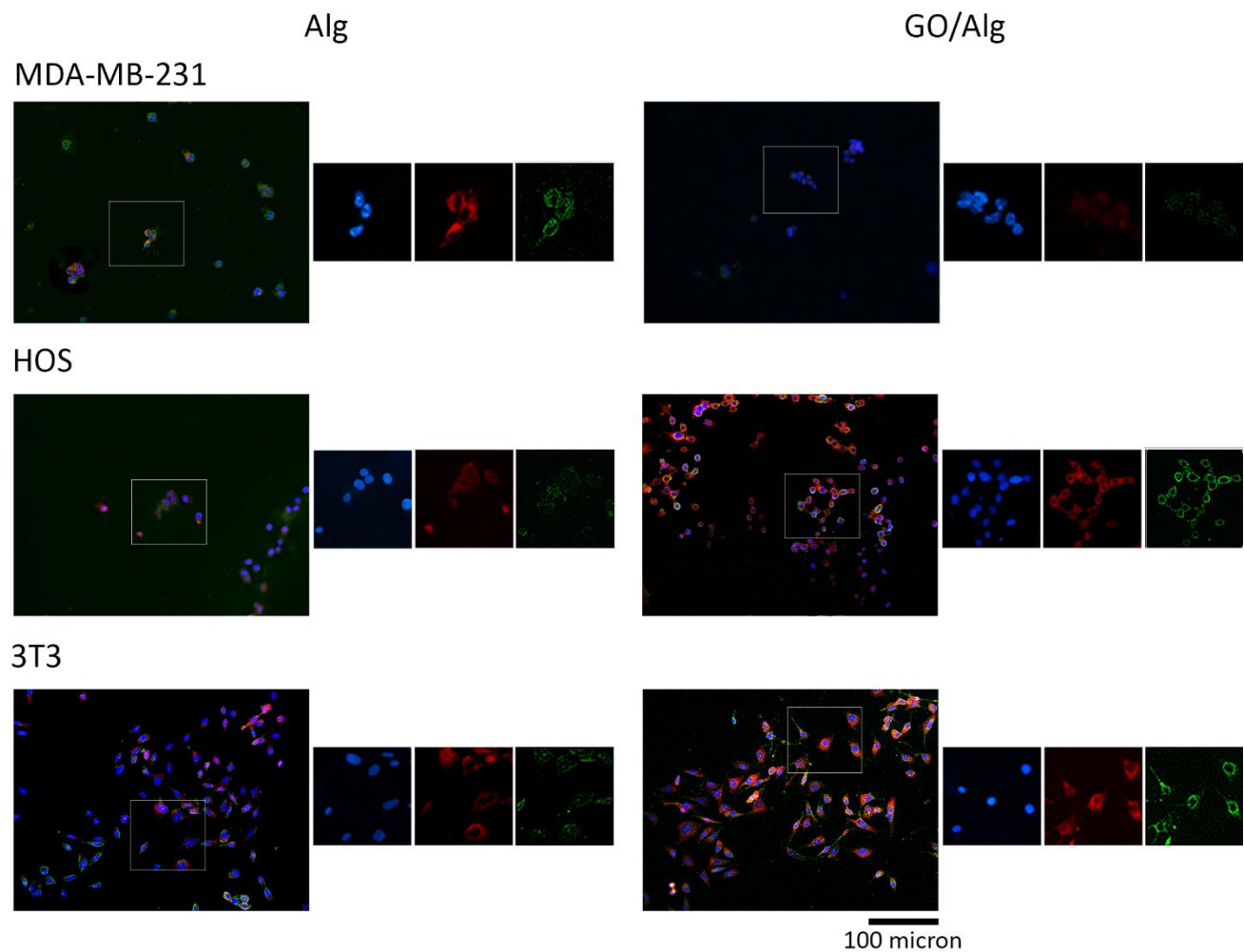


Figure 4.26: Cell adhesion patterns on Alg and GO/Alg substrates. The three cell lines were cultured over each substrate for 24 hours. Actin and vinculin were stained with phalloidin-TRITC and a monoclonal antivinculin antibody, respectively. The merged images show actin (red), vinculin (green), and the DAPI-stained nucleus (blue).

The cell area, the circularity, and the ratio between the cell main axes as proof of the elongated shape of the cells were quantified. In particular, the circularity of MDA-MB-231 was higher in GO/Alg substrates, while 3T3 and HOS showed an opposite trend, and both, the aspect ratio and the mean cell area were significantly higher over GO/Alg substrates for 3T3 and HOS and lower for MDA-MB-231.

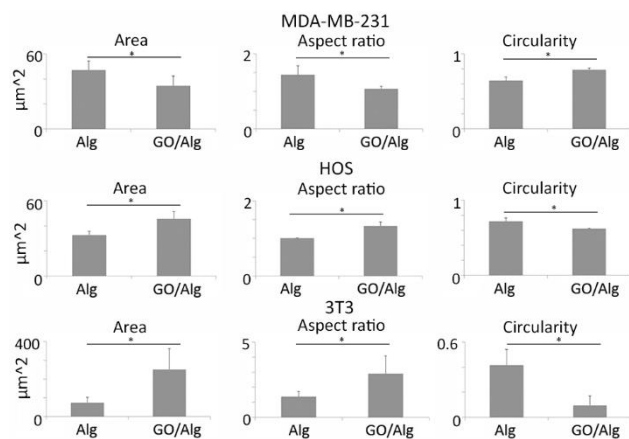


Figure 4.27: Analysis of the morphological parameters of cells cultured the substrates for 24 hours. Values are reported as mean + SD * indicates $p < 0.05$ significance.

All these results indirectly suggest that 3T3 and HOS, differently from MDA-MB-231 cells, organize closer cell-to-substrate contacts and display a higher affinity specifically for GO/Alg substrates. On the contrary, a more enhanced positive vinculin and actin staining can be observed for the metastatic breast cancer cells only when cultured over GO-free Alg films, as shown in fig. 4.26. That is because a higher substrate stiffness due to the GO-presence, inhibits the MDA-MB-231 adhesion process, uncoupling the adhesion requirement for cell growth from its consequent and mandatory cytoskeletal rearrangement.

The migration of cancer cells through the extracellular matrix is an example of the relevance of nanoscale level sensitivity of the substrate characteristics [89], within which cell processes such as detachment, movement and migration can be observed. These are the results of an organized localization and generation of cell–matrix interaction and focal adhesions sites, and specifically the formation of these F-actin filaments network is mediated by the vinculin adhesion protein [90, 91]. The GO addition in this experimental system inhibited the F-actin cytoskeleton assembly in breast cancer cells, which is a mandatory requirement for the migratory and invasive phenotype of these cancer cells [92]. This confirms the finding that 3T3s, like many cells of mesenchymal origin, preferentially interact with stiff and nano-rough substrates [93, 94], are considered anchorage-dependent cells [95], and gain growth advantages when cultured on nano-micro-scale structures in bio-based materials [96, 97].

The nanometre-scale features of a substrate play a crucial role in adhesion sites formation and function, regardless the carcinogenic nature of cells, as proven by the dual mode of effects exerted by GO on MDA-MB-231 and on HOS or 3T3 adhesion. In fact, even transformed cells seem reminiscent of their anatomical and developmental origin and take advantage of their peculiar preference toward substrates that display the same physical characteristics of their native tissues of origin: although breast tumours are stiffer than normal breast tissue, in fact, they still remain markedly softer than bone or muscle [98]. GO can thus be thought of not only as a molecular chemotaxis agent for growth factors [99] but also as a discriminant environmental cue at the nano-scale level in cell-surface interactions. Hence, adequate *in vitro* modelling and culturing setting for each cancer cell type should be reproduced by properly tuning the substrate physical cues, in order to more precisely study and more effectively act against metastatic processes.

4.5 Probe Size Effect on AFM Nanoindentation Measurements: Results

PDMS stiffness was evaluated by AFM nanoindentation measurements using different tip sizes. Load versus indentation curves were extracted by considering the contact region of standard AFM force curves. The load applied by the tip was calculated first by converting the output voltage from the AFM photodetector into nanometres of cantilever deflection, and then by multiplying the deflection values by the cantilever spring constant. The indentation corresponding to every applied load was calculated by comparing the force curve taken on the deformable PDMS substrate with a reference one taken on an ideally hard substrate (glass). From the load versus indentation curve, the elastic modulus of the sample was extracted using the model proposed by Oliver and Pharr [83]. Nanoindentation measurements were performed over a square grid ($5 \times 5 \mu\text{m}$) in order to consider intra-sample heterogeneity. For each sample, three maps of 16×16 force curves were collected onto three randomly selected regions.

A custom-software developed in LabVIEW environment (National Instruments) was used for processing force curves and extract Young modulus at a given maximum indentation. Preliminary results on a homogeneous elastic material such as PDMS did not show statistically significant differences in Young modulus obtained with spherical indenters of different sizes (fig. 4.28). This would allow to use indenter probes of different sizes to measure mechanical properties (e.g. elastic modulus) at different scale lengths using the same technique by simply changing the indenter size: for example it would be possible to probe the stiffness of a specific single cell as a whole using with a $50 \mu\text{m}$ diameter sphere and sub-cellular features of the cytoskeleton of the same cell using a different cantilever on the same chip with a blunt conical tip with 200 nm radius of curvature, being able to compare directly the results obtained.

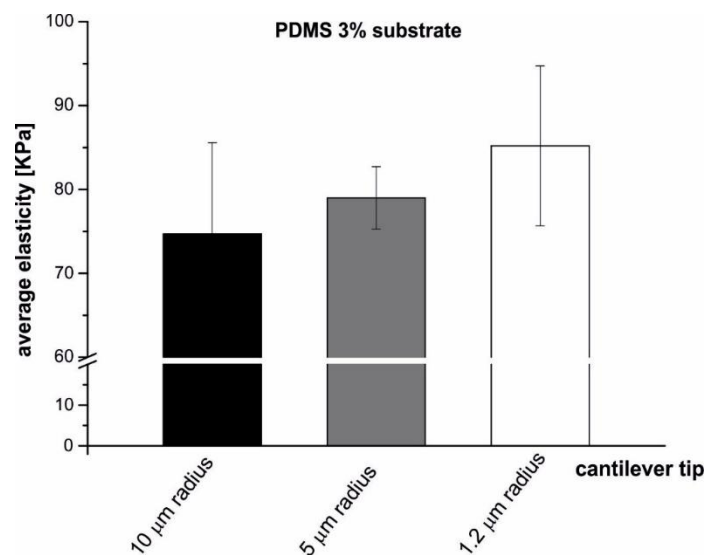


Figure 4.28: Young modulus values of a PDMS substrate obtained using three different type of nanoindenter.

Chapter 5

Conclusions and Future Perspectives

In this work, I presented and successfully tested a novel experimental system for the investigation of the electro-mechanical phenomena in neuronal and cardiac cells. The bioengineering approach adopted consists in integrating different experimental techniques for simultaneous measurement of cell electrophysiology and cell mechanical properties. The *in vitro* system I developed provides reliable temperature control and low electrical noise thus making it suitable for the investigation not only of cardiac myocytes as previously tested, but also of mature cultures of neurons. The employed systems and methods may open new ways in the investigation of the single excitable cell pathophysiology.

Although the system proposed in this work presents promising features for single cell studies, it still presents some limitations, such as the burden of cables and other electronic discrete components needed. Moreover, the level of electronic noise could be further reduced to allow more sophisticated measurement of neuronal activity (e.g. subthreshold membrane potential oscillations). Other possible improvement would be to exploit the possibility of electrical stimulation of the single cells using a nanoelectrode placed on the AFM tip.

Clearly, the future perspectives regard the development of protocols for cell mechanical stimulation. No protocols have been yet tested on neurons, while different protocols for the mechanical stimulation with AFM probes were tested on clusters of hPSC-CMs, unfortunately without evident signs of evoked electrical response. That was probably due to the large size of the cell clusters with respect to the indenting probe (a tipless cantilever). This problem can be overcome reducing on the cell cluster size together with the development of a procedure to standardize cell assembly in spheroids with dimensions comparable with the probe ones.

Finally, I would like to stress once more the potential of *in vitro* systems to systematically and reproducibly study cell response to different types of external (bio)chemical and mechanical stimuli, in order to build robust models of the *in vivo* conditions.

References

- [1] Iskratsch, T., Wolfenson, H. and Sheetz, M.P. (2014). Appreciating force and shape the rise of mechanotransduction in cell biology. *Nature Reviews Molecular Cell Biology* (15), 825-833.
- [2] Deok-Ho Kim, *et al.* (2009). Microengineered Platforms for Cell Mechanobiology. *Annu. Rev. Biomed. Eng.* (11), 203-233.
- [2] Condeelis, J., Segall, J.E. (2003). Intravital imaging of cell movement in tumours. *Nat. Rev. Cancer* (3), 921-930.
- [3] Hunt, T.K., Burke, J., Barbul, A., Gimbel, M.L. (1999). Wound healing. *Science*, 284:1775.
- [4] Turner, C.H., Pavalko, F.M. (1998). Mechanotransduction and functional response of the skeleton to physical stress: The mechanisms and mechanics of bone adaptation. *Journal of Orthopaedic Science* (3), 346-355.
- [5] Mullender, M. (2004). Mechanotransduction of bone cells in vitro: Mechanobiology of bone tissue. *Medical and Biological Engineering and Computing* (42), 14-21.
- [6] Williams and Bryan (1998). Mechanical influences on vascular smooth muscle cell function. *Journal of Hypertension* (16), 1921-1929.
- [7] Huang, H., Kamm, R.D., Lee, R.T. (2004). Cell mechanics and mechanotransduction: pathways, probes, and physiology. *Am. J. Physiol. Cell Physiol.* (287), C1-11.
- [8] Qiu, H., Zhu, Y., Sun, Z. *et al.* (2010). Short communication: vascular smooth muscle cell stiffness as a mechanism for increased aortic stiffness with aging. *Circ Res* (107), 615-619.
- [9] Illi *et al.* (2005). Epigenetic Histone Modification and Cardiovascular Lineage Programming in Mouse Embryonic Stem Cells Exposed to Laminar Shear Stress. *Circ Res.* (96), 501-508.
- [10] Jacot, J.G. (2010). Mechanobiology of cardiomyocyte development. *Journal of Biomechanics* (43), 93-98.
- [11] Bray, M.A. (2008). Sarcomere alignment is regulated by myocyte shape. *Cell Motility and the Cytoskeleton* (65), 641-651.
- [12] Tandon, N., *et al.* (2009). Electrical stimulation systems for cardiac tissue engineering, *Nature Protocols* (4), 155-173.
- [13] Chiu, L.L., Iyer, R.K., King, J.P., Radisic, M., (2008). Biphasic electrical field stimulation aids in tissue engineering of multicell-type cardiac organoids. *Tissue Eng. Pt. A.* (17), 11-12.
- [14] Tay, A. *et al.* (2016). Micro- and nano-technologies to probe the mechano-biology of the brain. *Lab Chip* (16), 1962-1977.

- [15] Tyler, W.J. (2012). The mechanobiology of brain function. *Nature Reviews Neuroscience* (13), 867-878.
- [16] Brouzés, E. and Farge, E. (2004). Interplay of mechanical deformation and patterned gene expression in developing embryos, *Curr. Opin. Genet. Dev.* (14), 367-374.
- [17] Anava, S. *et al.* (2009). The regulative role of neurite mechanical tension in network development. *Biophys. J.* (96), 1661-1670.
- [18] Lamoureux, P., *et al.* (2002). Mechanical tension can specify axonal fate in hippocampal neurons. *J. Cell Biol.* (159), 499-508.
- [19] Siechen, S., *et al.* (2009). Mechanical tension contributes to clustering of neurotransmitter vesicles at presynaptic terminals. *Proc. Natl. Acad. Sci. USA* (106), 12611-12616.
- [20] Kuciewicz, J. C. *et al.* (2007). Functional tissue pulsatility imaging of the brain during visual stimulation. *Ultrasound Med. Biol.* (33), 681-690.
- [21] Arnadottir, J. & Chalfie, M., (2010). Eukaryotic mechanosensitive channels. *Annu. Rev. Biophys.* (39), 111-137.
- [22] Chen, B. M. & Grinnell, A. D. (1995). Integrins and modulation of transmitter release from motor nerve terminals by stretch. *Science* (269), 1578-1580.
- [23] Bao, G., Suresh, S. (2003). Cell and molecular mechanics of biological materials. *Nat. Mater.* (2), 715-25.
- [24] Kaushik, G., Leijten, J., and Khademhosseini, A. (2017). Concise Review: Organ Engineering: Design, Technology, and Integration. *STEM CELLS* (35), 51-60.
- [25] Butler, D.L., Juncosa-Melvin, N., Boivin, G., *et al.* (2008). Functional tissue engineering for tendon repair: a multidisciplinary strategy using mesenchymal stem cells, bio-scaffolds and mechanical stimulation. *J Ortho Res.* (26), 1-9.
- [26] Butler, D.L., Goldstein, S.A., Guilak, F. (2000). Functional tissue engineering: the role of biomechanics. *J Biomech Eng* (122), 570-575.
- [27] Guilak, F., Butler, D.L., Goldstein, S.A., *et al.* (2014). Biomechanics and mechanobiology in functional tissue engineering. *J Biomech* (47), 1933-1940.
- [28] Balaban, N.Q., Schwarz, U.S., Riveline, D., Goichberg, P., Tzur, G., *et al.* (2001). Force and focal adhesion assembly: a close relationship studied using elastic micropatterned substrates. *Nat. Cell Biol.* (3), 466-472.
- [29] Yamamoto, K., Sokabe, T., Watabe, T., Miyazono, K., Yamashita, J.K., *et al.* (2005). Fluid shear stress induces differentiation of Flk-1-positive embryonic stem cells into vascular endothelial cells in vitro. *Am. J. Physiol. Heart Circ. Physiol.* (288), H1915-24.
- [30] Metallo, C.M., Vodyanik, M.A., de Pablo, J.J., Slukvin, I.I., Palecek, S.P. (2008). The response of human embryonic stem cell-derived endothelial cells to shear stress. *Biotechnol. Bioeng.* (100), 830-37.

- [31] Akbari, S. and Shea, H.R. (2012). Microfabrication and characterization of an array of dielectric elastomer actuators generating uniaxial strain to stretch individual cells. *J. Micromech. Microeng* (22), 045020 (12pp).
- [32] Wu, J. and Nyborg, W.L.M. (2006). *Emerging Therapeutic Ultrasound*. World Scientific, Hackensack, N.J.
- [33] Lenshof, A., *et al.* (2012). Acoustofluidics 8: applications of acoustophoresis in continuous flow microsystems. *Lab Chip* (12), 1210-1223.
- [34] Marino, A. *et al.* (2015). Piezoelectric Nanoparticle-Assisted Wireless Neuronal Stimulation. *ACS Nano* (9), 7678-7689.
- [35] Zimmermann, W. H. *et al.* (2002). Tissue engineering of a differentiated cardiac muscle construct. *Circ. Res.* (90), 223-230.
- [36] Hansen, A., Eder, A., Bonstrup, M., Flato, M., Mewe, M., Schaaf, S., Aksehirlioglu, B., Schworer, A., Uebeler, J., Eschenhagen, T. (2010). Development of a drug screening platform based on engineered heart tissue. *Circ Res* (107), 35-44.
- [37] Quinn, T.A., Kohl, P. (2013). Combining wet and dry research: experience with model development for cardiac mechano-electric structure-function studies. *Cardiovasc. Res.*, (97), 601-611.
- [38] Keplinger, C., *et al.* (2013). Stretchable, transparent, ionic conductors. *Science* (341), 984-987. (2013)
- [39] Lang, N., *et al.* (2014). A Blood-Resistant Surgical Glue for Minimally Invasive Repair of Vessels and Heart Defects. *Sci. Transl. Med.* (6), 218ra6.
- [40] Chung, H.J., *et al.* (2014). Stretchable, multiplexed pH sensors with demonstrations on rabbit and human hearts undergoing ischemia. *Adv. Healthc. Mater.* (3), 59-68.
- [41] Kim, D.H. *et al.* (2012). Electronic sensor and actuator webs for large-area complex geometry cardiac mapping and therapy. *Proc. Natl Acad. Sci. USA* (109), 19910-19915.
- [42] Radmacher, M., Tillamnn, R.W., Fritz, M., Gaub, H.E. (1992). From molecules to cells: imaging soft samples with the atomic force microscope. *Science* (257), 1900-5.
- [43] Galbraith, C.G., Sheetz, M.P. (1997). A micromachined device provides a new bend on fibroblast traction forces. *Proc. Natl. Acad. Sci. USA* (94), 9114-18.
- [44] Yang, S., Saif, T. (2005). Reversible and repeatable linear local cell force response under large stretches. *Exp. Cell Res.* (305), 42-50.
- [45] Sun, Y., Wan, K., Roberts, K., Bischof, J., Nelson, B. (2003). Mechanical property characterization of mouse zona pellucida. *IEEE Trans. Nanobiosci.* (2), 279-86.
- [46] Kim, K.Y., Cheng, J., Liu, Q., Wu, X.Y., Sun, Y. (2009). Investigation of mechanical properties of soft hydrogel microcapsules in relation to protein delivery using a MEMS force sensor. *J. Biomed. Mater. Res. A* (92), 103-113.

- [47] Kim, K.Y., Liu, X.Y., Zhang, Y., Cheng, J., Wu, X.Y., Sun, Y. (2009). Elastic and viscoelastic characterization of microcapsules for drug delivery using a force-feedback MEMS microgripper. *Biomed. Microdev.* (11), 421-27.
- [48] Park, J., Kim, J., Roh, D., Park, S., Kim, B., Chun, K. (2006). Fabrication of complex 3D polymer structures for cell-polymer hybrid systems. *J. Micromech. Microeng.* (16), 1614-19.
- [49] Park, J., Ryu, J., Choi, S.K., Seo, E., Cha, J.M., *et al.* (2005). Real-time measurement of the contractile forces of self-organized cardiomyocytes on hybrid biopolymer microcantilevers. *Anal. Chem.* (77), 6571-80.
- [50] Park, K., Jang, J., Irimia, D., Sturgis, J., Lee, J., *et al.* (2008). 'Living cantilever array' for characterization of mass of single live cells in fluids. *Lab Chip* (8), 1034-41.
- [51] Ossola, D. *et al.* (2015). Force-controlled patch clamp of beating cardiac cells. *Nano Lett* (15), 1743-1750.
- [52] Liu, Y. *et al.* (2012). In situ mechanical analysis of cardiomyocytes at nano scales. *Nanoscale* (4), 99-102.
- [53] Pesl, M. *et al.* (2016). Atomic force microscopy combined with human pluripotent stem cell derived cardiomyocytes for biomechanical sensing. *Biosensors and Bioelectronics* (85), 751-757.
- [54] Cogollo, J.F.S. *et al.* (2011). A new integrated system combining atomic force microscopy and micro- electrode array for measuring the mechanical properties of living cardiac myocytes. *Biomed. Microdev.* (13), 613-621.
- [55] Caluori, G. *et al.* (2019). Non-invasive electromechanical cell-based biosensors for improved investigation of 3D cardiac models. *Biosensors and Bioelectronics* (124,125), 129-135.
- [56] Tian, J. *et al.* (2017). Study of the union method of microelectrode array and AFM for the recording of electromechanical activities in living cardiomyocytes, *Eur Biophys J.* (46), 495-507.
- [57] Brown, E.N., Kass, R.E. & Mitra, P.P. (2004). Multiple neural spike train data analysis: state-of-the-art and future challenges. *Nat. Neurosci.* (7), 456-61.
- [58] Blau, A. (2013). Cell adhesion promotion strategies for signal transduction enhancement in microelectrode array in vitro electrophysiology: An introductory overview and critical discussion. *Curr. Opin. Colloid Interface Sci.* (18), 481-492.
- [59] Spira, M.E., Hai, A. (2013). Multi-electrode array technologies for neuroscience and cardiology. *Nat. Nanotechnol.* (8), 83-94.
- [60] Johnstone, A.F.M. *et al.* (2010). Microelectrode arrays: A physiologically based neurotoxicity testing platform for the 21st century. *Neurotoxicology* (31), 331-350.
- [61] Fejtl M., Stett A., Nisch W., Boven KH., Möller A. (2006) *On Micro-Electrode Array Revival: Its Development, Sophistication of Recording, and Stimulation*. In: Taketani M., Baudry M. (eds) *Advances in Network Electrophysiology*. Springer, Boston, MA.
- [62] Microelectrode Array (MEA) Manual. (2018). Multi Channel Systems, MCS GmbH, Reutlingen, Germany (www.multichannelsystems.com).

- [63] Kandere-Grzybowska, K., Campbell, C., Komarova, Y., Grzybowski, B.A., Borisy, G.G. (2005). Molecular dynamics imaging in micropatterned living cells. *Nat. Methods* (2), 739-41.
- [64] Chen, C.S., Mrksich, M., Huang, S., Whitesides, G.M., Ingber, D.E. (1997). Geometric control of cell life and death. *Science* (276), 1425-28.
- [65] Xia, N., Thodeti, C.K., Hunt, T.P., Xu, Q., Ho, M., *et al.* (2008). Directional control of cell motility through focal adhesion positioning and spatial control of Rac activation. *FASEB J.* (22), 1649-59.
- [66] Karp, J.M. (2006). A photolithographic method to create cellular micropatterns. *Biomaterials* (27), 4755-4764.
- [67] Yoonkey Nam *et al.* (2004). Gold-Coated Microelectrode Array With Thiol Linked Self-Assembled Monolayers for Engineering Neuronal Cultures, *IEEE TRANSACTIONS ON BIOMEDICAL ENGINEERING*, Vol. 51, No. 1.
- [68] Kim, D.H., Levchenko, A., Suh, K.Y. (2008). *Engineered surface nanotopography for controlling cell-substrate interactions. In Micro- and Nanoengineering of the Cell Microenvironment: Technologies and Applications*, ed. A Khademhosseini, J Borenstein, S Takayama, M Toner, 185-208. Boston: Artech House.
- [69] Szentivanyi, A., Chakradeo, T., Zernetsch, H. and Glasmacher, B. (2011). Electrospun cellular microenvironments: Understanding controlled release and scaffold structure. *Adv. Drug Delivery Rev.* (63), 209-220.
- [70] Chua, K.N., Chai, C., Lee, P.C., Tang, Y.N., Ramakrishna, S., Leong, K.W., and Mao, H.Q. (2007). Functional nanofiber scaffolds with different spacers modulate adhesion and expansion of cryopreserved umbilical cord blood hematopoietic stem/progenitor cells. *Exp. Hematol.* (35), 771-781.
- [71] Ding, Y., *et al.* (2015). Cooperative control of blood compatibility and re-endothelialization by immobilized heparin and substrate topography. *Acta Biomaterialia* (15), 150-163.
- [72] Moreno-Flores, S. and Toca-Herrera, J.L. (2013). *HYBRIDIZING SURFACE PROBE MICROSCOPIES, Toward a Full Description of the Meso- and Nanoworlds*. Taylor & Francis Group, NW.
- [73] Binnig, G., Rohrer, H., Gerber, C., Weibel, E. (1982). Surface Studies by Scanning Tunneling Microscopy. *Phys. Rev. Lett.* (49), 57-61.
- [74] Binnig, G., Quate, C., Gerber, C. (1986). Atomic Force Microscope. *Phys. Rev. Lett.* (56), 930-933.
- [75] Meyer, G., Amer, N. M. (1988). Novel Optical Approach to Atomic Force Microscopy. *Appl. Phys. Lett.* (53), 1045.
- [76] Butt, H.-J., Cappella, B., Kappl, M. (2005). Force Measurements with the Atomic Force Microscope: Technique, Interpretation and Applications. *Surf. Sci. Rep.* (59), 1-152.
- [77] Owen, R. JPK Instrument Application Report: A Practical Guide to AFM Force Spectroscopy and Data Analysis. 1-8.

- [78] Roduit C. "AFM figures", www.freesbi.ch. Creative Commons Attribution. 2010.
- [79] Hutter, J. L., Bechhoefer, J. (1993). Calibration of Atomic-Force Microscope Tips. *Rev. Sci. Instrum.* (64), 1868-1873.
- [80] 60HighDensityMEA, 60StandardMEA Manuals. (2018). Multi Channel Systems, MCS GmbH, Reutlingen, Germany (www.multichannelsystems.com)
- [81] Bologna, L.L., *et al.* (2010). Investigating neuronal activity by SPYCODE multi-channel data analyzer. *Neural Networks* (23), 685-697.
- [82] Marconi, E., *et al.* (2012). Emergent Functional Properties of Neuronal Networks with Controlled Topology. *Plos One* (7), e34648.
- [83] Pharr, G., Oliver, W. and Brotzen, F. (1992). On the generality of the relationship among contact stiffness, contact area, and elastic modulus during indentation. *Journal of materials research* (7), 613-617.
- [84] Haase, K. and Pelling, A.E. (2015). Investigating cell mechanics with atomic force microscopy. *J. R. Soc. Interface* (12), 20140970.
- [85] Engler, A. *et al.* (2004). Substrate compliance versus ligand density in cell on gel responses. *Biophysical journal* (86), 617-628.
- [86] Samani, A., Zubovits, J. & Plewes, D. (2007). Elastic moduli of normal and pathological human breast tissues: an inversion-technique-based investigation of 169 samples. *Physics in medicine and biology* (52), 1565.
- [87] Mi, K. *et al.* (2009). Influence of a self-assembling peptide, RADA16, compared with collagen I and matrigel on the malignant phenotype of human breast-cancer cells in 3D cultures and in vivo. *Macromolecular bioscience* (9), 437-443.
- [88] Radisky, D., Muschler, J. & Bissell, M. J. (2002). Order and disorder: the role of extracellular matrix in epithelial cancer. *Cancer investigation* (20), 139-153.
- [89] Weidner, N., *et al.* (1991). Tumor Angiogenesis and Metastasis - Correlation in Invasive Breast Carcinoma. *N. Engl. J. Med.* (324), 1-8.
- [90] Rothenberg, K.E., *et al.* (2018). Vinculin Force-Sensitive Dynamics at Focal Adhesions Enable Effective Directed Cell Migration. *Biophys. J.* (114), 1680-1694.
- [91] Ridley, A.J., *et al.* (2003). Cell migration: integrating signals from front to back. *Science* (302), 1704-1709.
- [92] Azios, N.G. and Dharmawardhane, S.F. (2005). Resveratrol and Estradiol Exert Disparate Effects on Cell Migration, Cell Surface Actin Structures, and Focal Adhesion Assembly in MDA-MB-231 Human Breast Cancer Cells. *Neoplasia* (7), 128-140.
- [93] Zouani, O.F., *et al.* (2013). Effect of BMP-2 from matrices of different stiffnesses for the modulation of stem cell fate. *Biomaterials* (34), 2157-2166.
- [94] Marrella, A., *et al.* (2017). Engineering vascularized and innervated bone biomaterials for improved skeletal tissue regeneration. *Materials Today* (21), 362-376.

- [95] Lovett, D.B., *et al.* (2013). Modulation of nuclear shape by substrate rigidity. *Cellular and molecular bioengineering* (6), 230-238.
- [96] Wei, G, and Ma, P.X. (2008). Nanostructured biomaterials for regeneration. *Advanced functional materials* (18), 3568-3582.
- [97] Murugan, R. and Ramakrishna, S. (2006). Nano-featured scaffolds for tissue engineering: a review of spinning methodologies. *Tissue Eng.* (12), 435-447.
- [98] Ramião, N.G., *et al.* (2016). Biomechanical properties of breast tissue, a state-of-the-art review. *Biomechanics and modeling in mechanobiology* (15), 1307-1323.
- [99] Liu, J., *et al.* (2018). Graphene-based nanomaterials and their potentials in advanced drug delivery and cancer therapy. *Control. Release*, (286), 64-73.

Appendix A

Mechanical Stimulation Protocols for hPSC-CMs

P R O T O C O L 1	HD MEA, tipless cantilever with spring constant=7.27N/m
	1. Baseline, 5 min, setpoint=10;
	2. Static force, 10-70nN, step 10nN every 60sec
	3. Impulsive force, 1Hz, 100-200nN, step 50nN every 60 sec
	4. Impulsive force, 2 Hz, 100-500nN, step 50nN every 60 sec
	5. Impulsive force, 5 Hz, 100-500nN, step 50nN every 60 sec
	6. Baseline, 5 min, setpoint 10
	HD MEA, tipless cantilever with spring constant=8N/m
	1. Baseline, 5 min, setpoint=20;
	2. Impulsive force, 1Hz, 100-500nN, step 50nN every 60 sec
	3. Impulsive force, 2 Hz, 100-500nN, step 50nN every 60 sec (6 μ m indentation)
P R O T O C O L 2	HD MEA, tipless cantilever with spring constant=23N/m
	1. Baseline, 5 min, setpoint=20;
	2. Static force, 100-500nN, step 100nN every 60sec
	3. Impulsive force, 1Hz, 200-600nN, step 200nN every 60 sec
	4. Impulsive force, 2 Hz, 200-1000nN, step 200nN every 60 sec
	5. Impulsive force, 4 Hz, 200-1000nN, step 200nN every 60 sec
	6. Baseline, 5 min, setpoint 200
	7. Baseline, 5min, no contact
P R O T O C O L 3	HD MEA, tipless cantilever with spring constant=7.13N/m
	1. Baseline, 5 min, setpoint=20;
	2. Constant height, 200nN
	3. Post-stim, 5 min, setpoint 20
	4. Constant height, 100nN
	5. Post-stim, 5 min, setpoint 20
	6. Transient overload, 50nN, 2Hz, 12mm/sec, z lenght 2mm
	7. Post-stim, 5 min
	8. Transient overload, 100nN, 2Hz, 14mm/sec, z lenght 2mm
	9. Post-stim, 5 min
	10. Impulsive force, 10 Hz, 150nN
	11. Baseline, 5min